INAUGURAL - DISSERTATION

submitted to the
Joint Faculties for Natural Sciences and Mathematics
of the Ruperto Carola University of
Heidelberg, Germany,
for the degree of
Doctor of Natural Sciences

Put forward by
M.Sc. Lars Müller
born in Friedrichshafen

Oral examination: June 28th, 2017

Improved Estimation of Microscopic Tissue Parameters by Double Diffusion Encoding and Flow-Compensated Single Diffusion Encoding Magnetic Resonance Imaging

Referees: Prof. Dr. Peter Bachert
Prof. Dr. Joao Seco

Verbesserung der Bestimmung von mikroskopischen Gewebseigenschaften mittels doppelt diffusionsgewichteter und flusskompensierter einzeln diffusionsgewichteter Magnetresonanztomographie

Die diffusionsgewichtete Magnetresonanztomographie (MRT) erlaubt es Rückschlüsse auf die Mikrostruktur des untersuchten Gewebes zu ziehen, welche mit der begrenzten Auflösung des MRT-Bildes nicht dargestellt werden. Für Diffusionsmessungen ist die Schaltung starker Gradientenpulse nötig, die zu Artefakten aufgrund von Wirbelströmen und Maxwell-Feldern (*concomitant fields*) führen kann. Eine weitere Quelle von Artefakten ist die gerichtete Bewegung, wie zum Beispiel Pulsation oder Blutfluss. Für die genauere Bestimmung der mikroskopischen fraktionellen Anisotropie (μFA) wurde eine doppelt refokussierte Spinecho-Sequenz für die doppelt diffusionsgewichtete MRT angepasst. Durch diese Wirbelstromkompensation wurden die fälschlicherweise erhöhten μFA Werte in der grauen Substanz (im Mittel von 0.57 ± 0.19 auf 0.50 ± 0.19) und den Ventrikeln (im Mittel von 0.54 ± 0.19 auf 0.28 ± 0.27) von gesunden Probanden verringert.

Eine zweite Sequenz, mit einer Einzeldiffusionswichtung, wurde entwickelt um jegliche Kombination der drei Quellen von Artefakten (Fluss, Wirbelströme und Maxwell-Felder) kompensieren zu können. In vivo Messungen zeigten, dass für viele Messungen eine höhere Wiederholbarkeit der Aufnahmen erreicht wird, wenn Fluss und Maxwell-Felder kompensiert werden. Eine zusätzliche Wirbelstromkompensation führte, außer bei Kopf Messungen, zu keiner weiteren Verbesserung. Die zweite Sequenz wurde verwendet um die Perfusion mittels *Intravoxel Incoherent Motion* (inkohärente Bewegung innerhalb eines Voxels) Modells zu bestimmen. Diese Messungen wurden im Abdomen und in der Prostata von gesunden Probanden durchgeführt, wobei ein Unterschied zwischen flusskompensierten und nicht flusskompensierten Messungen festgestellt wurde. Dies war jedoch nicht der Fall bei Patienten mit Prostatakarzinom.

Improved Estimation of Microscopic Tissue Parameters by Double Diffusion Encoding and Flow-Compensated Single Diffusion Encoding Magnetic Resonance Imaging

Diffusion weighted magnetic resonance imaging (MRI) can be used to gain information on the microstructure of the examined tissue on length scales below the actual image resolution. The large gradient amplitudes required for diffusion measurements can lead to artifacts due to eddy currents and concomitant fields. Another source of image artifacts, is the presence of directed motion such as blood flow or pulsation. In a first MRI sequence, a common approach for eddy current compensation, the twice-refocused spin echo was adjusted for a double diffusion encoding (DDE) sequence. In measurements of healthy volunteers, this approach reduced the falsely elevated microscopic fractional anisotropy (μFA) in the gray matter on average from 0.57 ± 0.19 to 0.50 ± 0.19 and in the ventricles on average from 0.54 ± 0.19 to 0.28 ± 0.27.

A second sequence, with a single diffusion encoding, was compensated for any combination of the three artifact sources flow, concomitant fields and eddy currents. For most in vivo measurements, it proved to be sufficient to compensate for flow and concomitant fields. An additional eddy current compensation led only in the brain measurements to a higher reproducibility. The developed sequence was also used to measure the incoherent intravoxel motion (IVIM) effect in the abdomen as well as the prostate of healthy volunteers, where a difference between flow-compensated and non-flow-compensated measurements was observed. This difference could not be seen in patients with prostate carcinoma.

Contents

List of Figures

List of Tables

List Of Abbreviations

ADC	apparent diffusion coefficient
BPH	benign prostatic hyperplasia
CV	coefficient of variation
DDE	double diffusion encoding
DTI	diffusion tensor imaging
DWI	diffusion weighted imaging
EPI	echo planar imaging
FA	fractional anisotropy
FEXI	filter exchange imaging
FOV	field of view
IVIM	intravoxel incoherent motion
MD	mean diffusivity
MR	magnetic resonance
MRI	magnetic resonance imaging
μFA	microscopic fractional anisotropy
NMR	nuclear magnetic resonance
qMAS	q-vector magic-angle spinning
RF	radio frequency
ROI	region of interest
SDE	single diffusion encoding
SNR	signal-to-noise ratio
TE	echo time
TR	repetition time
TRSE	twice-refocused spin echo

1 Introduction

In magnetic resonance imaging (MRI), tomographic images are acquired without the use of ionizing radiation, which is an advantage over computed tomography (CT) and position emission tomography (PET). MRI additionally offers a large variety of contrast mechanisms that allow not only anatomic imaging with a high soft tissue contrast, but also functional imaging. MRI has, for example, been used to assess tissue perfusion with contrast agent [SB13] or to examine chemical exchange with chemical exchange saturation transfer (CEST) [vZY11] as well as particle exchange over membranes [QBD+03]. The many different contrast mechanisms, the high soft tissue contrast and the absence of ionizing radiation have made MRI a wide spread tool in diagnostics and research, despite its mostly lower resolution than CT.

The self-diffusion of water is another parameter used in MRI. The influence of diffusion on the magnetic resonance signal has been described already in 1950 [Hah50]. Since then, it has been used to gain information about tissue structures smaller than the image resolution. This is possible because the diffusive motion during a typical MRI sequence is on the length scale of cell sizes. The measurements rely on the application of gradient pulses to make the signal sensitive to diffusive motion [ST65]. The main application of diffusion weighted imaging (DWI) is in the brain. It has, for example, been proven useful in detecting ischemic areas in strokes [MCM+90].

It was also shown that it is possible to assess the anisotropy of coherent white matter fibers [CBP90, MKAN91] by the use of the diffusion tensor [BML94a, BML94b]. This anisotropy is lost if the fibers inside a voxel are not coherently ordered, as, for example, is the case for fiber crossings, or if there is a loss of fibers. The reasons for a lower anisotropy cannot be distinguished with the diffusion tensor alone. In 1995, an approach to determine the anisotropy of the diffusion compartments directly was proposed [Mit95]. It was shown that the application of two individual diffusion encodings can overcome the need for a coherent ordering to determine the anisotropy of the actual diffusion compartments. The feasibility of this approach was demonstrated in humans [LF13]. As a measure of the compartment anisotropy, the microscopic fractional anisotropy μFA was proposed [JLSD13].

Besides the applications in the brain, diffusion measurements were also used in other body parts. The apparent diffusion coefficient (ADC) was shown to be a useful marker in the detection of prostate cancer and is included in guidelines for prostate imaging [WBC+16]. In 1986, LeBihan et al. proposed a model to determine the fraction of the signal that is attributed to the tissue perfusion [LBL+86, LBL+88]. This model is called intravoxel incoherent motion (IVIM) model and assumes that the blood flow in tissue can be modeled as a pseudo-diffusion for long diffusion encoding times owing to the random orientation of small blood vessels. The model parameters allow for a differentiation between normal and cirrhotic liver [LVC+08] and between pancreatitis and pancreatic carcinoma [KLG+11].

Despite these results, it was shown that the assumption of long diffusion encoding times is not met in many experiments [WSL15]. This was achieved by using a flow compensated diffusion encoding. If the long time limit would be valid, there should have been no difference between the flow-compensated and non-flow-compensated diffusion measurement.

All these diffusion measurements require the application of strong gradient pulses, which can lead to image artifacts. There are especially two kinds of artifacts that were considered in this work, eddy currents and concomitant fields. Eddy currents are caused by the switching of gradient amplitudes [VVB90, JWS90] and lead to image distortions. In the case of many diffusion encoding directions or strengths, the image distortions can lead to misregistrations and thus to false parameter estimations. Concomitant fields are caused by the fact that the Maxwell equations do not allow linear gradient fields in MRI. This leads to an additional spatially varying field, which can cause signal voids or wrong diffusion coefficients [MZFP08].

The aim of this work was to reduce these artifacts and thus allowing for a more accurate determination of microscopic tissue parameters. Therefore, two sequences were developed, an eddy-current-compensated double diffusion encoding (DDE) sequence for the determination of μFA and a single diffusion encoding (SDE) sequence with flow, concomitant field and eddy current compensation for the measurement of IVIM parameters. Both sequences were tested in phantom experiments as well as in vivo.

2 Basics: Principles of Nuclear Magnetic Resonance

In this chapter, a short introduction to nuclear magnetic resonance (NMR) is given and the basic principles needed for imaging are reviewed. For a more detailed look at these subjects, there are several books [Abr11, HBTV99, BKZ04] available. Here, the main focus is on the nuclei of hydrogen atoms, that is protons, as they were used for imaging. There are several other nuclei that can be used for magnetic resonance imaging (MRI), but they were not considered in this work.

2.1 Nuclear Spin and Magnetic Moment

The nucleus of a hydrogen atom consists in most cases of one proton, which in turn leads to a nuclear spin $\hat{\boldsymbol{I}} = (\hat{I}_x, \hat{I}_y, \hat{I}_z)$. In quantum mechanics, a spin is treated as an angular momentum with the known commutator relations:

$$[\hat{I}_i, \hat{I}_j] = i\hbar\epsilon_{ijk}\hat{I}_k \tag{2.1}$$

$$[\hat{\boldsymbol{I}}^2, \hat{I}_i] = 0 \tag{2.2}$$

and eigenvalue equations:

$$\hat{\boldsymbol{I}}^2|I, m\rangle = I(I+1)\hbar^2|I, m\rangle \tag{2.3}$$

$$\hat{I}_z|I, m\rangle = \hbar m|I, m\rangle, \tag{2.4}$$

where ϵ_{ijk} stands for the Levi-Civita symbol, i,j and k can be x, y or z, and the z-direction is chosen as the axis of quantization. The commutator relations show that there is a complete set of eigenfunctions of $\hat{\boldsymbol{I}}^2$ and $\hat{I}_z$. The corresponding eigenvalues are given by equations 2.3 and 2.4. In general, the value I can take positive integer or half-integer values. For a proton, it is $1/2$. The value m can take the values $-I$, $-I+1$, ... , I and therefore the possible values for m are $-1/2$ and $1/2$ for $I = 1/2$.

The spin is connected to a magnetic moment $\hat{\boldsymbol{\mu}}$ by the gyromagnetic ratio γ:

$$\hat{\boldsymbol{\mu}} = \gamma\hat{\boldsymbol{I}}. \tag{2.5}$$

The value of γ dependents on the nucleus. In MRI, often $\frac{\gamma}{2\pi}$ is used, which takes the value 42.576 MHz/T for protons.

2.2 Static External Magnetic Fields

The interaction of a spin with an external magnetic field is described by the Hamiltonian $\hat{H}$:

$$\hat{H} = -\hat{\boldsymbol{\mu}} \cdot \boldsymbol{B}. \tag{2.6}$$

For a static magnetic field B_0 in z-direction, the Hamiltonian is simplified to

$$\hat{H} = -\gamma B_0 \hat{I}_z. \tag{2.7}$$

The convention that the main magnetic field $\boldsymbol{B_0}$ is parallel to z-direction is used for the rest of this text. Equation 2.7 shows that eigenfunctions of $\hat{I}_z$ and $\hat{\boldsymbol{I}}^2$ are also eigenfunctions of $\hat{H}$ and thus

$$\hat{H}|I, m\rangle = E_m|I, m\rangle \tag{2.8}$$

can be used to determine the energy E_m of the eigenstates. By inserting equation 2.4 in equation 2.8, the energies can be calculated to $E_m = -\gamma\hbar m B_0$. The energy difference between neighboring states is thus

$$\Delta E = E_m - E_{m\pm1} = \gamma\hbar B_0. \tag{2.9}$$

This split in the formerly degenerate energy states is known as Zeeman effect. For the excitation of spins in this system, a photon with the energy $\hbar\omega_0$ is needed, with

$$\omega_0 = \gamma B_0, \tag{2.10}$$

which is known as the Larmor frequency. To induce transitions between the two states of a hydrogen nucleus in a magnetic field with $B_0 = 3\,\mathrm{T}$, electromagnetic waves with the frequency $\nu_0 = \frac{\omega_0}{2\pi} = 127.8\,\mathrm{MHz}$ are needed.

2.3 Macroscopic Magnetization

In MRI, the measurement involves a large spin ensemble so that the observed quantity is not the single spin but rather a magnetization. The magnitude of this magnetization is given by the difference in the population of the two energy states. The population probability p_m of the state with E_m in thermal equilibrium at absolute temperature T is described by the Boltzmann distribution:

$$p_m = \frac{\exp\left(-E_m/k_B T\right)}{\sum_{m=-I}^{I} \exp\left(-E_m/k_b T\right)} = \frac{\exp(\gamma\hbar m B_0/k_B T)}{\exp(-\gamma\hbar B_0/2k_B T) + \exp(\gamma\hbar B_0/2k_B T)}, \tag{2.11}$$

where k_B is the Boltzmann constant. For the last step, $I = 1/2$ was used explicitly. The population ratio of the two states is given by

$$\frac{p_{-1/2}}{p_{1/2}} = \frac{\exp(-\gamma\hbar B_0/2k_B T)}{\exp(\gamma\hbar B_0/2k_B T)} = \exp(-\gamma\hbar B_0/k_B T) \tag{2.12}$$

and the difference in occupation ΔN for a total of N particles by

$$\Delta N = N(p_{-1/2} - p_{+1/2}) = N \tanh\left(\frac{\gamma\hbar B_0}{2k_B T}\right). \tag{2.13}$$

For a body temperature of $T = 310\,\mathrm{K}$ and a magnetic field of $B_0 = 3\,\mathrm{T}$, the relative difference $\frac{\Delta N}{N}$ is $9.89 \cdot 10^{-6}$, which means there is only a very small excess of spins with $m = -1/2$. This ratio has to be compared to the number of particles in a typical imaging volume of a few mm^3, which is in the order of 10^{19} or higher, leading to a measurable signal.

The macroscopic magnetization $\boldsymbol{M}$ is given by the sum of the expected values of the magnetic moments:

$$\boldsymbol{M} = \frac{1}{V}\sum_i \langle \hat{\boldsymbol{\mu}}_{\boldsymbol{i}} \rangle = \frac{\gamma}{V}\sum_i \langle \hat{\boldsymbol{I}} \rangle. \tag{2.14}$$

The eigenstates for $\hat{I}_x$ and $\hat{I}_y$ are degenerate, meaning their expectation values vanish and thus leading to a magnetization parallel to the external magnetic field with a magnitude M_0:

$$M_0 = \frac{\gamma}{V}\sum_i \langle \hat{I}_z \rangle = \frac{N}{V}\gamma\hbar \sum_{m=-I}^{I} m p_m. \tag{2.15}$$

Because of the high temperature compared to the magnetic energy ($\gamma\hbar B_0 \ll k_B T$), the exponentials from equation 2.11 can be expanded in their Taylor series up to the first order $\exp(-\gamma\hbar B_0/2k_B T) \approx 1 - \gamma\hbar B_0/2k_B T$. With this approximation, M_0 is given by

$$M_0 \approx \frac{N}{V}\frac{\gamma^2\hbar^2 I(I+1)B_0}{3k_B T} = \frac{N}{V}\frac{\gamma^2\hbar^2 B_0}{4k_B T}, \tag{2.16}$$

which is known as Curie's law. The equal sign holds for $I = 1/2$. Equation 2.16 shows that the magnetization is proportional to the spin density $\frac{N}{V}$ and the magnetic field B_0, and inverse proportional to the temperature T.

2.4 Radio Frequency Pulses

To understand the effect of radio frequency (RF) pulses, first, the time evolution of $\boldsymbol{M}$ in a magnetic field is needed. It can be derived by applying the Ehrenfest theorem to the magnetic moments:

$$\frac{\mathrm{d}\langle \hat{\boldsymbol{\mu}} \rangle}{\mathrm{d}t} = \frac{i}{\hbar}\langle [\hat{\boldsymbol{H}}, \hat{\boldsymbol{\mu}}] \rangle = \langle \hat{\boldsymbol{\mu}} \rangle \times \gamma \boldsymbol{B}(t). \tag{2.17}$$

To get the equation for the magnetization, this has to be summed over all magnetic moments, which results in:

$$\frac{\mathrm{d}\boldsymbol{M}(t)}{\mathrm{d}t} = \boldsymbol{M}(t) \times \gamma \boldsymbol{B}(t). \tag{2.18}$$

Equation 2.18 describes a circular motion of $\boldsymbol{M}(t)$ about $\boldsymbol{B}(t)$ if $\boldsymbol{M}(t)$ and $\boldsymbol{B}(t)$ are not parallel. This kind of motion is known as precession. The angular frequency is given by γB which for a constant field with B_0 results in the Larmor frequency ω_0.

If additionally to the static field $\boldsymbol{B_0}$, a time dependent field $\boldsymbol{B_1}(t)$ of the form

$$\boldsymbol{B_1}(t) = B_1 \left(\cos(\omega_1 t), -\sin(\omega_1 t), 0\right) \tag{2.19}$$

is applied, the magnetization precesses around the effective field $\boldsymbol{B_0} + \boldsymbol{B_1}(t)$. This time evolution can be described more easily in a reference frame that is rotating with $\boldsymbol{B_1}(t)$. In the rotating frame of reference, the equation of motion for the magnetization $\boldsymbol{M'}(t)$ is given by

$$\frac{\mathrm{d}\boldsymbol{M'}(t)}{\mathrm{d}t} = \boldsymbol{M'}(t) \times \gamma \boldsymbol{B'_{\text{eff}}} = \boldsymbol{M'}(t) \times \gamma \left(B_1, 0, B_0 - \frac{\omega_1}{\gamma}\right) \tag{2.20}$$

and describes a precession about $\boldsymbol{B'_{\text{eff}}}$ with the angular frequency $\omega'_{\text{eff}} = \gamma ||\boldsymbol{B'_{\text{eff}}}||$. In the case of $\omega_1 = \omega_0$, the z'-term vanishes and the magnetization precesses about the x'-direction. Usually, such an on-resonant field is applied for a time t_p, leading to an angle α between the initial and final direction of the magnetization:

$$\alpha = \int_0^{t_p} \omega_{\text{eff}} \, \mathrm{d}t = \gamma B_1 t_p. \tag{2.21}$$

The flip angle α can, according to equation 2.21, be changed by the amplitude of the pulse B_1 and its duration t_p. In this work, two flip angles were used, one with $\alpha = 90°$ for excitation and one with $\alpha = 180°$ for refocusing. A magnetization that is initially parallel to the z-direction precesses after a $90°$ pulse in the xy-plane. The idea behind a refocusing pulse is explained in section 2.6.

2.5 Relaxation and Bloch Equations

The lowest energy is achieved for a magnetization $\boldsymbol{M}$ that is parallel to the magnetic field $\boldsymbol{B_0}$. If the system is disturbed, for example, by a RF pulse, it relaxes back in the ground state. This relaxation can be described by two separate parts that are associated with the different components of the magnetization. $\boldsymbol{M}$ can be separated in a component parallel to the magnetic field, called longitudinal magnetization $\boldsymbol{M}_{\parallel}$, and a component perpendicular to the magnetic field, called transversal magnetization $\boldsymbol{M}_{\perp}$:

$$\boldsymbol{M} = \boldsymbol{M}_{\parallel} + \boldsymbol{M}_{\perp}. \tag{2.22}$$

The transversal magnetization is the source of the MRI signal. It precesses about the main magnetic field and induces a current in the receive coils. For the description of the signal, it is helpful to write the transversal magnetization as a complex number $M_{xy} = M_x + iM_y = M_{\perp} \mathrm{e}^{i\Phi}$. The longitudinal magnetization is denoted as M_z.

2.5.1 Longitudinal Relaxation

For M_z to return to its equilibrium state M_0, an energy exchange is needed. This is achieved by the thermal coupling to the surrounding material. The time constant of this process is called T_1 and the process itself is called T_1- or longitudinal relaxation. In a quantum mechanical picture, the longitudinal relaxation rate $R_1 = 1/T_1$ can be understood as a measure of the transition probability between the two Zeeman states. These are induced by the fluctuating magnetic field caused by the thermal motion of the particles.

2.5.2 Transversal Relaxation

After an excitation pulse, the transversal magnetization is formed by a coherent superposition of the spin states. This coherence is lost over time, due to dipole-dipole interactions which lead to fluctuations in the local magnetic field and therefore in the local Larmor frequency. In many cases, this can be described reasonably well with a single time constant T_2. The dipole-dipole interactions lead to an irreversible coherence loss.

Additionally, there exists a reversible relaxation. This is caused by inhomogeneities in the magnetic field, for example, due to technical limitations or local susceptibility differences. These effects are described by a time constant T_2'. The total dephasing is determined by $T_2^\star$:

$$\frac{1}{T_2^\star} = \frac{1}{T_2} + \frac{1}{T_2'}. \tag{2.23}$$

The coherence loss because of magnetic field inhomogeneities is reversible by the spin echo technique (section 2.6).

2.5.3 Bloch Equations

In equation 2.18, the relaxation processes are not included. This was done phenomenologically by Bloch [Blo46]:

$$\frac{\mathrm{d}M_x}{\mathrm{d}t} = (\gamma \boldsymbol{M} \times \boldsymbol{B})_x - \frac{M_x}{T_2^\star} \tag{2.24a}$$

$$\frac{\mathrm{d}M_y}{\mathrm{d}t} = (\gamma \boldsymbol{M} \times \boldsymbol{B})_y - \frac{M_y}{T_2^\star} \tag{2.24b}$$

$$\frac{\mathrm{d}M_z}{\mathrm{d}t} = (\gamma \boldsymbol{M} \times \boldsymbol{B})_z - \frac{M_z - M_0}{T_1} \tag{2.24c}$$

For a constant magnetic field in z-direction, these equations can be solved. The results for the perpendicular field component M_{xy} and for the longitudinal one M_z are

$$M_{xy}(t) = M_{xy}(0)\mathrm{e}^{-i\omega_0 t}\mathrm{e}^{-\frac{t}{T_2^\star}} \tag{2.25}$$

$$M_z(t) = M_0 - (M_0 - M_z(0))\mathrm{e}^{-\frac{t}{T_1}}. \tag{2.26}$$

This solution describes the so-called free induction decay (FID), which, for example, appears after a 90°-pulse. As mentioned above, the measured signal is determined by M_{xy}, which precesses around the z-axis while its magnitude undergoes an exponential decay.

2.6 Echo Formation

In equations 2.24a and 2.24b, the time constant is $T_2^\star$, which includes reversible and irreversible effects. One way to reverse the dephasing induced by local magnetic field inhomogeneities $\Delta B_{loc}(\boldsymbol{r})$ is the spin echo. For this method, a 180° pulse, the so called refocusing pulse, is applied at $t = \tau$ after the 90° pulse. This leads to an echo formation at the echo time (TE) TE $= 2\tau$. For the explanation, the RF pulses are assumed to be applied instantaneously.

The magnetization is flipped in the transversal plane by the excitation pulse. Due to $\Delta B_{loc}(\boldsymbol{r})$, the magnetization gathers a spatially dependent relative phase $\Delta\Phi(\boldsymbol{r}, t) = \gamma \Delta B_{loc}(\boldsymbol{r}, t)$, which leads to a signal decay. The phase is inverted by the 180° pulse $\Delta\Phi(\boldsymbol{r}, \tau) = -\gamma \Delta B_{loc}\tau$, while for stationary particles the precession frequency stays constant leading to a relative phase after the 180° pulse of $\Delta\Phi(\boldsymbol{r}, \tau + t) = \gamma \Delta B_{loc}(t - \tau)$. The relative phase becomes zero at $t + \tau = 2\tau$ and gives rise to a signal reformation, the so-called spin echo. A representation of this process is shown in figure 2.1. The amplitude of the echo is determined by T_2.

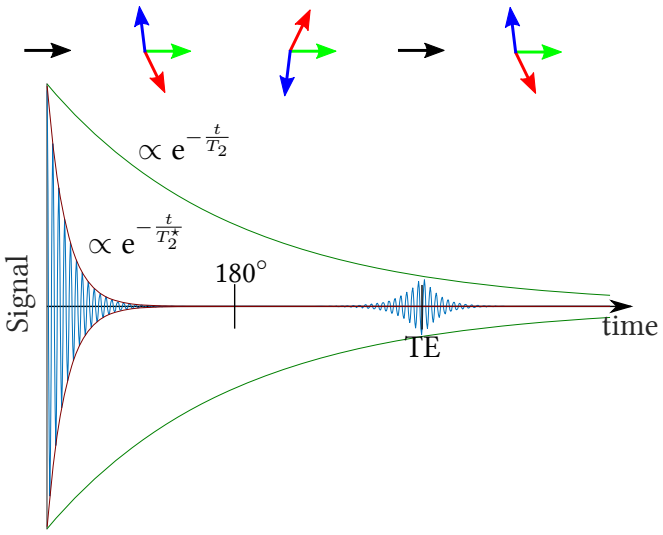

Figure 2.1: Signal evolution for a spin echo sequence. The signal decays initially with the time constant $T_2^\star$ (red lines). After the time TE/2, a refocusing pulse is applied (vertical line), which leads to a spin echo at TE, whose amplitude is determined by T_2 (green lines). Above the signal evolution, a pictorial explanation of the spin echo formation is shown (without T_2-relaxation). The three magnetization vectors dephase due to magnetic field inhomogeneities. The phase is inverted by the 180° pulse, which leads to a rephasing at $t =$ TE.

Another way an echo can be created is to use spatially dependent magnetic fields, called magnetic field gradients (section 3.1) that are applied deliberately. First, a gradient is used to induce a dephasing, which is rephased by the application of an opposite gradient. This is called a gradient echo.

3 Basics: Principles of NMR Imaging

Thus far, the processes in NMR have been described without considering how to obtain spatial information. For acquiring an image, a spatial dependence is created by the application of magnetic field gradients. The techniques used for image encoding are outlined in this chapters. The relaxation processes are not considered explicitly.

3.1 Magnetic Field Gradients

Normally, a MRI machine has three sets of gradient coils to create three orthogonal, mostly linear gradient fields (G_x, G_y and G_z). They slightly change the B_0 field, leading to different Larmor frequency. The gradient $\boldsymbol{G}$ can be written as

$$\boldsymbol{G} = (G_x, G_y, G_z) = \left(\frac{\partial B_z}{\partial x}, \frac{\partial B_z}{\partial y}, \frac{\partial B_z}{\partial z} \right). \tag{3.1}$$

If such a gradient is applied, the Larmor frequency becomes

$$\omega(\boldsymbol{r}, t) = \gamma(\boldsymbol{B_0} + \boldsymbol{r} \cdot \boldsymbol{G}(t)) = \omega_0 + \omega_G(\boldsymbol{r}, t), \tag{3.2}$$

with $\omega_G(\boldsymbol{r}, t) = \gamma \boldsymbol{r} \cdot \boldsymbol{G}(t)$ as the frequency change due to the gradient. In clinical MRI machines, the typical maximal gradient amplitude lies between 40 mT/m and 80 mT/m. A gradient can be switched to the maximal amplitude in under 1 ms. The switching of the gradient amplitude is called ramp and the minimal ramp time is determined by the slew rate, which is in clinical MRI around 100-200 T/m/s.

Gradient pulses are often described by their temporal profile. A common profile used is the trapezoidal gradient pulse, with a maximal amplitude g, total duration T_G and a starting time t_0 (see figure 3.1):

$$G(t) = \begin{cases} \frac{g}{p}(t - t_0) & \text{if } t_0 < t \leq t_0 + p \\ g & \text{if } t_0 + p < t \leq t_0 + \delta \\ g(1 - \frac{1}{p}(t - t_0 - \delta)) & \text{if } t_0 + \delta < t \leq t_0 + T_G \end{cases} \tag{3.3}$$

The definition of the timing parameters is shown in figure 3.1.

3.2 Slice Selection

One way to gain spatial information is to excite only a slice of a thickness Δz. Here, the convention of z as slice direction is used without loss of generality. A slice selective

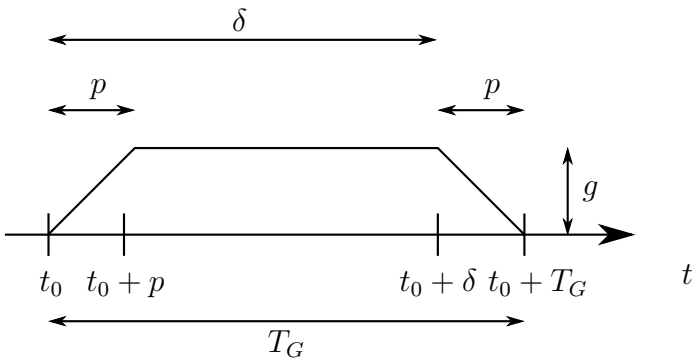

Figure 3.1: Temporal profile of a trapezoidal gradient pulse with definition of timing parameters.

excitation is achieved by applying a RF pulse at the same time as a gradient $\boldsymbol{G} = (0, 0, G_z)$ is applied. If a RF pulse is applied with the central frequency ω_c and a bandwidth $\Delta\omega$, only the range Δz is excited. To determine Δz, the Bloch equations need to be considered for fo this case. The Bloch equations can be solved in the small flip angle approximation, which assumes $M_z(t) \approx M_0$. The result for the transversal magnetization is given by [BKZ04]:

$$M_{xy}(t_p, z) \approx i\gamma M_0 \mathrm{e}^{-i\gamma z G_z t_p} \int_0^{t_p} B_1(t) \mathrm{e}^{i\gamma z G_z t} \, \mathrm{d}t, \tag{3.4}$$

with a pulse duration t_p. This solution shows that the slice profile is given by the Fourier transform of the envelope of the B_1 field.

In most applications, the goal is to excite a homogeneous slice, which is described by a box function. That means the excitation pulse would ideally be an infinitely long sinc pulse $B_1(t) = \frac{\sin \Delta\omega t}{\Delta\omega t}$. With such a pulse, the slice thickness is given by

$$\Delta z = \frac{\Delta\omega}{\gamma G z}. \tag{3.5}$$

Equation 3.5 presents two ways to adjust the slice thickness, the bandwidth of the envelope of $B_1(t)$ and the gradient amplitude G_z (illustrated in figure 3.2). In reality, the pulse duration is limited, which leads to a different slice profile. These deviations can be compensated in part by changing the pulse profile.

Another result from equation 3.4 is that the magnetization is acquiring a z-dependent phase due to the gradient. This phase is determined by the isodelay point, the time point after which the gradient effectively dephases the magnetization. For the pulses and slice selection gradients used here, the isodelay point lies in the middle of the gradient. To rephase the magnetization, a second gradient pulse is applied in the opposite direction.

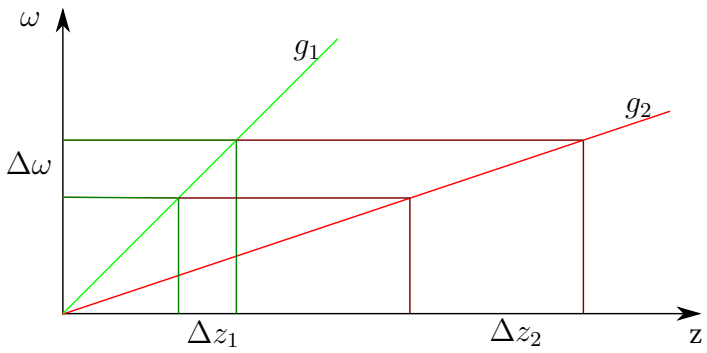

Figure 3.2: Connection of bandwidth and slice thickness. The z-dependent Larmor frequency is shown for two gradient amplitudes (g_1 and g_2). The RF pulse bandwidth ($\Delta\omega$) together with the gradient amplitude define the slice thickness Δz. The slice thickness is larger for a lower gradient amplitude.

3.3 Spatial Encoding and k-Space

3.3.1 Basic Principle of Spatial Encoding

For the generation of an image, additional gradients are used for spatial encoding. These gradients lead to a relative phase $\Phi_G(\boldsymbol{r}, t)$:

$$\Phi_G(\boldsymbol{r}, t) = \gamma \int_0^t \omega_G(\boldsymbol{r}, t')\,\mathrm{d}t' = \gamma \int_0^t \boldsymbol{r} \cdot \boldsymbol{G}(t')\,\mathrm{d}t' = \boldsymbol{r} \cdot \boldsymbol{k}(t), \tag{3.6}$$

where the wave vector $\boldsymbol{k}(t)$ was defined as

$$\boldsymbol{k}(t) = \gamma \int_0^t \boldsymbol{G}(t')\mathrm{d}t'. \tag{3.7}$$

Thus, neglecting relaxation, the time and spatially dependent transversal magnetization $M_{xy}(\boldsymbol{r}, t)$ can be written in the rotating coordinate system as

$$M_{xy}(\boldsymbol{r}, t) = M_{xy}(\boldsymbol{r}, 0)\mathrm{e}^{-i\boldsymbol{k}(t)\cdot\boldsymbol{r}}. \tag{3.8}$$

The signal S, which is measured in MRI, is proportional to the integral over the whole volume and thus

$$S(\boldsymbol{k}(t)) \propto \int_V M_{xy}(\boldsymbol{r}, t)\mathrm{d}\boldsymbol{r} = \int_V M_{xy}(\boldsymbol{r}, 0)\mathrm{e}^{-i\boldsymbol{k}(t)\cdot\boldsymbol{r}}\mathrm{d}\boldsymbol{r}. \tag{3.9}$$

This equation describes formally a Fourier transform. Thus, the distribution of the magnetization can be calculated by applying the inverse Fourier transform to the signal measured in k-space:

$$M_{xy}(\boldsymbol{r}, 0) \propto \int S(\boldsymbol{k}(t))\mathrm{e}^{i\boldsymbol{k}(t)\cdot\boldsymbol{r}}. \tag{3.10}$$

The wave vector can be manipulated freely by the gradients so that the whole k-space can, theoretically, be acquired . Two common ways for the manipulation of $\boldsymbol{k}$ are described shortly in the following sections.

3.3.2 Frequency Encoding

For frequency encoding, a gradient pulse is applied during the signal acquisition, the so-called readout. This leads to $\boldsymbol{k}$ changing along a line and therefore this k-space line is acquired. Although, it is possible to start the readout in the k-space center without any preceding gradients, a more common approach is to apply a readout dephaser gradient before the readout. In this case, the k-space line is acquired from one edge to the other. For of a spin echo sequence, the gradient pulses are adjusted in such a way that the k-space center is acquired exactly at the time of the spin echo.

3.3.3 Phase Encoding

Phase encoding is achieved by applying a gradient before the actual readout. This leads to a phase dispersion that is conserved during readout. With this technique, single points in k-space can be acquired. In many applications, phase and frequency encoding are combined for encoding in perpendicular directions.

3.3.4 Discrete k-Space

In reality, the k-space can only be acquired at a discrete number of points, which leads to a few limitations. The sampling of the signal at distinct points, with a distance of Δk, can be described by multiplying the continuous signal with a sampling function, given by a sum of delta functions. The continuous magnetization is given by the Fourier transform of the continuous signal (equation 3.10). In this case, the convolution theorem states that the measured magnetization is given by the convolution of the continuous signal with the sampling function. The convolution leads to periodical repetition of the magnetization distribution. In one dimension, these are centered around $x_j = \frac{2\pi j}{\Delta k}$, with $j \in \mathbb{Z}$, and define the field of view (FOV):

$$\mathrm{FOV}_x = \frac{2\pi}{\Delta k_x} \tag{3.11}$$

The limited FOV can lead to an image overlap if parts of the measurement object are outside of the FOV. This kind of artifact is called aliasing. To avoid image overlap, the Nyquist theorem needs to be fulfilled:

$$x_{\min} = -\frac{\pi}{\Delta k} \leq x \leq \frac{\pi}{\Delta k} = x_{\min}. \tag{3.12}$$

The finite sampling width of the k-space with N points results in a maximal k-value $k_{\max} = \frac{N\Delta k}{2}$. This value determines the resolution in the image space:

$$\Delta x = \frac{\mathrm{FOV}}{N} = \frac{\pi}{k_{\max}}. \tag{3.13}$$

Thus, to resolve small objects, the k-space needs to be sampled far away from the center, while the main contribution to the image contrast stems from there.

3.3.5 Echo Planar Readout

A special method to read out the k-space is the echo planar imaging (EPI) technique, which was proposed already in 1977 [Man77]. It could only be realized over a decade later, once the gradient systems were able to handle the high demands. The idea is to acquire the whole k-space after a single excitation. The readout scheme with a spin echo preparation and corresponding k-space trajectory is shown in figure 3.3.

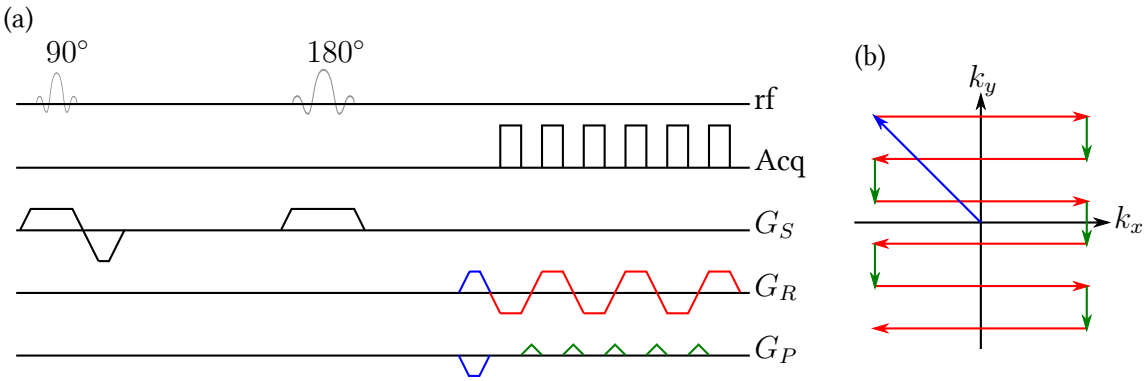

Figure 3.3: Spin echo with EPI readout and k-space trajectory. The dephaser gradients (blue) in the sequence scheme (a) move the acquisition (Acq) to a corner of the k-space (b). The effects of the individual readout (frequency encoding) gradients (red) and the phase blips (green) are shown as arrows in the k-space diagram.

To achieve k-space acquisition with a single excitation, at first, a phase encoding and a readout dephase gradient pulse are applied to reach one corner of the k-space. Afterwards, a k-space line is acquired by the use of frequency encoding. Once this is finished, a short gradient in phase direction, called blip, is applied to move to the next k-space line, which is acquired with another frequency encoding in the opposite direction. After this is completed, another phase blip is used, followed by a frequency encoding and so on until the whole k-space is acquired. If an EPI acquisition is used with a spin echo, the timing is adjusted in such a way that the k-space center is acquired at TE.

Due to the fast image acquisition, the EPI readout is used in several MRI techniques, although, it is prone to different kinds of artifacts. Many of these artifacts are caused by the low frequency difference between neighboring pixels (bandwidth per pixel) in the phase encoding direction. The bandwidth is determined by the time needed to induce the phase difference between neighboring pixels. In the readout direction, it is the inverse of the duration of a single frequency encoding gradient pulse and in the order of 2000-3000 Hz/pixel. In the phase encoding direction, the bandwidth is mainly determined by the time between two blips as this is the time needed to induce the phase difference between two pixels. In the phase encoding direction, the bandwidth is about 100 times lower than in the frequency encoding direction.

If a magnetic field inhomogeneity is present that creates a frequency difference in the order of the pixel bandwidth or higher, it leads to a displacement in the image. For example,

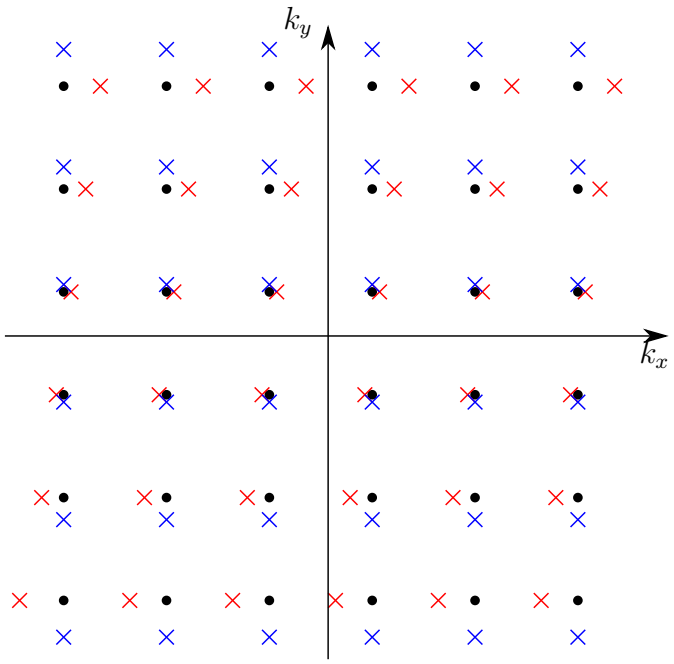

Figure 3.4: Comparison of assumed and actual k-space points. In the presence of an additional gradient, the actually acquired k-space points (shown as crosses) and the assumed ones (shown as dots) are not identical. In the case of a gradient in readout direction (here k_x, red crosses), there is a mismatch in readout direction which changes in the phase encoding direction. This leads to an image shearing. If there is a gradient in phase encoding direction, the mismatch is in that direction (here k_y, blue crosses) and leads to an image resizing. Designed after [JBP98].

the difference in the Larmor frequency of water and fat (chemical shift) at 3 T is about 440 Hz. With a pixel bandwidth of 40 Hz, this leads to a shift of 11 pixels, while in the readout direction, with a bandwidth of about 2000 Hz, the shift is below one pixel. An additional gradient during the whole EPI readout leads to image distortions for the same reason. The effects of a gradient along the readout or phase direction is shown in figure 3.4. In readout direction, an additional gradient leads to a sheared image, in the phase encoding direction to a different scaling and in the slice direction to a shift. A common reason for such residual gradients are eddy currents (section 3.4).

Since no spin echo is applied during the readout train, the main limitation for its duration is the $t_2^\star$-relaxation. This signal decay leads to a blurred image and shows that it can be advantageous to shorten the readout.

3.3.6 Partial Fourier Acquisition

The magnetization distribution $M_{xy}(\boldsymbol{r}, 0)$ (equation 3.8) is a real quantity, so its Fourier transform, that is the k-space signal, is hermitian:

$$S(-\boldsymbol{k}) = S^*(\boldsymbol{k}), \tag{3.14}$$

where * denotes the complex conjugate. Equation 3.14 shows that theoretically only half of the k-space needs to be acquired, but in reality, due to imperfections in the actual measurement, it is necessary to sample more. Such imperfections result from scanner vibrations, eddy currents, motion of the subject or random noise. The fraction of the k-space that is sampled is given by the partial Fourier factor. The advantage of partial Fourier encoding is the shortening of the EPI readout train and the therefore potentially shorter TE.

3.3.7 Parallel imaging

The basic idea of parallel imaging is to use several receive coils at different position to shorten the data acquisition. This is achieved by increasing the distance between neighboring k-space lines. According to equation 3.11, this reduces the FOV and can therefore lead to aliasing. The sensitivity profiles of the coils can be used to avoid or remove this aliasing. One approach for achieving this is called GRAPPA (generalized autocalibrating partially parallel acquisition) [GJH+02]. For GRAPPA, the sensitivity profiles of the individual coils are used to estimate the missing k-space information. The factor used for spreading the k-space line gives the acceleration that is achieved and is called GRAPPA factor in this work.

3.4 Eddy Currents

The use of time dependent magnetic fields $\boldsymbol{B}(t)$ leads to the induction of electric fields ($\boldsymbol{E}$), which is described by Faraday's induction law:

$$-\frac{\partial \boldsymbol{B}(t)}{\partial t} = \nabla \times \boldsymbol{E}. \tag{3.15}$$

These electric fields cause eddy currents in conducting materials, which cause a magnetic field that is opposed to the original magnetic field change, indicated by the minus sign (Lenz's law). These eddy currents can be induced in different parts of the scanner like gradient coils and the temperature shielding. The main source of eddy currents in MRI are the gradient pulses.

If not compensated for, eddy currents have different effects. First, the gradient that is actually applied is not identical to the nominal one, due to additional eddy currents in the gradient coils. This can be solved by pre-emphasis [JBDN87, VVB90, BGM91], where the currents through the coils are adjusted so that the resulting gradient pulse follows the intended time development. Second, eddy currents can induce additional magnetic fields in other conducting parts. These can be reduced by careful coil design [BM91] and the use of active shielding [MC86a, MC86b, MC87]. For active shielding, a set of additional coils is used, which is specifically designed to reduce the fringe fields of the primary gradient coils.

With these methods, the effect of eddy currents on MR images can be reduced, but when fast switching gradients with high amplitudes are used, eddy currents can still have significant effects. These residual eddy currents can be modeled by a number of inductively

coupled inductive- resistive (L-R-) circuits [VVB90, JWS90], which leads to eddy currents $I(t)$ that can be described by [BKZ04]

$$I(t) \propto \sum_i w_i \frac{\mathrm{d}G}{\mathrm{d}t} * \mathrm{e}^{-t/\tau_i}. \tag{3.16}$$

Equation 3.16 describes a convolution ($*$) of the time derivative of the gradient field with a multi-exponential decay. Each L-R-circuit in the model is weighted by w_i and is described by a decay constant τ_i.

The eddy currents can be calculated for trapezoidal gradient pulses $G(t)$ (equation 3.3), save for the proportionality factor. In this case, $\frac{\mathrm{d}G}{\mathrm{d}t}$ is only non zero during the ramp times of duration r. Under the assumption of a gradient starting time $t_0 = 0$, the resultant eddy current is given by

$$I(T) \propto \sum_i \left(w_i \int_0^T \frac{\mathrm{d}G(t)}{\mathrm{d}t} \, \mathrm{e}^{-(T-t)/\tau_i} \, \mathrm{d}t \right) \tag{3.17}$$

$$= \sum_i \left(w_i \int_0^r \frac{g}{r} \, \mathrm{e}^{-(T-t)/\tau_i} \, \mathrm{d}t - \int_\delta^{\delta+r} \frac{g}{r} \, \mathrm{e}^{-(T-t)/\tau_i} \, \mathrm{d}t \right). \tag{3.18}$$

These integrals can be solved and the eddy current for a time T after the gradient pulse is given by

$$I(T) \propto \sum_i w_i \frac{g\tau_i}{r} \left(\mathrm{e}^{r/\tau_i} - 1\right) \mathrm{e}^{-T/\tau_i} \left(\mathrm{e}^{\delta/\tau_i} - 1\right). \tag{3.19}$$

The proportionality factor and the individual weighting factors are system dependent. In many applications, only one decay time is assumed [RHWW03, Fin09]. Normally, these considerations are used to null or to at least minimize eddy currents, therefore the proportionality factor is not needed. The eddy currents for a gradient pulse with a different starting time t_0 can easily be calculated by multiplying each summand in equation 3.19 with the respective factor e^{t_0/τ_i}.

3.5 Concomitant Fields

So far, linear gradient fields were assumed, which is not actually true. This can be seen by looking at Maxwell's equations for a magnetic field $\boldsymbol{B}$:

$$\nabla \cdot \boldsymbol{B} = 0 \tag{3.20}$$

$$\nabla \times \boldsymbol{B} = \mu_0 \boldsymbol{J} + \mu_0 \epsilon_0 \frac{\partial \boldsymbol{E}}{\partial t}, \tag{3.21}$$

with the electric field $\boldsymbol{E}$, the current density $\boldsymbol{J}$, the vacuum permeability μ_0 and permittivity ϵ_0. In MRI, the current density and the displacement current density $\mu_0\epsilon_0 \frac{\partial \boldsymbol{E}}{\partial t}$ can

usually be neglected in the imaging volume and are therefore set to zero. With the wanted gradient field $\boldsymbol{G} = \nabla B_z$, Maxwell's equations (3.20 and 3.21) can be written as

$$\frac{\partial B_x}{\partial x} + \frac{\partial B_y}{\partial y} + \frac{\partial B_z}{\partial z} = 0 \tag{3.22a}$$

$$G_\perp = \frac{\partial B_x}{\partial y} = \frac{\partial B_y}{\partial x} \tag{3.22b}$$

$$\frac{\partial B_y}{\partial z} = \frac{\partial B_z}{\partial y} \tag{3.22c}$$

$$\frac{\partial B_z}{\partial x} = \frac{\partial B_x}{\partial z} \tag{3.22d}$$

$$G_x = \frac{\partial B_z}{\partial x} \tag{3.22e}$$

$$G_y = \frac{\partial B_z}{\partial y} \tag{3.22f}$$

$$G_z = \frac{\partial B_z}{\partial z}, \tag{3.22g}$$

where in equation 3.22b the transverse gradient $G_\perp$ was defined. There are nine partial derivatives in equations 3.22a-3.22g but only seven equations, leading to two more free parameters that are chosen as

$$\alpha = -\frac{1}{G_z}\left(\frac{\partial B_x}{\partial x}\right) \tag{3.23}$$

$$1 - \alpha = -\frac{1}{G_z}\left(\frac{\partial B_y}{\partial y}\right). \tag{3.24}$$

If all these parameters are considered, and without considering higher order terms, the magnetic field is given by

$$\begin{pmatrix} B_x \\ B_y \\ B_z - B_0 \end{pmatrix} = \begin{pmatrix} -\alpha G_z & G_\perp & G_x \\ G_\perp & (\alpha - 1)G_z & G_y \\ G_x & G_y & G_z \end{pmatrix} \begin{pmatrix} x \\ y \\ z \end{pmatrix}. \tag{3.25}$$

This equation shows that even if B_0 and the gradients are all applied along the z-direction, the magnetic field components in x- and y-direction are non-zero, which has two implications: first, the magnetic field is not aligned with the z-direction anymore and second, the amplitude must be calculated according to

$$B(x, y, z) = \sqrt{B_x^2 + B_y^2 + B_z^2}. \tag{3.26}$$

In common cylindrical gradient coils it can be assumed that $G_\perp \approx 0$ and $\alpha \approx 0.5$ [BKZ04]. The Taylor expansion of equation 3.26 can be used to find the additional magnetic field B_c, called concomitant field:

$$B(x, y, z) = B_0 + xG_x + yG_y + zG_z + B_c \tag{3.27}$$

$$B_c \approx \frac{1}{2B_0}\left(\left(zG_x - \frac{xG_z}{2}\right)^2 + \left(zG_y - \frac{yG_z}{2}\right)^2\right), \tag{3.28}$$

which is given here with terms up to the second order. The sign of B_c in the second order is independent of the actual gradient direction, meaning its effects cannot be reversed by just applying a gradient in opposite direction. The concomitant field amplitude rises with distance from the gradient center, which is located in the center of the MRI machine, thus B_c gets the more important the larger the FOV is. It introduces a spatially dependent phase in the image, which can only be compensated if at least one refocusing RF pulse is used. If the phase is not properly refocused and long gradient pulses with high amplitudes are used, it can lead to signal voids.

The signal is influenced by the additional phase Φ_c caused by the concomitant field of a gradient pulse, which is given by

$$\Phi_c(\boldsymbol{r}, t) = \gamma \int_0^t B_c(\boldsymbol{r}, t')\mathrm{d}t'. \tag{3.29}$$

As an example, it is assumed that a gradient pulse is applied in z-direction. The phase is then proportional to:

$$\Phi_c(t) \propto \int_0^t G_z(t')^2(x+y)^2\mathrm{d}t' = (x+y)^2 \int_0^t G_z(t')^2\mathrm{d}t', \tag{3.30}$$

where the equal sign holds for stationary particle. This integral can be solved for a trapezoidal gradient pulse (equation 3.3), resulting in:

$$\Phi_c = (\delta - \frac{p}{3})g^2(x+y)^2. \tag{3.31}$$

3.6 Imaging Sequence and Contrast

The combination of RF pulses and gradient pulses determines the image contrast in MRI and is called a sequence. It also defines the k-space acquisition scheme. Sequences can be characterized by these properties. For example, if a refocusing RF pulse is used, it is called a spin echo sequence or if a EPI readout is used, it is a EPI sequence.

To visualize a sequence, the sequence diagram can be used, which shows the RF and gradient pulses. An example for a spin echo EPI sequence can be seen in figure 3.3. For the rest of this work, RF pulses are indicated by a straight vertical line at the isodelay point, which is given by the center of the corresponding slice selection gradient pulse and most imaging gradients are omitted.

Another way to classify sequences is by the image contrast they produce. The basic image contrasts in MRI are based on the spin density ρ and the relaxation times T_1, T_2 and $T_2^\star$. The spin density always influences the image contrast, while the weighting of the relaxation times can be regulated by the sequence timing.

A T_1-weighting is achieved, for example, if the repetition time (TR), that is the time between two successive excitations, is in the order of T_1. In this case, the longitudinal magnetization is only partly regained before a new excitation. The regained part is larger for shorter T_1 values and they appear brighter. To minimize the T_1 weighting long TR need to be chosen.

For a T_2-weighted image, a spin echo sequence is needed, otherwise it can only be a $T_2^\star$-weighting. If TE is in the order of T_2, tissues with different T_2 show a different degree of transversal relaxation and hence a different signal intensity. Areas with a longer T_2 appear brighter in those images. This effect is minimal for short TE.

It follows that images with long TR and short TE show a contrast mainly determined by ρ.

4 Basics: Diffusion Weighted MRI

In this chapter, the basic principles of diffusion weighted MRI (diffusion weighted imaging (DWI)) are looked at. At first, a few general properties of the diffusion process are considered before the measurements with MRI are described. For a more detailed look, there are several books available, for example [Jon11, Mor07, BKZ04]. The last sections in this chapter deal with some special concepts and models of DWI.

4.1 The Diffusion Process

4.1.1 Free Diffusion

The name diffusion is used for the random Brownian motion that is observed for small particles. In many applications, this random motion is considered for transport processes along a concentration gradient $\nabla n(\boldsymbol{r}, t)$, leading to a particle flux $\boldsymbol{j}$. This was described by Fick [Fic55]:

$$\boldsymbol{j}(\boldsymbol{r}, t) = -D\nabla n(\boldsymbol{r}, t). \tag{4.1}$$

Equation 4.1 shows that the particle flux is in the direction opposite to the concentration gradient. The proportionality constant D is called diffusion coefficient, which is a scalar in case of an isotropic medium. Fick's first law (equation 4.1) together with the continuity equation:

$$\frac{\partial n(\boldsymbol{r})}{\partial t} = -\nabla \cdot \boldsymbol{j}(\boldsymbol{r}, t) \tag{4.2}$$

leads to Fick's second law:

$$\frac{\partial n(\boldsymbol{r}, t)}{\partial t} = \nabla D \nabla n(\boldsymbol{r}, t). \tag{4.3}$$

These equations were developed to describe a motion with a non-constant concentration of particles in solution. Einstein showed that the same laws govern self-diffusion [Ein05], without any concentration gradient and without the need of a solvent. Equation 4.3 is known as the diffusion equation and in the presented form also valid for a spatially varying diffusion coefficient.

The solution of the diffusion equation for the initial condition of all particles at the initial position $\boldsymbol{r_0} = \boldsymbol{r}(t_0)$ (that is $n(\boldsymbol{r}, 0) = \delta_G(\boldsymbol{r} - \boldsymbol{r_0}$ with the Dirac function δ_G), no boundary conditions and a constant diffusion coefficient is given by:

$$n(\boldsymbol{r}, t) = \frac{1}{\sqrt{4\pi D t}^d} \mathrm{e}^{-\frac{(\boldsymbol{r}-\boldsymbol{r_0})^2}{4Dt}}, \tag{4.4}$$

where d gives the dimensions of the diffusive motion looked at. This solution describes the fact that the particles spread out over time. The spreading is described by a Gaussian bell curve. Its width is given by the standard deviation σ, which widens with time. It can be identified with the mean squared displacement $\langle \boldsymbol{r}^2 \rangle$ and is given by the Einstein equation which in one dimension reads:

$$\sigma_x(t) = \langle x^2 \rangle = 2Dt. \tag{4.5}$$

For free diffusion, that is without any boundaries, of water at body temperature, the diffusion coefficient is found to be $D_{\text{free water}} \approx 3\,\mu\text{m}^2/\text{ms}$. This leads to a mean displacement length $\sqrt{\langle x^2 \rangle}$ in 50 ms of about 17 μm. It is on the length scale of human cells, why it is possible to use diffusion measurements to infer information on the tissue microstructure.

4.1.2 Diffusion with Boundaries

The solution for the diffusion equation given in equation 4.4 is valid for free diffusion. In tissue, the diffusion is not free, as there are, for example, cell membranes or macromolecules. These boundaries restrict the particle path, therefore reducing $\langle x^2 \rangle$ and making the diffusion non-Gaussian. Due to the boundaries, the displacement steps of a particle are no longer uncorrelated. The particles that experience this effect are mostly those in a distance of $\sqrt{2DT_D}$ of a boundary, where T_D describes the duration of the diffusion experiment. For short diffusion times this is only a small fraction of the particles, while most exhibit Gaussian diffusion so that it is a good approximation.

For long diffusion times in open geometries, the correlation is lost and the central limit theorem can be applied, leading again to a Gaussian diffusion with reduced diffusion coefficient. Such an open geometry is, for example, the extracellular space. The diffusion in different time limits is illustrated in figure 4.1.

If the boundaries are additionally ordered, as, for example, cell membranes in coherent nerve fibers in the brain, they induce a directional dependence on the diffusion coefficient. This can be described by introducing the diffusion tensor $\underline{\underline{D}}$. In the case of Gaussian diffusion, equation 4.5 can be used to define the tensor elements D_{ij} as:

$$D_{ij} = \frac{\langle R_i(T_D) R_j(T_D) \rangle}{2T_D}. \tag{4.6}$$

Here, $\boldsymbol{R}(T_D)$ was introduced which is given by the displacement $\boldsymbol{R}(T_D) = \boldsymbol{r}(T_D) - \boldsymbol{r_0}$ and its components are denoted as $R_{i,j}$ with i and j can be 1, 2 or 3. The diffusion tensor can be written as a symmetric 3×3 matrix, as can be seen from equation 4.6, leading to the conclusion that it has six independent parameters, three for the direction and three for the strength.

If the limits of Gaussian diffusion are not met, equation 4.6 is still used, but $\underline{\underline{D}}(T_D)$ becomes time dependent.

One case where the diffusion is not Gaussian are closed pores. A pore is considered to be filled with diffusing, NMR-visible medium, without any NMR-visible medium on the outside. The diffusion and its measurement in such geometries are described in detail, for

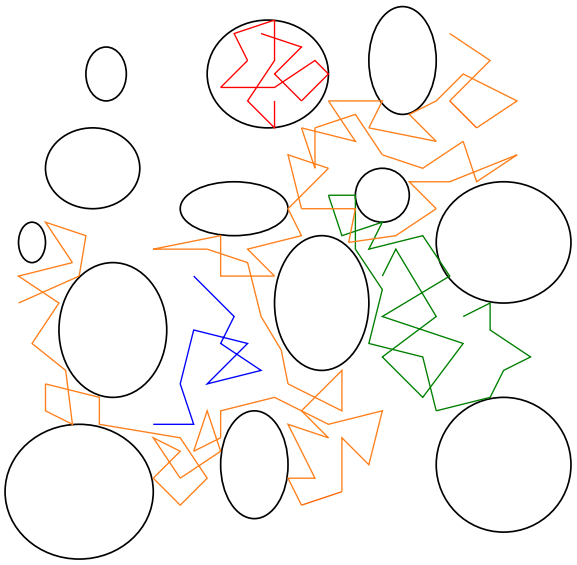

Figure 4.1: Diffusion for different time scales. For short diffusion times (blue), only few particles collide with the walls. At longer times (green), the particles collide several times with the walls. For very long diffusion times (orange), the overall motion is less influenced by the local geometry. In red the diffusion inside a pore is demonstrated.

example, in [Gre07]. In human tissue such pores do not exist, although intracellular space is sometimes considered as such. There is always extracellular space and exchange with the intracellular compartment, effectively leading to an open geometry. The assumption of a closed pore can nevertheless be a good approximation if the mean abode times are long compared to the diffusion time T_D. The time constants for exchange processes in the human brain can go up to over a second [NLvW+13], while typical diffusion times are around 50 ms.

4.2 Measurement of Diffusion with MRI

4.2.1 Bloch-Torrey Equations

The basic Bloch equations (2.24a-2.24b) can be extended with a term describing the diffusion, which is given by the diffusion equation 4.3. This was done by Torrey [Tor56], yielding the Bloch-Torrey equations:

$$\frac{\partial \boldsymbol{M}}{\partial t} = \gamma \boldsymbol{M} \times \boldsymbol{B} - \begin{pmatrix} M_x/T_2 \\ M_y/T_2 \\ (M_z - M_0)/T_1 \end{pmatrix} + \nabla(\underline{\underline{D}} \nabla \boldsymbol{M}). \tag{4.7}$$

For the complex transversal magnetization $M_{xy} = M_x + iM_y$ during the application of a gradient $\boldsymbol{G}(t)$, the equation yields

$$\frac{\partial M_{xy}}{\partial t} = -i\gamma M_{xy}(B_0 + \boldsymbol{r}\cdot\boldsymbol{G}(t)) - \frac{M_{xy}}{T_2} + \nabla(\underline{\underline{D}}\nabla M_{xy}). \tag{4.8}$$

This equation can be solved for free diffusion. The precession with the Larmor frequency $\omega_0 = \gamma B_0$ and the T_2-relaxation can be removed $m_{xy}(\boldsymbol{r},t) = M_{xy}(\boldsymbol{r},t)\mathrm{e}^{i\gamma B_0 + t/T_2}$:

$$\frac{\partial m_{xy}}{\partial t} = -i\gamma m_{xy}\boldsymbol{r}\cdot\boldsymbol{G}(t) + \nabla(\underline{\underline{D}}\nabla m_{xy}). \tag{4.9}$$

Magnitude and phase of m_{xy} can be separated by using the substitution $m_{xy}(\boldsymbol{r},t) = M(t)\mathrm{e}^{-i\boldsymbol{r}\cdot\boldsymbol{k}(t)}$, where $\boldsymbol{k}(t)$ follows the same definition as the wave vector $\boldsymbol{k}(t)$ (equation 3.7), that is $\boldsymbol{k}(t) = \gamma\int_0^t \boldsymbol{G}(t')\mathrm{d}t'$. The signal is proportional to the magnitude $M(t)$, whose time derivative can be calculated with the help of equation 4.9:

$$\begin{aligned}
\frac{\partial M(t)}{\partial t} &= \left(\frac{\partial m_{xy}(t)}{\partial t} + m_{xy} i\boldsymbol{r}\cdot\frac{\partial \boldsymbol{k}(t)}{\partial t}\right)\mathrm{e}^{i\boldsymbol{r}\cdot\boldsymbol{k}(t)} && \text{(4.10a)}\\
&= \left(\frac{\partial m_{xy}(t)}{\partial t} + m_{xy} i\gamma\boldsymbol{r}\cdot\boldsymbol{G}(t)\right)\mathrm{e}^{i\boldsymbol{r}\cdot\boldsymbol{k}(t)} && \text{(4.10b)}\\
&= \left(\nabla(\underline{\underline{D}}\nabla m_{xy})\right)\mathrm{e}^{i\boldsymbol{r}\cdot\boldsymbol{k}(t)} = \left(\nabla(\underline{\underline{D}}\nabla M(t)\mathrm{e}^{-i\boldsymbol{r}\cdot\boldsymbol{k}(t)})\right)\mathrm{e}^{i\boldsymbol{r}\cdot\boldsymbol{k}(t)} && \text{(4.10c)}\\
&= -M(t)\boldsymbol{k}^T(t)\underline{\underline{D}}\boldsymbol{k}(t). && \text{(4.10d)}
\end{aligned}$$

The solution of this differential equation can be calculated by integration, if no boundary conditions are assumed.

$$M(\mathrm{TE}) = M(0)\exp\left(-\int_0^{\mathrm{TE}} \boldsymbol{k}(\boldsymbol{t'})^T\underline{\underline{D}}\boldsymbol{k}(\boldsymbol{t'})\mathrm{d}t'\right). \tag{4.11}$$

For a scalar diffusion coefficient, the definition of the b-value is straightforward

$$b = \int_0^{TE}\boldsymbol{k}(t)^T\boldsymbol{k}(t)\mathrm{d}t = \int_0^{TE}\boldsymbol{k}(t)^2\mathrm{d}t = \int_0^{TE}\gamma^2\left(\int_0^t \boldsymbol{G}(t')\mathrm{d}t'\right)^2\mathrm{d}t. \tag{4.12}$$

The b-value describes the strength of the diffusion encoding. The signal attenuation due to this diffusion encoding is given by

$$S(\mathrm{TE},b) = \frac{M(\mathrm{TE},b)}{M(0)} = \mathrm{e}^{-bD}, \tag{4.13}$$

where the normalized signal was used. For a diffusion tensor, equation 4.11 needs to be considered. In this case, the b-value definition can be kept with a few changes. A gradient with a constant direction but varying amplitude can be written as $\boldsymbol{G}(t) = G(t)\boldsymbol{u}$, where $G(t)$ describes the temporal profile of the gradient amplitude and $\boldsymbol{u}$ is the normalized direction ($\|\boldsymbol{u}\| = 1$). This gives a b-value as in the last term in equation 4.12, only with $G(t)$ instead of $\boldsymbol{G}(t)$. The signal reduction is then given by $S(\mathrm{TE},b) = \exp(-b\boldsymbol{u}^T\underline{\underline{D}}\boldsymbol{u})$.

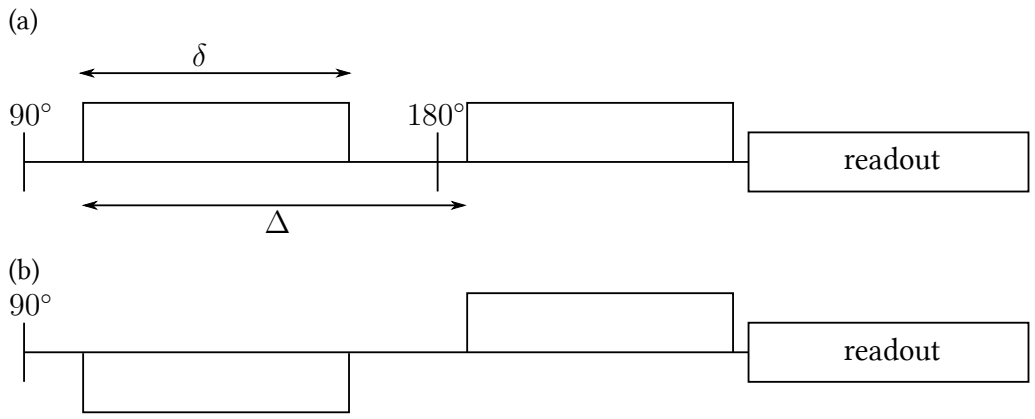

Figure 4.2: Stejskal-Tanner sequence. (a) The sequence scheme that was introduced by Stejskal and Tanner to measure the diffusion coefficient. (b) The effective gradient scheme of the Stejskal-Tanner sequences.

4.2.2 Diffusion Sequences

Stejskal-Tanner Sequence

Stejskal and Tanner proposed a sequence to measure the diffusion by using two gradient pulses of limited duration together with a spin echo sequence [ST65]. The diffusion encoding is shown in figure 4.2a. For calculating the b-value, the refocusing RF pulse needs to be considered. This can be done by introducing the effective gradient G_{eff}, which is shown in figure 4.2b. The effective gradient scheme is determined by flipping the gradient amplitude once for each refocusing pulse before it. Mathematically this can be done by multiplying the gradient amplitude with a factor of $s(t) = \pm 1$ which changes the sign for every refocusing pulse. With this definition and equation 4.12, the b-value for trapezoidal gradients (equation 3.3) can be calculated to:

$$b = \gamma^2 g^2 \left(\delta^2 \left(\Delta - \frac{\delta}{3} \right) - \frac{\delta^2 p}{6} + \frac{p^3}{30} \right) \tag{4.14}$$

The first diffusion encoding gradient in the Stejskal-Tanner sequence induces a spatially dependent phase, which is refocused by the second gradient for stationary particles. Therefore, the first gradient is also called the dephaser and the second one the rephaser. If the particles are moving, the rephasing is not perfect.

Narrow Pulse Approximation

In the Stejskal-Tanner sequence, the gradients exhibit a finite duration. Often, the $\boldsymbol{q}$-vector is used to describe the signal. It is defined as

$$\boldsymbol{q} = \gamma \int_{t_0}^{T_G} G(t)\boldsymbol{u}\mathrm{d}t, \tag{4.15}$$

which for trapezoidal gradients is $q = \gamma g \delta$. The usefulness of this definition can be understood when considering that the normalized signal for diffusion can be considered as the average over all random paths in the time T_D, indicated by $\langle \cdot \rangle$, with the acquired phase:

$$S = \langle \mathrm{e}^{-i\Phi} \rangle = \langle \mathrm{e}^{-i\gamma \int_0^T \boldsymbol{G}(t)\cdot\boldsymbol{r}(t)\mathrm{d}t} \rangle. \tag{4.16}$$

If infinitesimal short gradients with constant q are assumed at the times 0 and T_D, the signal attenuation is only determined by the particle positions at those two times:

$$S = \langle \mathrm{e}^{-i\Phi} \rangle = \left\langle \mathrm{e}^{-i\boldsymbol{q}\cdot(\boldsymbol{r}(T)-\boldsymbol{r}(0)} \right\rangle = \left\langle \mathrm{e}^{-i\boldsymbol{q}\cdot\boldsymbol{R}} \right\rangle. \tag{4.17}$$

where the definition $\boldsymbol{R}$ from section 4.1.2 was used. This approximation is used in the q-space imaging for a wide variety of applications [CG90, CCM+91, Tuc04] and is also known as narrow pulse approximation.

Equation 4.17 can be generalized to gradients with finite gradient lengths [MH95, Jes12] by the use of the center of the generalized mass $\boldsymbol{r}^{\delta}_{\boldsymbol{cm}}(t_0)$ of a random walk between $\boldsymbol{r}(t_0)$ and $\boldsymbol{r}(t_0 + \delta)$:

$$\boldsymbol{r}^{\delta}_{cm}(t_0) = \frac{1}{\delta} \int_{t_0}^{t_0+\delta} \boldsymbol{r}(t) w(t) \mathrm{d}t. \tag{4.18}$$

Here a weighting $w(t)$ is defined, which is given by the relative amplitude of the gradient profile $\boldsymbol{G}(t)$. $w(t)$ must fulfill $\int_0^{T_G} w(t) = 1$. The signal (equation 4.16) can then be written as

$$S = \left\langle \mathrm{e}^{-i\boldsymbol{q}\cdot\left(\frac{1}{\delta}\int_0^{\delta}\boldsymbol{r}(t)w(t)\mathrm{d}t - \frac{1}{\delta}\int_{\Delta}^{\Delta+\delta}\boldsymbol{r}(t)w(t)\mathrm{d}t\right)} \right\rangle = \left\langle \mathrm{e}^{-i\boldsymbol{q}\cdot(\boldsymbol{r}^{\delta}_{\boldsymbol{cm}}(\Delta)-\boldsymbol{r}^{\delta}_{\boldsymbol{cm}}(0)} \right\rangle = \left\langle \mathrm{e}^{-i\boldsymbol{q}\cdot\boldsymbol{R}^{0,\Delta}_{\boldsymbol{cm}}} \right\rangle \tag{4.19}$$

where $\boldsymbol{R}^{0,\Delta}_{\boldsymbol{cm}} = \boldsymbol{r}^{\delta}_{\boldsymbol{cm}}(\Delta) - \boldsymbol{r}^{\delta}_{\boldsymbol{cm}}(0)$ was introduced. This equation has the same form as equation 4.17 and the derivations can be done with both in the same way.

4.2.3 Diffusion Tensor in MRI

Measurement

The diffusion tensor has six independent parameters, as mentioned in section 4.1.2. This shows that at least six measurements with non-collinear gradient directions $\boldsymbol{u_i}$ are needed for the measurement of the whole tensor. In each of the measurements, an apparent diffusion coefficient (ADC) is determined, which is given by

$$\mathrm{ADC}_i = \boldsymbol{u_i}^T \underline{\underline{D}} \boldsymbol{u_i}. \tag{4.20}$$

and leads to the signal

$$S_i(b) = S(0)\mathrm{e}^{-b\mathrm{ADC}_i} \tag{4.21}$$

For the determination of ADC_i two measurements are needed, with two different b-values. In many cases, one is done without diffusion weighting ($b = 0$). In total, seven measurements are needed to determine the diffusion tensor.

For the calculation with more than the seven measurements, a pseudo-inverse matrix can be used to minimize the quadratic error [Kin06]. To show this, the independent parameters are reorganized in a vector $\boldsymbol{d}$:

$$\boldsymbol{d} = (D_{xx}, D_{yy}, D_{zz}, D_{xy}, D_{xz}, D_{yz})^T \tag{4.22}$$

and the gradient direction is rewritten as $\boldsymbol{U}$:

$$\boldsymbol{U} = (u_x^2, u_y^2, u_z^2, u_x u_y, u_x u_z, u_y u_z)^T. \tag{4.23}$$

The result of a single measurement with b_i and $\boldsymbol{U_i}$ is then given by

$$\log S_i = \log S_0 - b_i \boldsymbol{U_i} \cdot \boldsymbol{d}. \tag{4.24}$$

If n measurements are done, they can be combined in the form:

$$\begin{pmatrix} \log S_1 \\ \vdots \\ \log S_n \end{pmatrix} = \begin{pmatrix} \log S(0) \\ \vdots \\ \log S(0) \end{pmatrix} - \begin{pmatrix} b_1 \boldsymbol{U_1}^T \\ \vdots \\ b_n \boldsymbol{U_n}^T \end{pmatrix} \cdot d = \underline{\underline{B}} \cdot \boldsymbol{d}. \tag{4.25}$$

The determination of $\boldsymbol{d}$ and thus $\underline{\underline{D}}$ requires only the determination of the pseudo-inverse of $\underline{\underline{B}}$.

Since this measurement of $\underline{\underline{D}}$ is based on Gaussian diffusion and therefore on equation 4.6 it gets time-dependent in the presence of boundaries.

Rotationally Invariant Parameters

There are several rotationally invariant parameters that can be derived from the diffusion tensor. Some of the most common ones are the mean diffusivity (MD) and the fractional anisotropy (FA). The MD is given by the trace of $\underline{\underline{D}}$:

$$\mathrm{MD} = \frac{\mathrm{tr}(\underline{\underline{D}})}{3} = \frac{D_{xx} + D_{yy} + D_{zz}}{3} = \overline{\lambda_i}, \tag{4.26}$$

where the overbar indicates the mean and the λ_i are the three eigenvalues of $\underline{\underline{D}}$. The FA is given by

$$\mathrm{FA} = \sqrt{\frac{(\lambda_1 - \lambda_2)^2 + (\lambda_1 - \lambda_3)^2 + (\lambda_2 - \lambda_3)^2}{2(\lambda_1^2 + \lambda_2^2 + \lambda_3^2)}} = \sqrt{\frac{3}{2}} \sqrt{\frac{\mathrm{var}(\lambda_i)}{\overline{\lambda_i^2}}}, \tag{4.27}$$

where $\mathrm{var}(\lambda_i)$ is the variance of the eigenvalues. The FA can take values between 0 and 1 and is a measure of the diffusion anisotropy. If all eigenvalues are equal, that is the diffusion is isotropic, the FA is 0. If only one eigenvalue is non-zero, that is diffusion is only possible in one direction, the FA becomes 1.

The eigenvector associated with the largest eigenvalue determines the main diffusion direction and is used to visualize nerve fibers in the brain. This is done by encoding its direction in the colors red (left-right), green (up-down) and blue (through plane) and the brightness by the FA. The color choices are given for a transversal plane.

4.2.4 Cumulant Expansion

Equation 4.11 was derived without boundary conditions. To examine the diffusion signal in more complicated geometries, for example in vivo, an expansion of the signal is helpful:

$$S = \left\langle \mathrm{e}^{-i\boldsymbol{q}\cdot\boldsymbol{R}} \right\rangle = \left\langle \mathrm{e}^{-i\Phi} \right\rangle = \sum_{n=0}^{\infty} \frac{(-i)^n}{n!} \left\langle \Phi^n \right\rangle , \tag{4.28}$$

with $\Phi = \boldsymbol{q} \cdot \boldsymbol{R}$ in the case of short gradients. This equation is the same for finite gradient durations with the corresponding $\boldsymbol{R_{cm}}$, but, for simplicity, the subscripts are dropped here. Φ is a random variable and follows a probability density function and can be described by these terms [vK08, JC10]. The term $\langle \Phi^n \rangle$ is known as the n-th moment of the distribution. The zeroth moment is 1 and the first moment is the mean value. The second moment depends on the variance and the mean value, which is not an ideal way to describe the width of a distribution. A better way to represent the signal is by the cumulant expansion:

$$\log S = \log \left\langle \mathrm{e}^{-i\Phi} \right\rangle = \sum_{n=0}^{\infty} \frac{(-i)^n}{n!} \left\langle \Phi^n \right\rangle_C , \tag{4.29}$$

where $\langle \cdot \rangle_C$ denotes the cumulant. They can be calculated from the moments by subtracting the trivial contributions. The first cumulant is by definition the same as the mean and the second one is given by the variance $\langle \Phi^2 \rangle_C = \sigma = \langle \Phi^2 \rangle - \langle \Phi \rangle^2$. The fourth order cumulant is in terms of moments given by $\langle \Phi^4 \rangle_C = \langle \Phi^4 \rangle - 4 \langle \Phi^3 \rangle \langle \Phi \rangle - 3 \langle \Phi^2 \rangle^2 + 12 \langle \Phi^2 \rangle \langle \Phi \rangle^2 - 6 \langle \Phi \rangle^4$.

In DWI the odd cumulants are often taken to be zero, which is the case without directed flow and for the gradient profiles usually employed for NMR diffusion measurements. This leaves the even cumulants. For many applications, it is enough to consider the first few terms of the expansion, which is given in Stejskal-Tanner-like sequences by

$$\log S \approx -\frac{1}{2} \left\langle \Phi^2 \right\rangle_C + \frac{1}{24} \left\langle \Phi^4 \right\rangle_C = -\frac{1}{2} q_i q_j \left\langle R_i R_j \right\rangle_C + \frac{1}{24} q_i q_j q_k q_l \left\langle R_i R_j R_k R_l \right\rangle_C . \tag{4.30}$$

The Einstein summing convention has been applied here, where there is a summation over each pair of identical indices in a product. The second order cumulant can be identified with the diffusion tensor (equation 4.6) if one keeps in mind that here $\langle \Phi \rangle = 0$ and thus $\langle R_i R_j \rangle_C = \langle R_i R_j \rangle = 2 D_{ij}(T_D) T_D$. The forth order term is given by the kurtosis $K = \frac{\langle \Phi^4 \rangle_C}{\langle \Phi^2 \rangle_C^2} = \frac{\langle \Phi^4 \rangle}{\langle \Phi^2 \rangle^2} - 3$. With these observations the signal is, for isotropic diffusion, given by

$$\log S \approx -q^2 T_D D(T_D) + \frac{1}{6} q^4 T_D^2 D(T_D)^2 K(T_D). \tag{4.31}$$

For a gaussian distribution, the kurtosis is zero. This shows that for low diffusion encoding strengths, the diffusion can be approximated by gaussian diffusion in DWI.

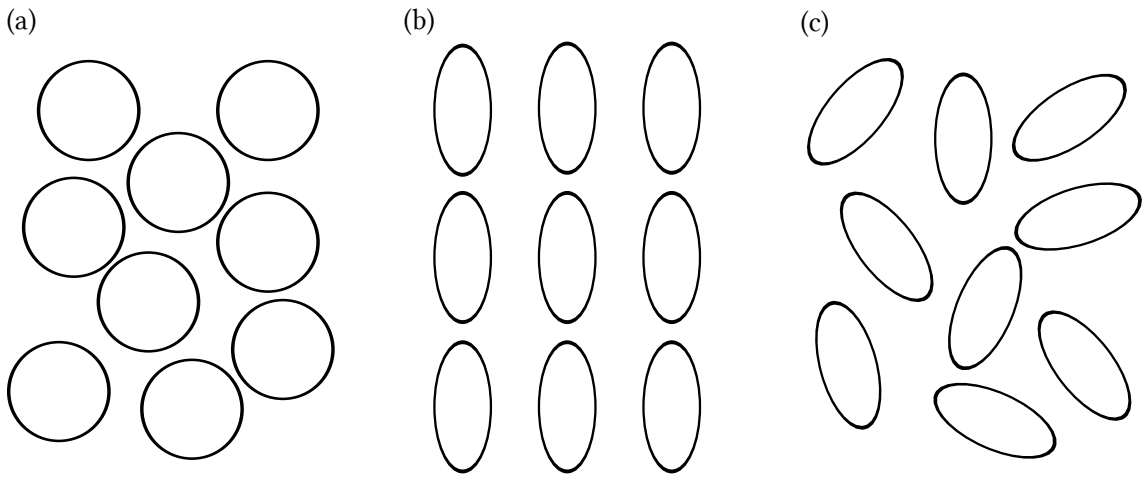

Figure 4.3: Comparison of microscopic and macroscopic anisotropy. It is assumed that there are only NMR-visible particles inside the pores. Standard diffusion tensor measurements in a volume containing all pores would lead to no anisotropy in cases (a) and (c), even though (c) does show single pore anisotropy (called microscopic anisotropy). In the case of coherently ordered, microscopically anisotropic pores (b) the FA is non-zero.

4.3 Double Diffusion Encoding

4.3.1 General Considerations

The measured diffusion tensor for one pixel in MRI depends on the underlying microstructure. It can therefore be a powerful tool for determining parameters thereof. Nevertheless, it also has a few drawbacks, as it is, for example, averaged over the whole volume element (voxel). One such drawback is the anisotropy measure. To illustrate this, simple two-dimensional example geometries are considered in figure 4.3. If the microstructure is ordered, the FA represents the underlying anisotropy well, but if the order is not given, the FA goes to zero, although the single diffusion compartments are still anisotropic. One prominent case in vivo where this happens is two crossing nerve fibers in the brain. With the diffusion tensor, it can not be decided if a loss of FA is due to a loss of coherent ordering or due to a loss of fibers and thus a larger a amount of particles diffusing isotropically.

This problem can be solved by the application of multiple diffusion encodings (figure 4.4), which was already suggested in 1995 [Mit95]. The derivation is only strictly true for closed pores, but, as mentioned in section 4.1.2, can be applied in vivo for reasonable timing parameters.

Two separate diffusion encodings can be used to make the signal dependent on the actual microscopic anisotropy. Such sequences are called double diffusion encoding (DDE) sequences. The derivation of the properties follows mostly [Jes12, JLSD13] and uses the narrow pulse approximation (section 4.2.2), but can be generalized to finite gradient durations by the center of mass approach. The two diffusion encodings are characterized by $\boldsymbol{q_1}$

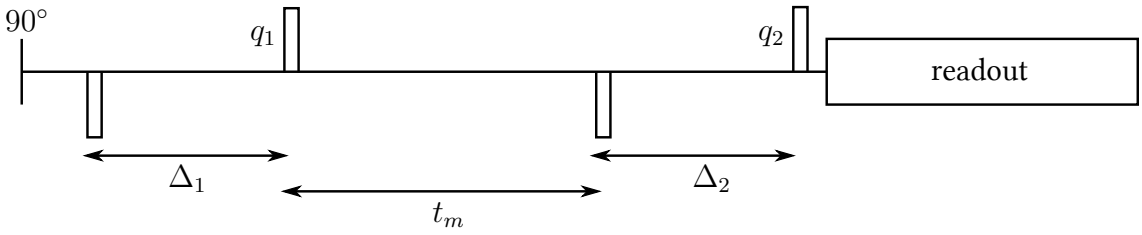

Figure 4.4: Effective gradient scheme for double diffusion encoding. The diffusion encodings shown here are defined to be parallel.

and $\boldsymbol{q_2}$. It is assumed that both encodings have the same separation of the gradient pulses Δ and are a time t_m apart, called the mixing time (figure 4.4). The corresponding displacement vectors are denoted with $\boldsymbol{R_1} = \boldsymbol{r}(\Delta) - \boldsymbol{r}(0)$ and $\boldsymbol{R_2} = \boldsymbol{r}(2\Delta + t_m) - \boldsymbol{r}(\Delta + t_m)$. The signal is given by an equation similar to equation 4.17:

$$S(\boldsymbol{q_1}, \boldsymbol{q_2}) = \left\langle \mathrm{e}^{-i(\boldsymbol{q_1}\cdot\boldsymbol{R_1} + \boldsymbol{q_2}\cdot\boldsymbol{R_2})} \right\rangle, \tag{4.32}$$

where the effective gradient directions (including refocusing pulses), where used (figure 4.4) and thus $\boldsymbol{q_1}$ and $\boldsymbol{q_2}$ are

$$\boldsymbol{G_1}(t) = \frac{\boldsymbol{q_1}}{\gamma\delta}(-\delta_G(t) + \delta_G(t-\Delta)) \tag{4.33a}$$

$$\boldsymbol{G_2}(t) = \frac{\boldsymbol{q_2}}{\gamma\delta}(-\delta_G(t-2\Delta) + \delta_G(t-2\Delta-t_m)), \tag{4.33b}$$

with the Dirac function $\delta_G(t)$. The signal can be expanded in cumulants:

$$\begin{aligned}
\log S(\boldsymbol{q_1}, \boldsymbol{q_2}) \approx & -\frac{1}{2}(q_{1i}q_{1j} - q_{2i}q_{2j}) \left\langle R_{1i}R_{1j}\right\rangle_C - q_{1i}q_{2j} \left\langle R_{1i}R_{2j}\right\rangle_C \\
& + \frac{1}{24}(q_{1i}q_{1j}q_{1k}q_{1l} + q_{2i}q_{2j}q_{2k}q_{2l}) \left\langle R_{1i}R_{1j}R_{1k}R_{1l}\right\rangle_C \\
& + \frac{1}{4}(q_{1i}q_{1j}q_{2k}q_{2l}) \left\langle R_{1i}R_{1j}R_{2k}R_{2l}\right\rangle_C \\
& + \frac{1}{6}(q_{1i}q_{1j}q_{1k}q_{2l} + q_{2i}q_{2j}q_{2k}q_{1l}) \left\langle R_{1i}R_{1j}R_{1k}R_{2l}\right\rangle_C,
\end{aligned} \tag{4.34}$$

where again the Einstein summing convention was used. To derive this equation, it was assumed that there is no net flow which gives $\langle R_{1i}R_{2j}\rangle = \langle R_{2i}R_{1j}\rangle$ and that diffusion is a stationary process, which leads to $\langle R_{1i}R_{1j}\rangle = \langle R_{2i}R_{2j}\rangle$ and similar results for the fourth order terms. The single cumulants can be used to define several tensors, which, given in the moments, are

$$Q_{ij} = -\left\langle R_{1i}R_{2j}\right\rangle \tag{4.35a}$$

$$K_{ijkl} = \left\langle R_{1i}R_{1j}R_{1k}R_{1l}\right\rangle - \left\langle R_{1i}R_{1j}\right\rangle \left\langle R_{1k}R_{1l}\right\rangle - \left\langle R_{1i}R_{1k}\right\rangle \left\langle R_{1j}R_{1l}\right\rangle - \left\langle R_{1i}R_{1l}\right\rangle \left\langle R_{1j}R_{1k}\right\rangle \tag{4.35b}$$

$$S_{ijkl} = -\left\langle R_{1i}R_{1j}R_{1k}R_{2l}\right\rangle + \left\langle R_{1i}R_{1j}\right\rangle \left\langle R_{1k}R_{2l}\right\rangle + \left\langle R_{1i}R_{1k}\right\rangle \left\langle R_{1j}R_{2l}\right\rangle + \left\langle R_{1j}R_{1k}\right\rangle \left\langle R_{1i}R_{2l}\right\rangle \tag{4.35c}$$

$$Z_{ijkl} = \left\langle R_{1i}R_{1j}R_{2k}R_{2l}\right\rangle - \left\langle R_{1i}R_{1j}\right\rangle \left\langle R_{2k}R_{2l}\right\rangle - \left\langle R_{1i}R_{2k}\right\rangle \left\langle R_{1j}R_{2l}\right\rangle - \left\langle R_{1i}R_{2l}\right\rangle \left\langle R_{1j}R_{2k}\right\rangle. \tag{4.35d}$$

$\underline{\underline{K}}$ is the kurtosis tensor, the generalization of the kurtosis (section 4.2.4), and clearly accessible from measurements with only a single diffusion encoding (SDE), as it only contains terms with R_1. Thus no closer analysis of it is presented here.

$\underline{\underline{Q}}$ is named correlation tensor [JB11]. The name stems from the fact that it is non-zero in the case that the displacements in both encodings are correlated. For long mixing times this correlation is lost and the correlation tensor vanishes. Thus, it is a good indicator if the long mixing time limit is reached. It can be derived from the time dependent diffusion tensor and carries no additional information on the microstructure compared to $\underline{\underline{D}}(t)$ [Jes12]. In actual measurements, it might nevertheless be more accurate to use $\underline{\underline{Q}}$ instead of determining the time dependent diffusion tensor.

The tensors $\underline{\underline{S}}$ and $\underline{\underline{Z}}$ contain information that cannot be gathered with SDE, as they contain positions of at least three time points in one moment. Here, the long t_m limit is assumed, which leads to $S_{ijkl} \to 0$. As can be seen in equation 4.35c, each term of S_{ijkl} contains only one displacement from the second encoding, which becomes independents of the three others and therefore vanishes. In this limit $\underline{\underline{Z}}$ becomes

$$Z_{ijkl} = \langle R_{1i} R_{1j} R_{2k} R_{2l} \rangle - \langle R_{1i} R_{1j} \rangle \langle R_{2k} R_{2l} \rangle , \tag{4.36}$$

which is zero in Gaussian systems.

4.3.2 Macroscopically Isotropic Systems

To derive a microscopically anisotropy measure, it is assumed that the single pores are randomly oriented so that there is no macroscopic anisotropy. In this case, $\underline{\underline{Z}}$ is also isotropic and because of the minor ($Z_{ijkl} = Z_{jikl} = Z_{ijlk}$) and major ($Z_{ijkl} = Z_{klij}$) symmetry (equation 4.35d), it is given by [Moa08, Jes12]

$$Z^{\text{iso}}_{ijkl} = Z^{\text{iso}}_{zzxx}\delta_{ij}\delta_{kl} + \frac{1}{2}(Z^{\text{iso}}_{zzzz} - Z^{\text{iso}}_{zzxx})(\delta_{ik}\delta_{jl} + \delta_{il}\delta_{jk}). \tag{4.37}$$

The superscript iso is used to indicate that this is derived in an macroscopically isotropic system. This was derived by using the fact that each isotropic rank four tensor with minor and major symmetry is fully determined by two parameters [Moa08]. The validity of the choice is simply proven by calculating the right hand side of equation 4.37 for $zzxx$ and $zzzz$. It leads to the signal:

$$\log S^{\text{iso}}(\boldsymbol{q_1}, \boldsymbol{q_2}) = -2q_1q_2\text{MD}\Delta + \frac{1}{12}(q_1q_2)^2 K^{\text{iso}}_{zzzz} + \frac{1}{4}(q_1q_2)^2(\cos^2\theta(Z^{\text{iso}}_{zzzz} - Z^{\text{iso}}_{zzxx}) + Z^{\text{iso}}_{zzxx}), \tag{4.38}$$

where MD was used for the isotropic diffusion coefficien.t Equation 4.38 was derived for a macroscopically isotropic system but no not for a special coordinate system.

In macroscopically isotropic systems, the signal does not depend on the actual direction of the $\boldsymbol{q}$-vectors, but only on the angle θ between them, and their amplitude, which are combined in the dot product $\boldsymbol{q_1} \cdot \boldsymbol{q_2} = q_1q_2\cos\theta$. The $\cos^2\theta$ dependence in equation 4.38

shows that the largest signal difference can be found between parallel and perpendicular diffusion encodings. It is given by the compartment eccentricity ϵ [JLSD13]:

$$\epsilon = \frac{Z^{\text{iso}}_{zzzz} - Z^{\text{iso}}_{zzxx}}{4}. \tag{4.39}$$

To show that ϵ depends on the pore anisotropy, the averaging over all random paths of particles in an individual pore is denoted by $\langle\cdot\rangle_p$ and the averaging over the pore ensemble by an overbar. This notation is used to disentangle the averaging processes. In a single pore, the displacements in each encoding become independent at long mixing times so that equation 4.36 becomes

$$Z^{\text{iso}}_{ijkl} = \overline{\langle R_{1i}R_{1j}R_{2k}R_{2l}\rangle_p}^{\text{iso}} - \overline{\langle R_{1i}R_{1j}\rangle_p}^{\text{iso}}\,\overline{\langle R_{2k}R_{2l}\rangle_p}^{\text{iso}} \tag{4.40a}$$

$$= \overline{\langle R_{1i}R_{1j}\rangle_p\langle R_{2k}R_{2l}\rangle_p}^{\text{iso}} - \overline{\langle R_{1i}R_{1j}\rangle_p}^{\text{iso}}\,\overline{\langle R_{2k}R_{2l}\rangle_p}^{\text{iso}} \tag{4.40b}$$

$$= \overline{\left(\langle R_{1i}R_{1j}\rangle_p - \overline{\langle R_{1i}R_{1j}\rangle_p}^{\text{iso}}\right)\left(\langle R_{1k}R_{1l}\rangle_p - \overline{\langle R_{1k}R_{1l}\rangle_p}^{\text{iso}}\right)}^{\text{iso}} \tag{4.40c}$$

In the last line, it was used that the diffusion is a stationary process. The subscripts 1 and 2 can be dropped from here on out. Equation 4.40c is identical for isotropic and anisotropic macroscopic ordering, except for the superscript. The term $\langle R_iR_j\rangle_p$ is proportional to the diffusion tensor of a single pore D^p_{ij} and so $\underline{\underline{Z}}$ depends on the single pore anisotropy.

In the long diffusion time limit, the initial and final position of the particles become uncorrelated and the displacement can be replaced by the positions using $\langle R_iR_j\rangle_p \to 2\langle r_ir_j\rangle_p$:

$$Z^{\text{iso}}_{ijkl} = 4\overline{\left(\langle r_ir_j\rangle_p - \overline{\langle r_ir_j\rangle_p}^{\text{iso}}\right)\left(\langle r_kr_l\rangle_p - \overline{\langle r_kr_l\rangle_p}^{\text{iso}}\right)}^{\text{iso}} \tag{4.41}$$

This shows that Z_{ijkl} is given by the variation of the radius of the gyration tensor of the single pore $\langle r_ir_j\rangle_p$. For isotropic pore shapes the gyration tensor is given by $\langle r_ir_j\rangle = r^2\delta_{ij}$, which would lead to a vanishing $Z^{\text{iso}}_{zzzz} - Z^{\text{iso}}_{zzxx}$. This shows that ϵ depends on the pore anisotropy and the pore size. For a pure anisotropy measure a normalization is needed, which can be achieved for example by MD.

4.3.3 Macroscopically Anisotropic Systems

In the presence of a macroscopic anisotropy, equation 4.38 does not hold anymore because the signal depends additionally on the actual direction of the diffusion encodings. This problem can be solved by acquiring many diffusion directions and averaging the signal before taking the logarithm. This so called powder average has the same effect as taking the sample and making a powder out of it, leading to a macroscopic anisotropy.

For a truly isotropic signal, an infinite amount of directions would be needed, but it was shown that 60 measurements with perpendicular $\boldsymbol{q}$-vectors and 12 measurements with parallel $\boldsymbol{q}$-vectors are accurate up to the fifth order [GP09, JLSD13]. This scheme applies 12 directions for the first encoding to accurately sample a sphere in q-space and 5 directions for

the second encoding to sample the circle perpendicular to the first encoding. Therefore only 12 measurements are needed, for the parallel encodings. The signal can then be calculated by the average for each of the two sets of measurements (parallel and perpendicular).

This isotropic signal can be written for $q = q_1 = q_2$ as

$$\log S^{\text{iso}}(q_1, q_2) = -2q^2 D^{\text{iso}}\Delta + \frac{1}{12}q^4 K^{\text{iso}}_{zzzz} + \frac{1}{4}q^4(\cos^2\theta(Z^{\text{iso}}_{zzzz} - Z^{\text{iso}}_{zzxx}) + Z^{\text{iso}}_{zzxx}). \quad (4.42)$$

An important point is that $\underline{\underline{Z}}^{\text{iso}}$ is defined over $\log S^{\text{iso}}$ and not by averaging $\underline{\underline{Z}}$ directly. $\underline{\underline{Z}}^{\text{iso}}$ can be calculated from the anisotropic $\underline{\underline{Z}}$ due to the fact that it can be written as $a\delta_{ij}\delta_{kl} + b(\delta_{ik}\delta_{jl} + \delta_{il}\delta_{jk})$ and that the inner product ($\langle\cdot,\cdot\rangle$) is rotationally invariant. So a and b can be determined by using

$$\langle \underline{\underline{Z}}^{\text{iso}}, \delta_{ij}\delta_{kl}\rangle = \langle \underline{\underline{Z}}, \delta_{ij}\delta_{kl}\rangle \quad (4.43a)$$

$$\langle \underline{\underline{Z}}^{\text{iso}}, \delta_{ik}\delta_{jl} + \delta_{il}\delta_{jk}\rangle = \langle \underline{\underline{Z}}, \delta_{ik}\delta_{jl} + \delta_{il}\delta_{jk}\rangle, \quad (4.43b)$$

leading to

$$\begin{aligned} Z^{\text{iso}}_{ijkl} = {} & \frac{1}{5}\left(2\langle R_{1i}R_{1i}R_{1j}R_{1j}\rangle - \langle R_{1i}R_{1j}R_{2i}R_{2j}\rangle - \frac{5}{9}\langle R_{1i}R_{1i}\rangle\langle R_{2j}R_{2j}\rangle\right)\delta_{ij}\delta kl \\ & + \frac{1}{30}\left(3\langle R_{1i}R_{1j}R_{2i}R_{2j}\rangle - \langle R_{1i}R_{1i}R_{2j}R_{2j}\rangle\right)(\delta_{ik}\delta_{jl} + \delta_{il}\delta_{jk}) \end{aligned} \quad (4.44)$$

The result can be used to determine the eccentricity to:

$$\epsilon = \frac{1}{60}\left(3\overline{\langle R_iR_j\rangle\langle R_iR_j\rangle} - \overline{\langle R_iR_i\rangle\langle R_jR_j\rangle}\right) \quad (4.45)$$

$$= \frac{\Delta^2}{15}(3D^p_{ij}D^p_{ij} - D^p_{ii}D^p_{jj}) \quad (4.46)$$

$$= \frac{3\Delta^2}{5}\text{var}(\lambda^p_i), \quad (4.47)$$

which again shows the dependence on the pore diffusion tensor. In the last line, the eigenvalues λ^p_i of $\underline{\underline{D}}^p$ were introduced together with their variance. The connection of ϵ to $\text{var}(\lambda^p_i)$ suggests a similar normalization as for the FA (equation 4.27), resulting in the microscopic fractional anisotropy (μFA) [JLSD13, JLSD14b]:

$$\mu\text{FA}^2 = \frac{3}{2}\frac{\epsilon}{\epsilon + (3\Delta^2/5)(\text{MD}^2)}, \quad (4.48)$$

where $\overline{(\lambda^p_i)^2} = \text{var}(\lambda^p_i) + \overline{\lambda^p_i}^2$, which can be derived from the second order cumulant, and $\overline{\lambda^p_i} = \text{MD}$ were used.

The μFA gives the same value as the FA for parallel pores but is not reduced if the macroscopic order is lost while preserving the microsopic pore anisotropy.

4.4 Gradient Moment Nulling and Flow

Thus far, all derivations for MRI assumed no net motion of particles. For in vivo measurements, this is not always the case, as there is, for example, blood flow or pulsation. Since diffusion measurements are very sensitive to motion, these effects can have a considerable influence on the resulting parameters.

To see how bulk motion can compensated for, the Taylor expansion of the particle trajectory is used. The derivation is done for one dimension, but it can easily be expanded to three dimensions as they are independent:

$$x(t) = x_0 + v_0 t + \frac{1}{2} a_0 t^2 + \dots, \tag{4.49}$$

with the initial position x_0, the initial velocity v_0 and the initial acceleration a_0. For the accumulated phase, this gives

$$\Phi(t) = \gamma \int_0^t G(t') x(t') \mathrm{d}t' = \gamma \int_0^t G(t')(x_0 + v_0 t' + \frac{1}{2} a_0 t'^2 + \dots)\mathrm{d}t, \tag{4.50}$$

which can be used to define the n-th gradient moment $m_n(t)$:

$$m_n(t) = \int_0^t G(t') t'^n \mathrm{d}t'. \tag{4.51}$$

This definition leads to the phase:

$$\Phi(t) = \gamma m_0(t) x_0 + \gamma m_1(t) v_0 + \frac{\gamma}{2} m_2(t) a_0 + \dots \tag{4.52}$$

Equation 4.52 shows that in order to negate the effect of motion of order n, the nth gradient moment needs to be zero. The process of designing gradient profiles with moments set to zero is called gradient moment nulling. Diffusion encodings are designed to null the zeroth gradient moment, therefore they have no effect on resting particles. A nulled zeroth moment is also called gradient reversal. A nulled first moment leads to a refocusing of particles with constant velocity and is known as flow compensation.

To achieve gradient reversal (and perform a diffusion encoding), at least two gradient pulses with opposite effective polarity are needed. For each higher moment that should be nulled additionally, an extra gradient pulse with changing polarity is needed. This leads to a lower b-value or a longer TE. Therefore, only few applications null higher orders than the first one.

Here, as a little example, the first moment caused by a trapezoidal gradient pulse starting at t_0 (equation 3.3) is calculated:

$$m_1(t_0+T_G) = \int_{t_0}^{T_G} G(t)t\mathrm{d}t \tag{4.53a}$$

$$= \int_{t_0}^{t_0+p} \left(\frac{g}{p}(t-t_0)\right) t\mathrm{d}t + \int_{t_0+r}^{t_0+\delta} gt\mathrm{d}t + \int_{t_0+\delta}^{t_0+\delta+p} g\left(1-\frac{1}{p}(t-t_0-\delta)\right) t\mathrm{d}t \tag{4.53b}$$

$$= \left(\frac{r^2}{3} + \frac{1}{2}pt_0 + \frac{(\delta-p)^2}{2} + (\delta-p)(t_0+p) + \frac{p^2}{6} + \frac{1}{2}p(t_0+\delta)\right) g \tag{4.53c}$$

$$= \delta g\left(\frac{1}{2}(p+\delta)+t_0\right). \tag{4.53d}$$

This solution shows that the value of m_1 depends on the definition of $t=0$, therefore it is useful to examine what happens in the case of a time translation. Let the gradient pulse $\tilde{G}(t)$ be the time translated scheme $G_0(t)$, which starts at $t=0$, that is $\tilde{G}(t) = G_0(t-\Delta t)$. The first moment is given by

$$\tilde{m}_1 = \int_{\Delta t}^{\Delta t+T_G} \tilde{G}(t)t\mathrm{d}t \tag{4.54a}$$

$$= \int_{\Delta t}^{\Delta t+T_G} G_0(t-\Delta t)t\mathrm{d}t \tag{4.54b}$$

$$= \int_{0}^{T_G} G_0(w)(w+\Delta t)\mathrm{d}w \tag{4.54c}$$

$$= \int_{0}^{T_G} G_0(w)w\mathrm{d}w + \int_{0}^{T_G} G_0(w)\Delta t\mathrm{d}w \tag{4.54d}$$

$$= m_1 + m_0\Delta t. \tag{4.54e}$$

The solution demonstrates that for a gradient scheme with $m_0 = 0$, the first moment is time invariant and does not depend on the choice of $t=0$.

4.5 Intravoxel Incoherent Motion

The influence of blood flow in small vessels on the diffusion signal can be modeled by the intravoxel incoherent motion model [LBL+86, LBL+88]. It assumes a randomly oriented capillary bed in which blood flows with a constant velocity. After a characteristic time τ_B, the blood changes the direction. It is further assumed that the velocities before and after the direction change are uncorrelated.

For long diffusion times T_D, this model leads to a biexponential diffusion weighted signal:

$$S(b) = S(0)\left(f\mathrm{e}^{-bD^\star} + (1-f)\mathrm{e}^{-bD}\right). \tag{4.55}$$

The factor f is known as the perfusion fraction. It is the fraction of the signal attenuation that can be attributed to the perfusion of the tissue. In the case of long T_D compared to τ_B, the blood flow changes the direction so often that it can be considered as a diffusion-like motion with a pseudo-diffusion coefficient $D^\star$, which is larger than the actual diffusion coefficient D.

LeBihan stated that $\frac{T_D}{\tau_B} \gtrsim 7$ would be needed for the long diffusion time limit to be valid [LBL+88]. In this limit the use of a flow-compensated sequence should not change the signal attenuation, as the flow changes directions often during the experiment. It was shown that this limit, although often applied, does not hold for typically used diffusion times, as a difference between flow-compensated and uncompensated diffusion encodings was observed [WSL15].

5 Materials and Methods

In the course of this work, two different kinds of sequences were implemented that both aimed at reducing artifacts in special applications of DWI. One sequence was a DDE sequence, which was compensated for eddy currents, the other one was a SDE sequence, which could be compensated for any combination of flow, concomitant fields and eddy currents. In this chapter the models used to compensate for the artifacts are recapped (section 5.1). The DDE sequence used an analytical solution for the eddy currents, while the SDE sequence was optimized numerically (section 5.2). Details on the sequence implementations used for the actual measurements are described in section 5.3. The rest of the chapter details other experimental parameters as well as the soft- and hardware used.

5.1 Artifact Models

The compensation of different artifacts requires a description of the source of the artifacts and its strength. Different models can be used for this. In this section the models used here are specified. For all measurements the assumption of rectangular, which means negligible ramp times, gradient pulses with constant gradient amplitudes g that might only differ in sign. The index i refers always to the i-th gradient. The duration of a gradient is denoted with δ_i, its starting time with t_i and the time between gradients with T_i. Thus, the starting time of the $(i+1)$th gradient is given by $t_{i+1} = t_i + \delta_i + T_i$.

5.1.1 Eddy Currents

Eddy currents are induced by changing gradient amplitudes $G(t)$. It was assumed that these eddy currents decay exponentially with only one time constant τ. The resulting eddy current of a single gradient with starting time t_i can then be calculated from equation 3.19 by using L'Hôpital's rule to find the limit for the ramp time going to zero:

$$I(T) \propto g\mathrm{e}^{-T/\tau}\left(\mathrm{e}^{\delta_i/\tau} - 1\right)\mathrm{e}^{t_i/\tau}, \tag{5.1}$$

where $T > t_i + \delta_i$.

For a series of gradients, the eddy currents for each gradient must be summed up so that the condition for eddy current compensation becomes:

$$\sum_i s_i\,\mathrm{e}^{-T/\tau}\left(\mathrm{e}^{\delta_i/\tau} - 1\right)\mathrm{e}^{t_i/\tau} = 0, \tag{5.2}$$

where s_i is the sign of the gradient. The gradient amplitude could be dropped in equation 5.2 as it is a constant over the whole gradient train. Additionally, it was assumed that there are no cross effects between the different spatial directions so that the timing could be optimized without paying attention to the actual gradient direction.

5.1.2 Concomitant Fields

As shown in section 3.5, truly linear magnetic gradient fields are not achievable and there are always higher order field gradients present. These can lead to an incomplete refocusing of the magnetic resonance (MR) signal. To compensate for this, the accumulated phase (equation 3.29) has to be zero, which leads in the second order term to

$$\int_0^T s(t)'' \, G(t)^2 \mathrm{d}t = 0. \tag{5.3}$$

In the case considered here (rectangular gradients), this simplifies to:

$$\sum_i s_i'' \delta_i = 0, \tag{5.4}$$

where $s(t)''$ and s_i'' were used for considering the number of refocusing pulses before the gradients:

$$s(t)'' \text{ or } s_i'' = \begin{cases} +1 & \text{if number of preceding RF pulses is even or 0} \\ -1 & \text{if number of preceding RF pulses is odd} \end{cases} \tag{5.5}$$

Higher order terms were not considered in this work. Since the acquired phase is quadratic in the gradient amplitude, at least one refocusing pulse is needed to compensate for concomitant fields. Since the applied gradient amplitude is constant, its value is not needed for nulling the acquired phase.

5.1.3 Flow

For the Stejskal-Tanner sequence, the diffusion encoded signal drops faster in the presence of flow than in the absence thereof. This can be compensated by the technique of gradient moment nulling, as described in section 4.4. In the case of constant flow velocities, the first gradient moment m_1 has to be nulled for flow compensation:

$$m_1(T) = \int_0^T s(t)' \, G(t) \, t \, \mathrm{d}t = 0, \tag{5.6}$$

with $s(t)'$ taking care of the refocusing RF pulses, which means it switches sign for each RF pulse and has an absolute value of 1. For rectangular gradients with constant amplitude this can be simplified:

$$\sum_i s_i' \, (\frac{\delta_i^2}{2} + \delta_i \, t_i) = 0. \tag{5.7}$$

s_i' is the discrete version of $s(t)'$. Since g is constant in this implementation, it does not need to be considered for flow compensation. To achieve flow compensation while the gradient reversal condition is fulfilled, at least three gradient pulses with switching effective signs are needed [BKZ04].

5.2 Optimization Setup

For the optimization of the SDE sequence, rectangular gradients were assumed. The maximal number of gradient pulses and the number of refocusing RF pulses were predefined. To distinguish the different sequences, a short hand notation is used. Each gradient is denoted with either $+$ or $-$, depending on its direction and a RF pulse is indicated by $|$. So, for example, the sequence in figure 5.1a would be $+-|-+$. To compare the ability to

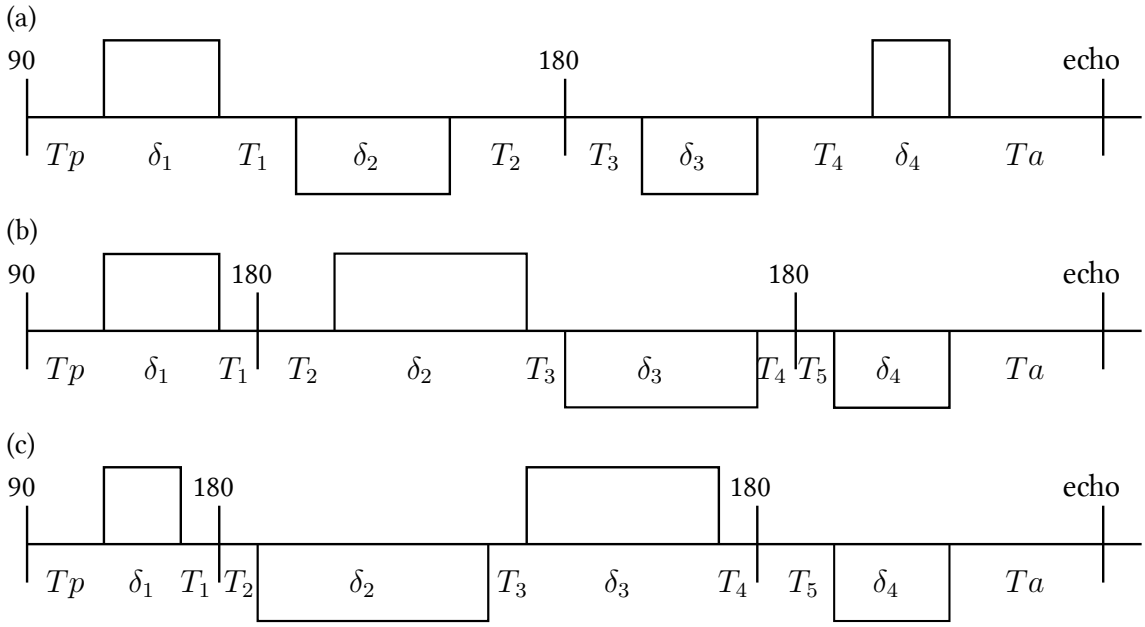

Figure 5.1: Example sequences considered in numerical optimization. In the shorthand notation the sequences are $+-|-+$ (a), $+|+-|-$ (b) and $+|-+|-$ (c). Additionally, the names of the timing parameters are shown. Each time between gradients with a RF pulse is described by two timing parameters, one before and one after the RF pulse. Tp is the time needed for the excitation and Ta the time needed for the readout train before the formation of the spin echo.

produce a high diffusion encoding while compensating for different kinds of artifacts, sequences with a maximal number of gradient pulses of 2-5 were considered. The number of RF pulses was 1 or 2. The number of sequences was reduced by a few limitations. First, neighboring gradients had to differ in their sign if no RF pulse was in between them. So for example $+|+-|-$ (figure 5.1b) was considered, while $+|--|+$ was not. Second, sequences that only differ in an overall sign change (for example, $+|+-|-$ and $-|-+|+$) were considered identical. With these restrictions 60 sequences remained.

To further decrease the number, only sequences that allowed for simultaneous gradient reversal and concomitant field compensation (equation 5.4) were taken into account. With the notation in section 5.1, the condition for gradient reversal can be written generally as

$$\sum_i s_i' \delta_i = 0. \tag{5.8}$$

The possibility to fulfill both conditions is easily checked for a sequence. For example, for the standard Stejsakl-Tanner sequence $(+|+)$ the gradient reversal gives the condition $-\delta_1 + \delta_2 = 0$, which is the same (except for an overall $-$ sign) for concomitant field compensation so that this sequence is intrinsically compensated for concomitant fields.

For the sequence $+|-+|-$ (figure 5.1c), the gradient reversal $\delta_1 + \delta_2 - \delta_3 - \delta_4 = 0$ and the concomitant field compensation $\delta_1 - \delta_2 - \delta_3 + \delta_4 = 0$ can be fulfilled at the same time for $\delta_1 = \delta_3$ and $\delta_2 = \delta_4$.

The sequence $+-|-$ has to fulfill the conditions for gradient reversal $-\delta_1 + \delta_2 - \delta_3 = 0$ and for concomitant field compensation $\delta_1 + \delta_2 - \delta_3 = 0$. These two conditions lead to $\delta_1 = 0$. This means the sequence would reduce to $-|-$, which is considered identical to $+|+$. Therefore, such sequences were not included in the optimization.

The actual optimization was set up to maximize the b-value by varying the gradient durations and the time between gradients (T_i). The total duration of the diffusion encoding ($\sum_i \delta_i + T_i$) had to stay within TE $- Tp - Ta$, where Tp was the time for the excitation and Ta the time for the readout until the echo formation. To ensure the right timing of the RF pulses, the time slot in which they appeared was split in two independent parameters (see figure 5.1 for examples), one before and one after the RF pulse. Gradient reversal was ensured by fixing the first gradient durations δ_1 according to equation 5.8.

In the cases with two refocusing RF pulses, these had to be separated by TE/2. This allowed for fixing another timing parameter, which was chosen to be T_3. Additionally, the exact position of the RF pulses does not change TE as long as their distance remains the same. This fact was used to set the total diffusion time T_D to the maximum value and use it to fix δ_2. For the sequences with only one refocusing pulse, T_3 and δ_2 could not be fixed and timing constraints were used to ensure that the RF pulse is played out at the right time.

The optimization was then performed with different sets of conditions, which could include flow (equation 5.7), concomitant field (equation 5.4) and eddy current (equation 5.2) compensation. This led to eight different optimization conditions for 20 sequences:

1. no additional conditions
2. flow compensation
3. concomitant field compensation
4. eddy current compensation
5. flow+concomitant field compensation
6. flow+eddy current compensation
7. concomitant field+eddy current compensation
8. flow+concomitant field+eddy current compensation

During the optimization procedure, a gradient duration of 0 was allowed. The time for a refocusing RF pulses was set to 5 ms, $Tp = 5$ ms and $Ta = 10$ ms were chosen. The eddy

current decay time was determined in phantom measurements (section 6.1.2), resulting in $\tau = 70\,\text{ms}$.

The optimization was set up in Matlab's Global Optimization Toolbox (Version 2016a, The Mathworks Inc., Natick, MA) using the global search algorithm [ULP+07]. This algorithm uses multiple start points and and a local optimizer to find a global optimum. The start points are created with a scatter search algorithm [Glo98], which is initialized with valid (for no additional conditions) gradient times. As local optimizer *fmincon* with the interior point algorithm was used, which is a gradient based optimization algorithm [BHN99, BGN00, WMNO06].

5.3 Sequence Design

5.3.1 Sequence Programming

The different diffusion sequences were implemented with the IDEA environment, provided by Siemens. The used versions were D13D for the DDE sequence and E11C for the SDE sequence. The IDEA environment is based on C++ and allows the implementation of in-house developed sequences.

5.3.2 Twice-Refocused Spin Echo

A common way to compensate eddy current distortions in DWI is the use of the twice-refocused spin echo (TRSE) [RHWW03, Hei00]. This sequence employs two refocusing RF pulses and four gradient pulses. In the short hand notation, this is $+|-+|-$ and can be seen in figure 5.1c. Normally, the T_i are chosen as small as possible, which means in this case $T_3 = 0$ and $T_1 + T_2 = T_4 + T_5 = u$, where u is the time needed for the slice selection. With the conditions of gradient reversal

$$\delta_1 + \delta_2 = \delta_3 + \delta_4, \tag{5.9}$$

the TE constraint

$$\frac{\text{TE}}{2} = \delta_2 + \delta_3 + u, \tag{5.10}$$

and the limit for T_D

$$T_D = \delta_1 + \delta_2 + \delta_3 + \delta_4 + 2u, \tag{5.11}$$

there exists an analytical solution for the eddy current equation 3.19:

$$\delta_1 = \tau \log\left(\frac{(1+\exp(T_D/2\tau))}{(1+\exp(u/\tau))\,(1+\exp(\mathrm{TE}/2\tau))}\right), \tag{5.12a}$$

$$\delta_2 = \frac{T_D}{2} - \delta_1 - u, \tag{5.12b}$$

$$\delta_3 = \frac{\mathrm{TE} - T_D}{2} + \delta_1, \tag{5.12c}$$

$$\delta_4 = T_D - \frac{\mathrm{TE}}{2} - \delta_1 - u. \tag{5.12d}$$

5.3.3 Eddy-Current-Compensated Double Diffusion Encoding

For the DDE sequence, all combinations of eddy-current-compensated (c) and uncompensated (u) diffusion encodings were implemented. The corresponding sequence schemes are shown in figure 5.2. A short hand notation is used to distinguish the different combinations, where the choice for the first and second encoding are noted with one letter each, separated by a /. For example, the sequence with the first encoding compensated and the second uncompensated is noted as c/u (figure 5.2c). The total diffusion time of each encoding i (T_{Di}) and the mixing time t_m, which is defined as the time between the end of the first and the beginning of the second encoding, could be chosen as sequence parameters. For each compensated diffusion encoding, the gradient durations were calculated following equations 5.12(a)-(d). The value for TE had to be replaced by an effective echo time TE_eff for each compensated diffusion encoding. TE_eff is defined as twice the distance between the RF pulses of that encoding. With that replacement the equations 5.12 can be used directly. In the case of the u/c and c/u sequences, TE_eff could be chosen as an additional sequence parameter. For the sequence c/c, the TE_eff for each encoding have to add up to the actual TE and they were chosen equally, leading to identical gradient durations for both encodings. For the uncompensated sequences, the gradients were placed symmetrically around the RF pulse and had the maximal duration. With the definition of T_{D1}, T_{D2} and t_m, the actual TE is fixed for the u/u sequence in this implementation.

5.3.4 Single Diffusion Encoding with Possible Artifact Reduction

The sequence that was used for the measurements consisted of a maximum of five gradient pulses and one refocusing RF pulse ($+-+|-+$, see also figure 5.3). For different compensations, the number of gradients can change, as the gradient durations could become zero.

5.3.5 Crusher Gradients

Since the refocusing RF pulses are not perfect, additional gradient pulses are needed to dephase any signal newly created by these pulses. One way is to add a gradient pair directly

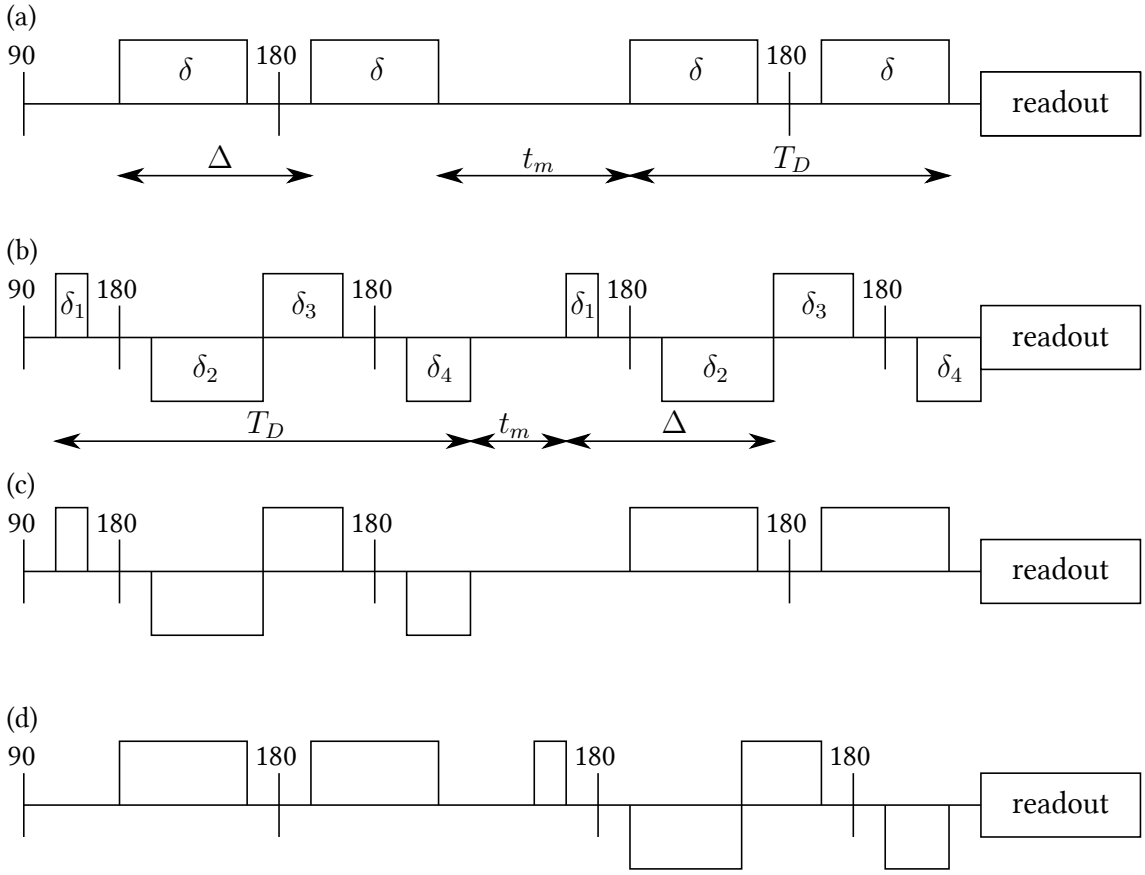

Figure 5.2: DDE sequence schemes. Here, the sequence schemes for all combinations of compensated and uncompensated diffusion encodings are shown. For the u/u (a) and c/c (b) sequence, the definitions of Δ, T_D and t_m are shown. These are skipped for the c/u (c) and u/c (d) sequences.

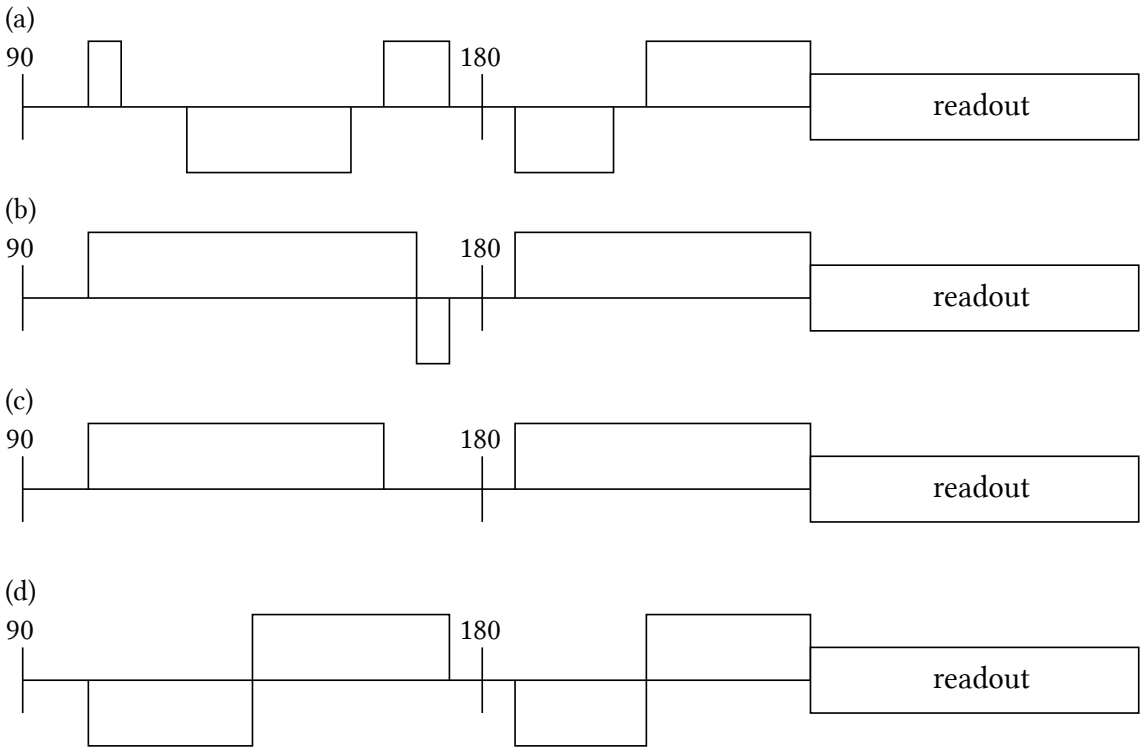

Figure 5.3: Sequence schemes used for compensating different artifacts. (a): Scheme for compensating flow and eddy currents simultaneously. This can be run with or without concomitant field compensation. (b): Sequence without any compensation. (c): compensated only for concomitant fields. This is the samescheme as for the Stejskal-Tanner sequence. (d): Sequence scheme for only flow or only eddy current compensation. For additional concomitant field compensation, the insertion of delay times between the gradients might be necessary, depending on the actual timing.

around the RF pulse [BW84], where both gradients have the same zeroth moment. The second gradient dephases the magnetization that is unintentionally excited by the RF pulse. For the intended signal pathway, the gradient pair generates a small additional diffusion encoding. The gradient moment was chosen to ensure a phase difference of at least 8π over a single voxel.

The effect of the crusher gradients on the actual diffusion encoding is minimized by choosing the directions orthogonal to each other [NTW14]. In the case of an eddy-current-compensated encoding in the DDE sequence, meaning two refocusing RF pulses, the corresponding crusher gradients were also orthogonal to each other. If crusher gradients between the first and second encoding were parallel, the ones belonging to the second encoding were rotated by 45°. In the case of SDE with artifact reduction, there was only one gradient pair, which was chosen orthogonal to the diffusion encoding.

5.4 Directionally Independent μFA Measurements

For a measurement of the μFA that is independent of the macroscopic orientation of the diffusion compartments, the directional scheme proposed by Jespersen et al. [GP09, JLSD13, JLSD14b] was used. This is comprised of 72 individual DDE measurements, 12 with parallel and 60 with orthogonal diffusion encodings. In the case of identical q-values in both encodings, this allows for a simple calculation of the μFA:

$$\mu\mathrm{FA} = \sqrt{\frac{3}{2}\frac{\epsilon}{\epsilon + (3/5)\Delta^2\,\mathrm{MD}^2}} \tag{5.13}$$

$$\epsilon = \frac{1}{q^4}\left(\log\left(\frac{1}{12}\sum S_{\parallel}\right) - \log\left(\frac{1}{60}\sum S_{\perp}\right)\right), \tag{5.14}$$

where Δ describes the classical diffusion time, defined by the time from the start of the first dephasing to the beginning of the first rephasing gradient. $\sum S_{\parallel}/\sum S_{\perp}$ is the sum over all measurements with parallel/perpendicular diffusion encodings. The MD is determined by fitting

$$\log\frac{S(\boldsymbol{q}_1,\boldsymbol{q}_2)}{S(0,0)} = -\frac{1}{2}\boldsymbol{q}_1^T\underline{\underline{D}}\boldsymbol{q}_1 - \frac{1}{2}\boldsymbol{q}_2^T\underline{\underline{D}}\boldsymbol{q}_2 + \boldsymbol{q}_1^T\underline{\underline{Q}}\boldsymbol{q}_2 \tag{5.15}$$

to the same 72 measurements and an additional measurement with $\boldsymbol{q}_1 = \boldsymbol{q}_2 = 0$. The MD is defined as $\frac{1}{3}\mathrm{tr}(\underline{\underline{D}})$. The correlation tensor $\underline{\underline{Q}}$ was included in the fit as t_m was not long enough for both encodings to be completely independent, as was experimentally verified in this work (section 6.3).

5.5 Monte Carlo Simulations

Monte Carlo simulations were set up to further test the dependence of the DDE parameters on the timing. Therefore, two dimensional random walks for 500 000 particles were

simulated and the position of each particle was saved for every millisecond ($\boldsymbol{r_i}$). The total simulated diffusion time was 100 ms. This approach allows to evaluate several timings and diffusion encoding directions with just one Monte Carlo dataset. The diffusion coefficient was set to $D = 2\,\mu\text{m}^2/\text{ms}$, with a time for one random step of $\Delta t = 1.7\,\mu\text{s}$.

Diffusion in two different geometries was simulated. One, with an anisotropy, was diffusion between two parallel plates in a distance of 10 μm. The other one, without anisotropy, was diffusion inside a circle with a radius of 10 μm.

From the random walks, the normalized DDE signal was calculated for optimal conditions, meaning infinitely short gradients and no relaxation, for different T_D and t_m:

$$S = \left|\left\langle \mathrm{e}^{(-i(\boldsymbol{q_1}(\boldsymbol{r}(t_2)-\boldsymbol{r}(t_1))+\boldsymbol{q_2}(\boldsymbol{r}(t_4)-\boldsymbol{r}(t_3)))}\right\rangle\right|. \tag{5.16}$$

Here, T_D is defined as $t_2 - t_1 = t_4 - t_3$ and $t_m = t_3 - t_2$, $\boldsymbol{q_1}$ and $\boldsymbol{q_2}$ were the diffusion encoding strengths and directions for the first and second encoding. The $\langle\cdot\rangle$ indicates the average and $|\cdot|$ the absolute value. In total twenty directions were calculated. The first direction was perpendicular to the plates and was then rotated in five steps in the plane, with each step rotating $\boldsymbol{q_1}$ by 72°. For each first direction, four second directions were simulated: parallel, antiparallel and the two orthogonal directions. These signals were used to fit a two dimensional diffusion and correlation tensor according to equation 5.15. Additionally, the difference between the mean signal of the parallel and antiparallel directions and the mean of the signals of the perpendicular directions was used to determine μFA^2 with adjusted equations 5.13 and 5.14.

5.6 IVIM Model

For fitting the intravoxel incoherent motion (IVIM) model to the in vivo measurements the equation [LBL+86]

$$\frac{S(b)}{S(0)} = (1-f)\mathrm{e}^{-bD} + f\,\mathrm{e}^{-bD^\star} \tag{5.17}$$

was used. The diffusion weighted images were normalized by the image with $b = 0$ and the perfusion fraction f, the diffusion coefficient D and the pseudo-diffusion coefficient $D^\star$ were used as fitting parameters. The fitting was performed in Matlab with the provided trust region algorithm. Each of the three parameters was forced to be larger or equal to zero.

5.7 Phantoms

The verification of the sequences was done by measuring different kinds of phantoms. Their design and how they are used for their respective purpose is described in this section.

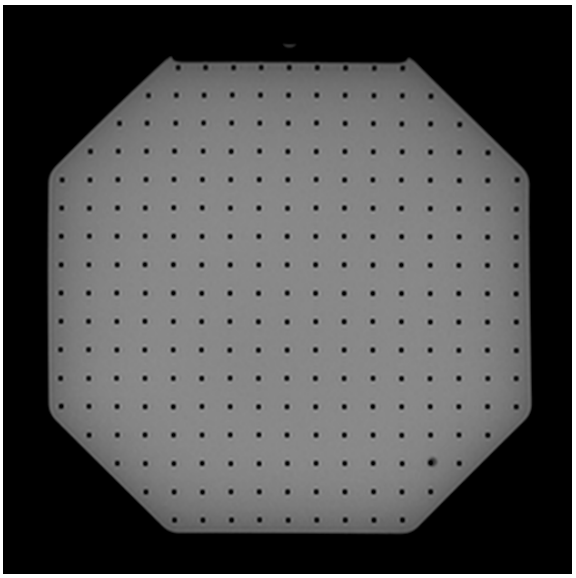

Figure 5.4: MR image of the grid phantom. The image was taken with a fast gradient echo sequence. The plastic rods can be seen as small dark squares.

5.7.1 Grid Phantom

To evaluate the image distortions due to eddy currents, a phantom was used that consists of plastic rods on a regular quadradtic grid. This grid is immersed in water. The outer shape is octagonal with a height and width of 330 mm. The distance of the rods is 20 mm. The setup can be seen in a MR image in figure 5.4. The plastic rods lead to signal voids in the image.

In the presence of different image distortions, as, for example, caused by eddy currents, the grid points fall on different pixels in the image. This leads to higher signal variations in such pixels. To quantify this, the coefficient of variation (CV) was used, which is defined as the variance normalized by the mean value. A higher CV can then be attributed to larger artifacts due to eddy currents. The measurements for determining the efficiency of the eddy current compensation, thus, consisted of several diffusion measurements with different directions, from which the CV of the signal was calculated. For an additional quantification, regions of interest (ROIs) were drawn and the mean value inside was determined.

5.7.2 String Phantom

To test the dependence of the μFA on different experimental parameters, a diffusion tensor phantom was used. This phantom is made of polyamide fibers, that were wound on a spindle [LHS09]. The fibers were wet while they were wound so that water diffuses between them. This phantom was placed in agarose gel. It shows an area with high diffusion anisotropy, on a microscopic and a macroscopic scale, in the fiber area and with no anisotropy in the agarose gel.

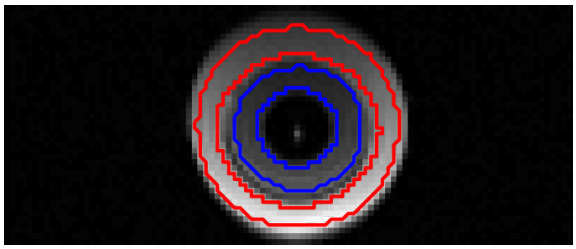

Figure 5.5: MR image of the string phantom. The blue ROI marks the fibers, the red one marks the agarose gel.

5.7.3 Flow Phantom

To verify the flow compensation, a tube with water flowing through it was used. The experimental setup is shown in figure 5.6. In the upper part, the tube can be seen. Additionally, a water bottle was used for the coil filling.

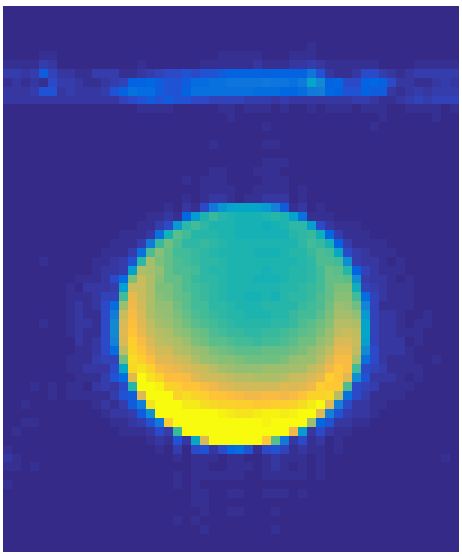

Figure 5.6: Experimental setup for the measurements with flow. Water was flowing through the tube in the upper part of the image. The flow direction was in-plane horizontally. The water bottle was used for filling the coil.

The flow was generated using a peristaltic pump (Watson Marlow 505Du, Watson Marlow Fluid Technology Group, Wilmington, MA, USA), with low rotational speed (10 and 20 rotations per minute), so the flow had a pulsatile part and was not completely constant. For the determination of the mean flow velocity v_{flow}, the time t was measured, during which a volume V passed through the system. Together with the tube diameter of $d = (1.31 \pm 0.02)$ cm, this gives:

$$v_{\text{flow}} = \frac{V/t}{\pi(d/2)^2}. \tag{5.18}$$

The used velocities were $v_{\text{flow},1} = (0.85 \pm 0.08)\,\text{cm/s}$ and $v_{\text{flow},2} = (1.71 \pm 0.11)\,\text{cm/s}$.

5.8 In Vivo Measurements

5.8.1 Prostate Anatomy and Prostate Cancer

This section gives a short introduction to the anatomy of the prostate and to prostate cancer, following the books [DW14, SSS09]. The prostate is comprised of glandular and muscular tissue. It can be divided into different zones. The urethra is passing through the prostate and is surrounded by the narrow periutheral zone. In front of the urethra lies the anterior zone, which does not include glandular tissue. The central zone surrounds the ejaculatory ducts. Between the latter two zones is the transitional zone. The largest amount of glandular tissue is located in the peripheral zone. In this work, all zones, except for the peripheral zone, were considered one area called the central gland.

The prostate carcinoma is the most common cancer in human males. It most often originates in the peripheral zone. The screening for prostate cancer can be done by a digital, rectal examination, the determination of the prostate-specific antigen (PSA) and/or a MRI examination, including DWI. The findings are confirmed by a biopsy which is also used for grading. The grading is done by the Gleason grading system [EAJAE05]. The Gleason grade is determined by the cell structure and can take values from 1 to 5, where 1 is given for well differentiated and 5 for very poorly differentiated cells. The differentiation of cells describes how specialized they are. For tumors, it means how similar the tumor cells are to the cells they originated from. Well differentiated cells resemble the original cells closely and indicate a less progressed tumor. The Gleason score is determined by the different Gleason grades found in a histological sample. The Gleason score is reported by two numbers, where the first one is the most common grade. The second number is the highest grade if that is higher than the first one, otherwise it is the second most common grade. If only one grade is found, it is doubled for the Gleason score.

Prostate cancer needs to be differentiated from benign prostatic hyperplasia (BPH), which is a benign hyperplasia originating mostly in the transitional zone.

5.8.2 Volunteers and Patients

For the in vivo verification of both sequences, healthy volunteers were measured. DDE images were acquired for six volunteers (3 female, 3 male) in the age of 21-36 years.

For the SDE experiments, three healthy volunteers were measured, the brain of a 22-year old female, the abdomen of a 24-year old female and the prostate of a 27-year old male volunteer. Additionally three male prostate cancer patients were imaged before biopsy (65, 66 and 69 years old). The biopsy confirmed the presence of prostate cancer with Gleason scores of $3+3$, $3+4$, and $3+5$.

5.9 MR-Scanner

All measurements were performed on a 3 T MRI machine (Prismafit, Siemens Healthcare, Erlangen). This Scanner allows nominal a maximal gradient amplitude of 80 mT/m and a

maximal slew rate of 200 T/m/s. These values had to be reduced to actually be able to run the sequence for all oblique slice orientations used and stay in the limits for peripheral nerve stimulation. The actually used maximal amplitude was 79 mT/m and the maximal slew rate was 100 T/m/s, which gives a maximal ramp time of $r = 0.79$ ms. This is shorter than the usual gradient duration of at least several milliseconds. For head measurements, a 64-channel head coil was used, while the abdomen and pelvis measurements were performed with a 18-channel flex coil and a spinal array (all provided by Siemens). For the phantom experiments with the grid phantom, the built-in body coil was used, while the diffusion phantom was measured in the 64-chanel head coil.

5.10 Evaluation Software

The determination of the different diffusion parameters, like the diffusion tensor, and the CV, for rating the strength of the eddy currents, was done with Matlab (Versions R2014a and R2016a, The Mathworks Inc., Natick, MA, USA). The evaluation was performed on the magnitude images from the MRI. The determination of the ADC and the diffusion tensor were done with the *mldivide* function of Matlab. If not mentioned explicitly, no filtering or interpolation was performed.

6 Results: Double Diffusion Encoding

In this chapter, the results for the μFA measurements are shown. The developed eddy-current-compensated DDE sequence was tested in phantoms as well as in vivo. The eddy current decay time, which is needed for a proper compensation, was determined in phantom experiments. Afterwards, the sequence was tested with phantoms to demonstrate the accurate determination of the μFA and the effectiveness of the eddy current compensation (section 6.1). Monte Carlo simulations were used to verify some of the results concerning the μFA (section 6.2). The final section describes the effects of the eddy current compensation on the determination of the μFA in vivo.

6.1 Phantom Experiments

6.1.1 Grid Phantom Measurements

To evaluate the degree of eddy current artifacts in the grid phantom, the DDE measurements were performed with 36 different direction combinations. This is the number of possible combinations if each diffusion encoding is in either plus or minus read, phase or slice direction, which coincided with the x, y and z-axis of the scanner.

The actual eddy current decay time of the used MRI machine was estimated by varying the assumed eddy current decay time τ with both encodings supposedly eddy current compensated. The images were taken with a FOV of $380\times380\,\mathrm{mm}^2$, a nominal resolution of $3.8\times3.8\,\mathrm{mm}^2$, a partial Fourier factor of $6/8$ and a slice thickness of 5 mm for ten slices. The timing parameters TE $=$ 96 ms, TR $=$ 3000 ms, $T_{D1} = T_{D2} =$ 38 ms and $t_m =$ 0 ms were chosen with a readout bandwidth of $2780\,\mathrm{Hz/pixel}$. The durations of the diffusion gradient pulses were adjusted to null the eddy currents with the assumed τ, according to equations 5.12 (a)-(d). The b-values for both encodings were $b_1 = b_2 = 0.5\,\mathrm{ms}/\mu\mathrm{m}^2$.

The resulting mean CV over the whole volume can be seen in figure 6.1.There is a plateau where the CV is minimal, with its center roughly at $\tau = 70$ ms. This value was chosen for τ in all further measurements.

For the purpose of investigating the effectiveness of the eddy current compensation, all combinations of compensated and uncompensated encodings (u/u, c/u, u/c and c/c) were examined. Most imaging parameters were the same as for the estimation of τ. The timing had to be slightly adjusted for the different combinations of compensated and uncompensated encoding. In the case of uncompensated encodings, the total diffusion time T_D was 27 ms, the gradient duration δ was 9.44 ms and the amplitude $g = 77.4\,\mathrm{mT/m}$. For compensated encodings T_D was 38 ms, the gradient durations were 3.14, 7.73, 8.14 and 2.73 ms and $g = 78.7\,\mathrm{mT/m}$. The TE for the four different combinations were 94, 105, 85 and 96 ms for u/u, c/u, u/c and c/c respectively, with t_m-values of 20, 10, 0 and 0 ms.

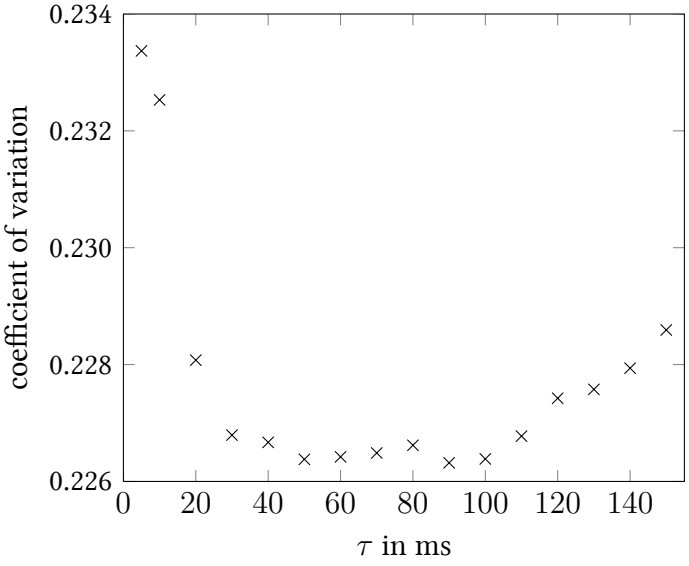

Figure 6.1: CV for different assumed eddy current decay times τ. The CV was determined as the mean value over the whole imaging volume. This figure was previously published in [MWKL17], copyright 2015 by Wiley Periodicals, Inc.

The corresponding CV maps are shown in figure 6.2. The grid points are visibly blurred in the phase encoding direction, which was downwards in all measurements. The blurring gets worse towards the outer parts of the image. At the upper edge of the phantom, there are distortions due to the susceptibility differences between the water and an air bubble. This heightens the effect of the eddy-current-induced distortions, which can be seen by the large areas with high CV.The blurring as well as the edge artifacts are reduced when using the eddy current compensation. Thereby, it can be seen that the second diffusion encoding plays a larger role in the overall effect than the first one, as the u/c measurements show a lower CV than the c/u measurements. In the case c/c (figure 6.2d), a bright spot above the ROI can be seen, which stems from concomitant field artifacts.

The mean CV over the white ROI in figure 6.2 is depicted in figure 6.3 for all four compensation combinations and the baseline measurement. The ROI has been chosen to exclude the major concomitant field artifacts in the c/c measurements. The CV without compensation is $\mathrm{CV}_{\mathrm{u/u}} = (4.37 \pm 0.09)\%$ (mean $\pm$ standard deviation over the slices). It is reduced to $\mathrm{CV}_{\mathrm{c/c}} = (3.62 \pm 0.10)\%$ for the full compensation, with only one compensated encoding it is $\mathrm{CV}_{\mathrm{c/u}} = (4.44 \pm 1.3)\%$ and $\mathrm{CV}_{\mathrm{u/c}} = (3.73 \pm 0.10)\%$. $\mathrm{CV}_{\mathrm{c/u}}$ is slightly larger than $\mathrm{CV}_{\mathrm{u/u}}$. Thus, the c/u scheme, shows worse results in the ROI analysis than the u/u scheme. The ROI covers only a small part in the central area of the phantom, where the effects of eddy current distortions are small. Over the whole image, c/u gives better results as can be seen, for example, at the upper edge of the phantom. The CV cannot be reduced to the baseline value of $\mathrm{CV}_{\mathrm{baseline}} = (2.9 \pm 0.09)\%$ in any of the compensation combinations.

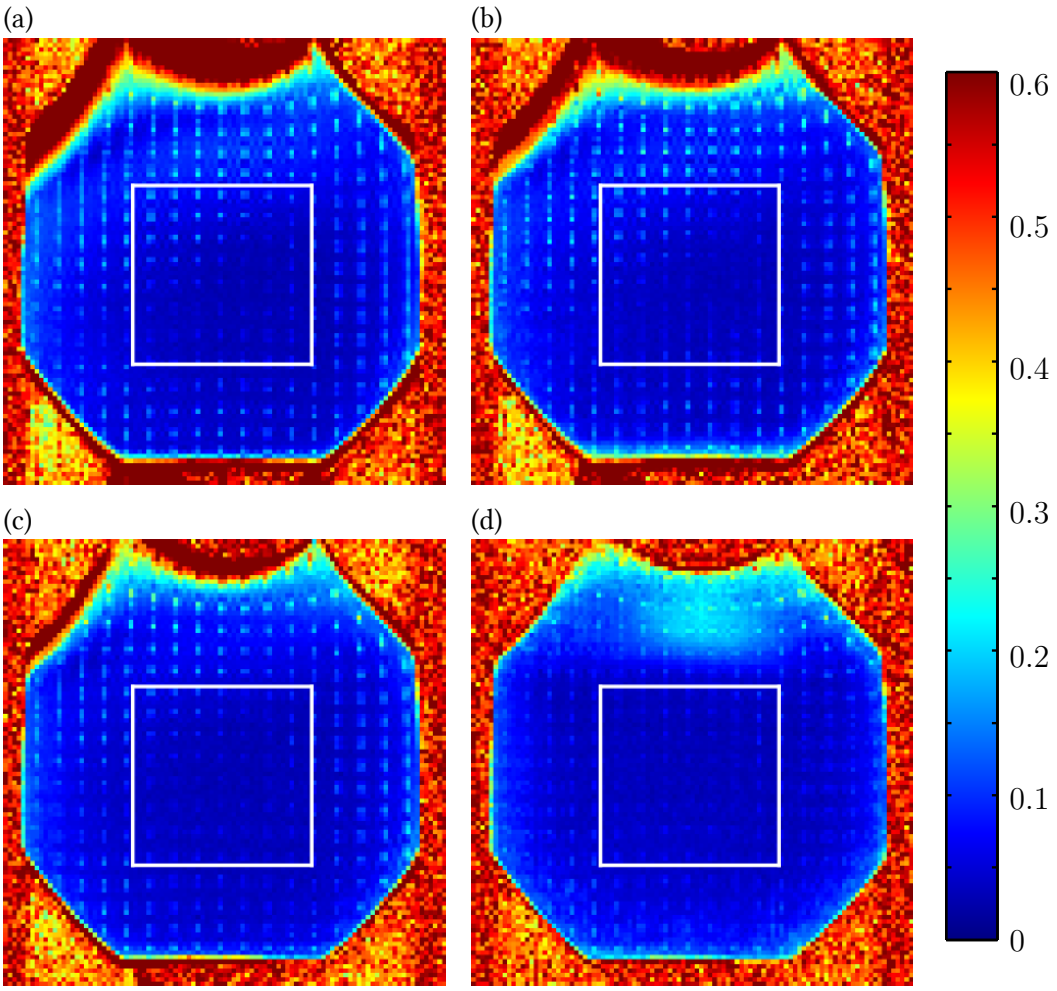

Figure 6.2: CV maps for an exemplary slice of the grid phantom in DDE measurements. The grid points are blurred along the phase encoding direction (up–down) because of eddy current artifacts. Additionally, a high CV appears at the edge of the phantom. These artifacts are most abundant for the u/u (a) measurement. They decrease for c/u (b) and u/c (c). The best results are achieved in the case of c/c (d). The white square was used for ROI analysis. The area with a higher CV above the ROI in the c/c measurements can be attributed to concomitant field artifacts. This figure was previously published in [MWKL17], copyright 2015 by Wiley Periodicals, Inc.

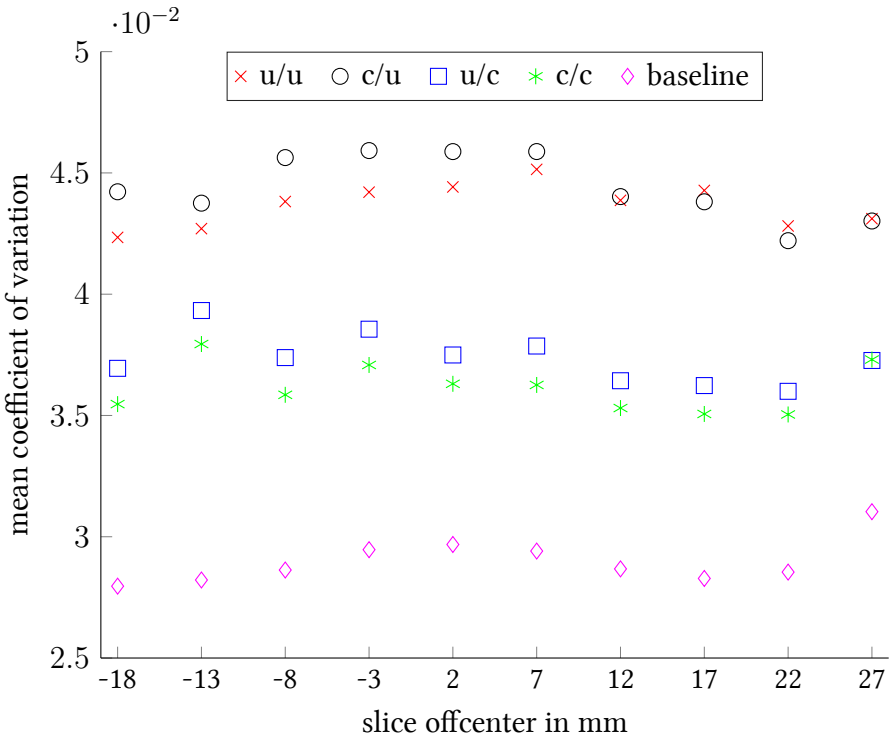

Figure 6.3: CV for different compensation combinations in DDE. The values were obtained as mean value over the ROI shown in figure 6.2 as white rectangle. The ROI size was 41^2 pixels. This figure was previously published in [MWKL17], copyright 2015 by Wiley Periodicals, Inc.

6.1.2 String Phantom Measurements

The measurements of the string phantom were performed with a $T_D = 39\,\text{ms}$ for each encoding and $\text{TE} = 110\,\text{ms}$, the repetition time was $\text{TR} = 2000\,\text{ms}$. Both encodings were compensated for eddy current, which lead to the same gradient durations in both encodings of 1.47, 9.82, 9.74 and 1.82 ms. The nominal in-plane resolution was $3 \times 3\,\text{mm}^2$ with a FOV of $126 \times 300\,\text{mm}^2$ and a slice thickness of 5 mm. A partial Fourier factor of 6/8 was used and the readout bandwidth was 3125 Hz/pixel. The maximal gradient amplitude was limited to 79.5 mT/m. For the measurement of the q-dependence, $t_m = 20\,\text{ms}$ was used, while for the t_m-dependence the q-value was $0.25\,\mu\text{m}^{-1}$. For the relation of FA to μFA, $q = 0.25\,\mu\text{m}^{-1}$ and $t_m = 20\,\text{ms}$ were used. The μFA, FA and correlation tensor $\underline{\underline{Q}}$ were calculated pixelwise and for the dependence measurements, the mean was calculated afterwards for a ROI over the fiber as well as for one over the agarose gel surrounding it (figure 5.5).

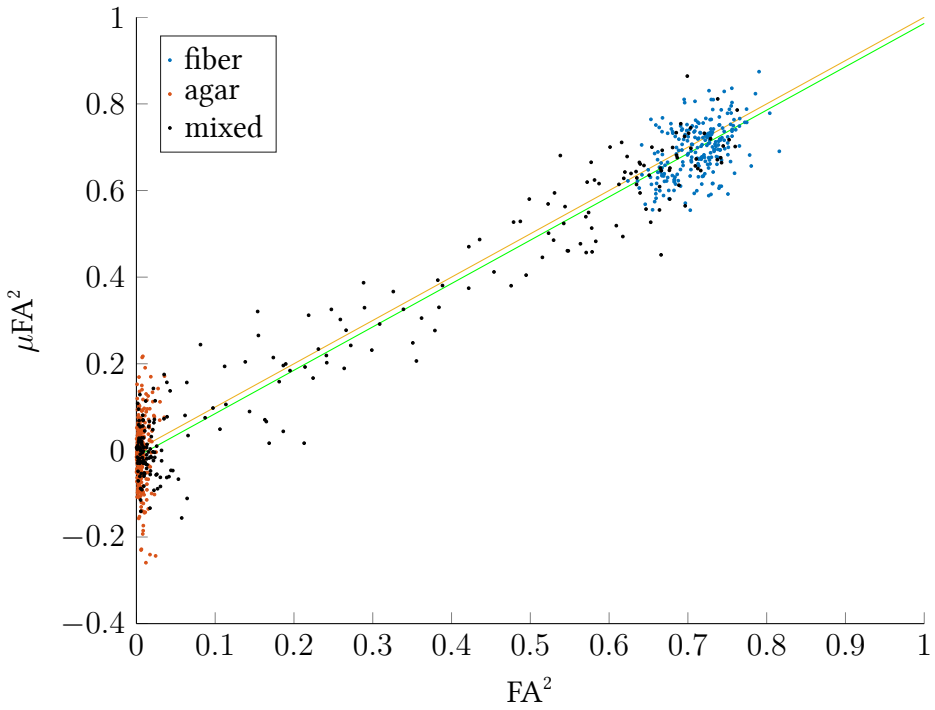

Figure 6.4: Scatter plot of μFA^2 against FA^2 in the string phantom. The values are spread around the line of identity (yellow line). In the agarose gel, where no diffusion anisotropy is present, the values cluster around zero. Since one measures μFA^2, its values can become negative due to noise, while the definition of FA allows only for positive values. The black dots belong to the pixels between the two ROIs in figure 5.5. The green line shows a linear fit.

Figure 6.4 shows a scatter plot of FA^2 against μFA^2. The squared values were chosen because the measured μFA^2 can become negative for small μFA-values due to noise. The pixels attributed to the fiber (shown in blue) show similar values for μFA^2 and FA^2 with mean and standard deviation $\overline{\mu\text{FA}^2} = 0.76 \pm 0.05$ and $\overline{\text{FA}^2} = 0.84 \pm 0.02$. The agarose gel

pixels exhibit very small FA^2-values with a slightly positive mean value $\overline{FA^2} = 0.07 \pm 0.03$, while $\overline{\mu FA^2} = -0.01 \pm 0.05$ can be considered zero.

The dependency of the μFA on t_m and q can be seen in figure 6.5. In the fiber (figure 6.5a and 6.5b), there is only a small dependence on t_m. The reduction is about 0.02 over the total t_m range of 20 ms. The FA and μFA show nearly identical values in all measurements with $q > 0.15\,\mu m^{-1}$. For small q-values, the μFA is overestimated for high anisotropies.

In the case of no diffusion anisotropy, as is given in agarose gel (figure 6.5c and 6.5d), there is no t_m dependence, while for low q-values the μFA^2 varies strongly around 0.

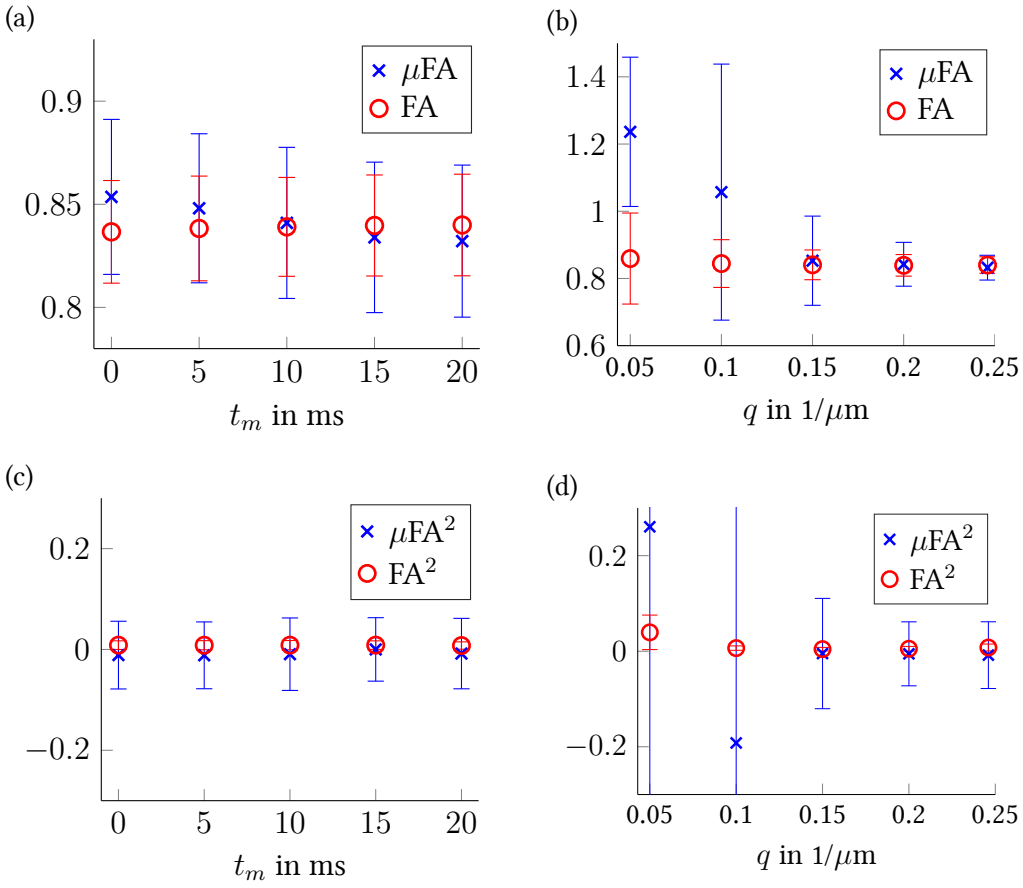

Figure 6.5: Dependencies of the μFA on t_m and q. The μFA depends only slightly on t_m in the fiber (a), while no dependence is seen in agarose gel (c). For small q-values, the μFA becomes very noisy ((b) and (d)) and is overestimated in the fiber (b). In agarose gel pixels (d), the noise is so large that the standard deviation (std) is not shown completely for $q = 0.05\,\mu m^{-1}$ (std = 10.0) and $q = 0.1\,\mu m^{-1}$ (std = 1.3). For the agarose gel ((c) and (d)), μFA^2 and FA^2 are shown instead of μFA and FA. As μFA^2 is the measured quantity, negative values can appear due to noise. The FA shows no dependence on the q-value or on t_m.

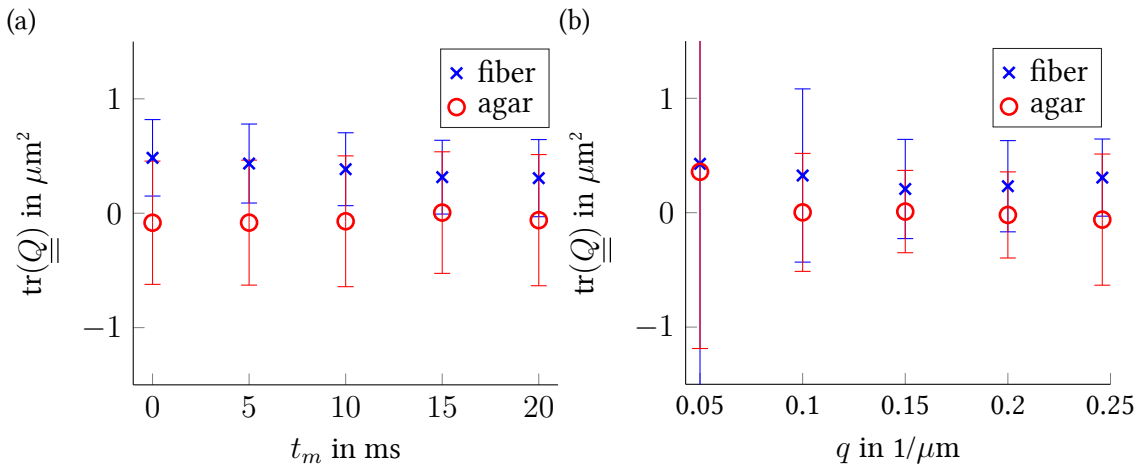

Figure 6.6: Dependencies of $\mathrm{tr}(\underline{\underline{Q}})$ on t_m and q. In agarose gel, $\mathrm{tr}(\underline{\underline{Q}})$ is zero. In the fiber, it is larger than zero and decreases with increasing t_m. There is no clear dependence on q. The standard deviation of the measurements with $q = 0.05\,\mu\mathrm{m}^{-1}$ is $3.0\,\mu\mathrm{m}^2$ for the fiber and $1.5\,\mu\mathrm{m}^2$ for the agarose gel.

In addition to the μFA , $\underline{\underline{Q}}$ was calculated and in figure 6.6 the mean values of $Q = \mathrm{tr}(\underline{\underline{Q}})$ over the two ROIs are shown. It can be seen that Q decreases with increasing t_m in the fiber, from $Q = (0.48 \pm 0.33)\,\mu\mathrm{m}^2$ for $t_m = 0\,\mathrm{ms}$ to $Q = (0.31 \pm 0.33)\,\mu\mathrm{m}^2$ for $t_m = 20\,\mathrm{ms}$. In the agarose gel, the value is basically zero for all t_m.

For the q-dependence no clear trends were found. For $q = 0.05\,\mu\mathrm{m}^{-1}$ the measurements were very noisy so that not the whole standard deviation is shown in figure 6.6b. This is the only measurement showing a Q in agarose gel similar to the one in the fiber. For all other q-values Q in agarose gel is close to zero, while in the fiber it is larger than zero.

6.2 Monte Carlo Simulations

The connections of μFA and Q with the experimental parameters t_m and T_D were also tested in Monte Carlo simulations for two simple two-dimensional geometries. One consisted of two parallel plates, which shows a diffusion anisotropy, the other one was a circle with no anisotropy. The results are shown in figure 6.7 for the plates and in figure 6.8 for the circle. In both cases, $\mathrm{tr}(\underline{\underline{Q}})$ clearly decreases with larger t_m. The dependence on T_D is smaller and only present if the long t_m limit is not reached. In the long t_m limit, $\underline{\underline{Q}}$ is zero independent of the diffusion time. If the limit is not reached, Q raises with T_D until its maximum, which is determined by t_m.

The μFA shows no dependence on t_m for the parallel plates, but it rises with T_D. For the circle the μFA shows a similar behavior as Q, but decreases faster than Q for increasing t_m. If the long t_m limit is reached the μFA is zero independent of T_D.

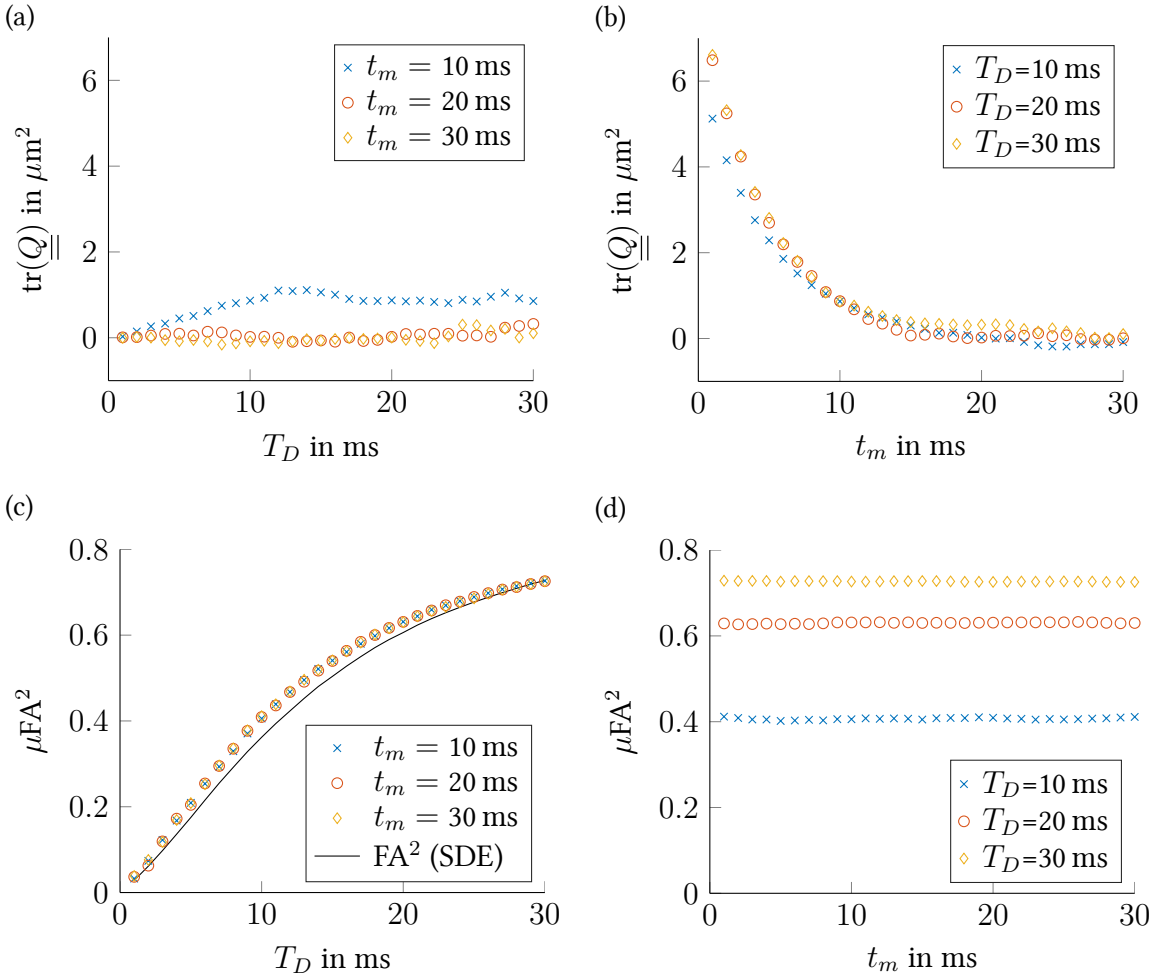

Figure 6.7: Monte Carlo results for two parallel plates. The plate distance was 10 μm and q was 0.1 $\mu\mathrm{m}^{-1}$. The signal was calculated for 20 direction combinations. The black line in (c) shows the FA^2 from simulations of a SDE sequence with varying T_D.

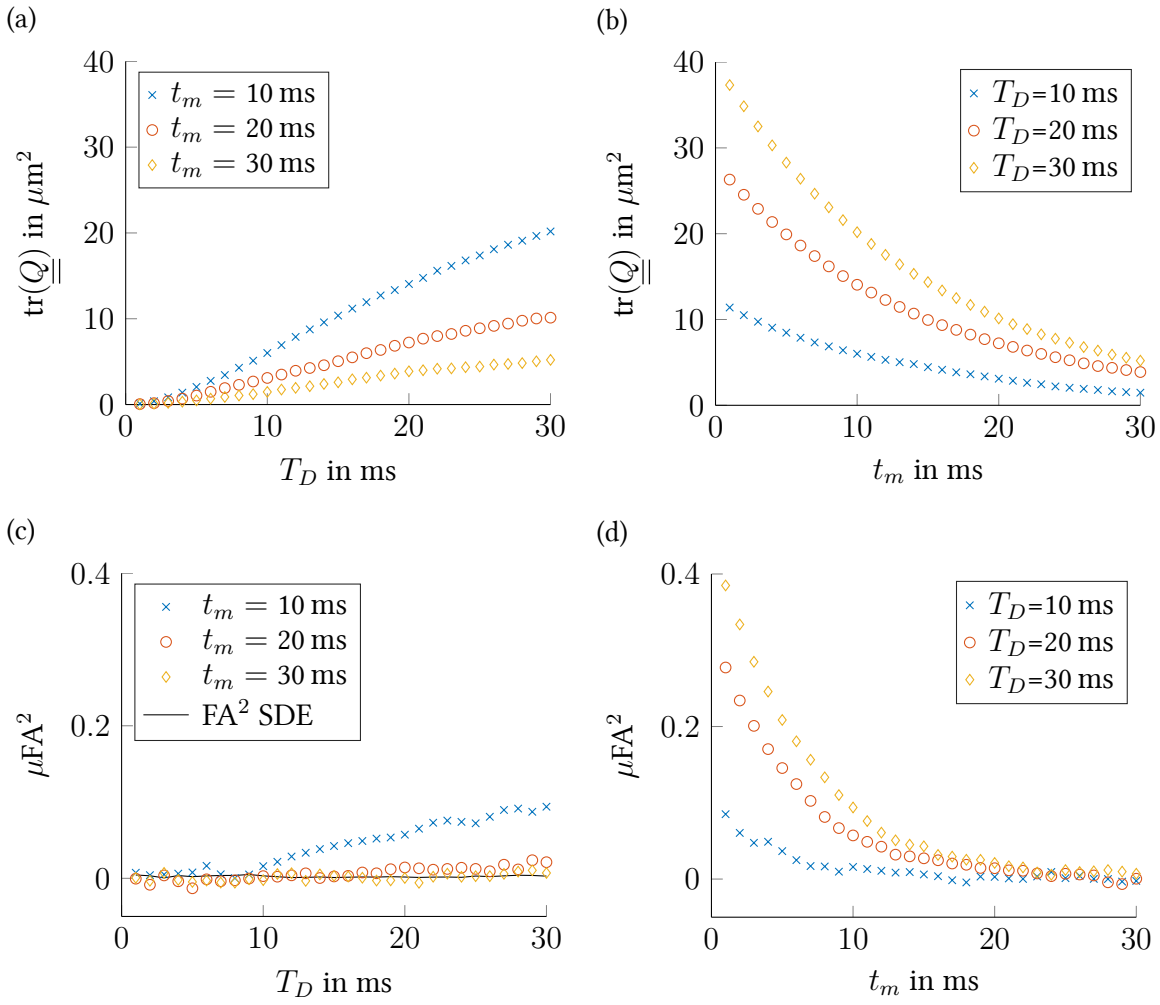

Figure 6.8: Monte Carlo results for a circle. The radius was 10 μm and q was 0.1 μm^{-1}. The signal was calculated for 20 direction combinations. The black line in (c) shows the FA^2 from simulations of a SDE sequence with varying T_D.

6.3 In Vivo Experiments

For the in vivo measurements of the μFA, the heads of six healthy volunteers were scanned with the u/u and c/c scheme. In five cases, an additional standard diffusion sequence was acquired to automatically segment gray and white matter and ventricles. In the sixth case (volunteer number 4), the DDE measurement itself was used. Voxels with a FA higher than 0.35 and a MD between 0.35 and 1 µm^2/ms were classified as white matter. Voxels with a FA between 0.02 and 0.15 and a MD between 0.5 and 1.3 µm^2/ms were classified as gray matter [NLvW+13, MWKL17]. Voxels with a MD higher than 1.5 µm^2/ms were marked as ventricles.

The nominal in plane resolution was 3×3 mm^2. 20 slices, with a slice thickness of 3 mm, were acquired with TR = 4000 ms. The FOV was 300×270 mm^2. A partial Fourier factor of 6/8 was used and additionally a GRAPPA factor of 2. The b-value in each diffusion encoding was 0.5 ms/µm^2. In the uncompensated $T_D = 27$ ms, with $\delta = 9.26$ ms and a gradient amplitude of 78.3 mT/m was used for each encoding and $t_m = 16$ ms and TE = 86 ms were chosen. In the compensated measurements, the timing parameters were $T_D = 31$ ms ($\delta_{1-4} = 2.34, 8.67, 8.84 and 2.17$ ms), $t_m = 10$ ms and TE = 104 ms. The gradient amplitude was 79 mT/m. Additionally an image without diffusion encoding was acquired for both DDE schemes.

The standard diffusion imaging was performed with the same resolution, slices and FOV. The b-values were 0 and 1.0 ms/µm^2, 20 diffusion directions were acquired, with a TE = 62 ms.

In figure 6.9, FA and μFA maps of a representative slice of each volunteer are shown. The μFA exhibits larger areas of high anisotropies than the standard FA, calculated from the compensated measurements. The uncompensated μFA maps show elevated values in the ventricles and the gray matter, while the white matter shows similar values. This is also represented in the mean values over these three types of brain matter, as can be seen in table **??**. There is a largely increased μFA in the ventricles and slightly higher values in gray matter for the u/u measurements. In white matter no clear trend can be seen.

An enlarged image of a fiber crossing is shown in figure 6.10. In figure 6.10a, the whole brain slice is depicted in a color encoded FA map, where each color represents the main fiber direction in the voxel, red for right-left, blue for up-down and green for perpendicular to the shown slice. The fiber crossing shows a reduction in FA (0.35 ± 0.03) compared to the coherent fiber (0.64 ± 0.04) (green arrow in 6.10e), which is not present in the μFA maps. They have similar values for the fiber crossing of 0.86 ± 0.02 and 0.87 ± 0.03 for the u/u (6.10d) and c/c (6.10e) sequence respectively In the fiber the μFA is 0.89 ± 0.02 (u/u) and 0.88 ± 0.02 (c/c). The reported values were obtained as mean $\pm$ standard deviation over the ROIs shown in figure 6.10b.

The red arrows in figure 6.10d and 6.10e point inside a ventricle, where the uncompensated measurement shows an increased μFA, which is reduced in the compensated measurements.

In figure 6.11, scatter plots of μFA against FA are shown for the gray and white matter masks of each volunteer. For better visibility, the identity line is plotted in green. The μFA values lie mostly above this line, so μFA is larger than FA. As mentioned above, the

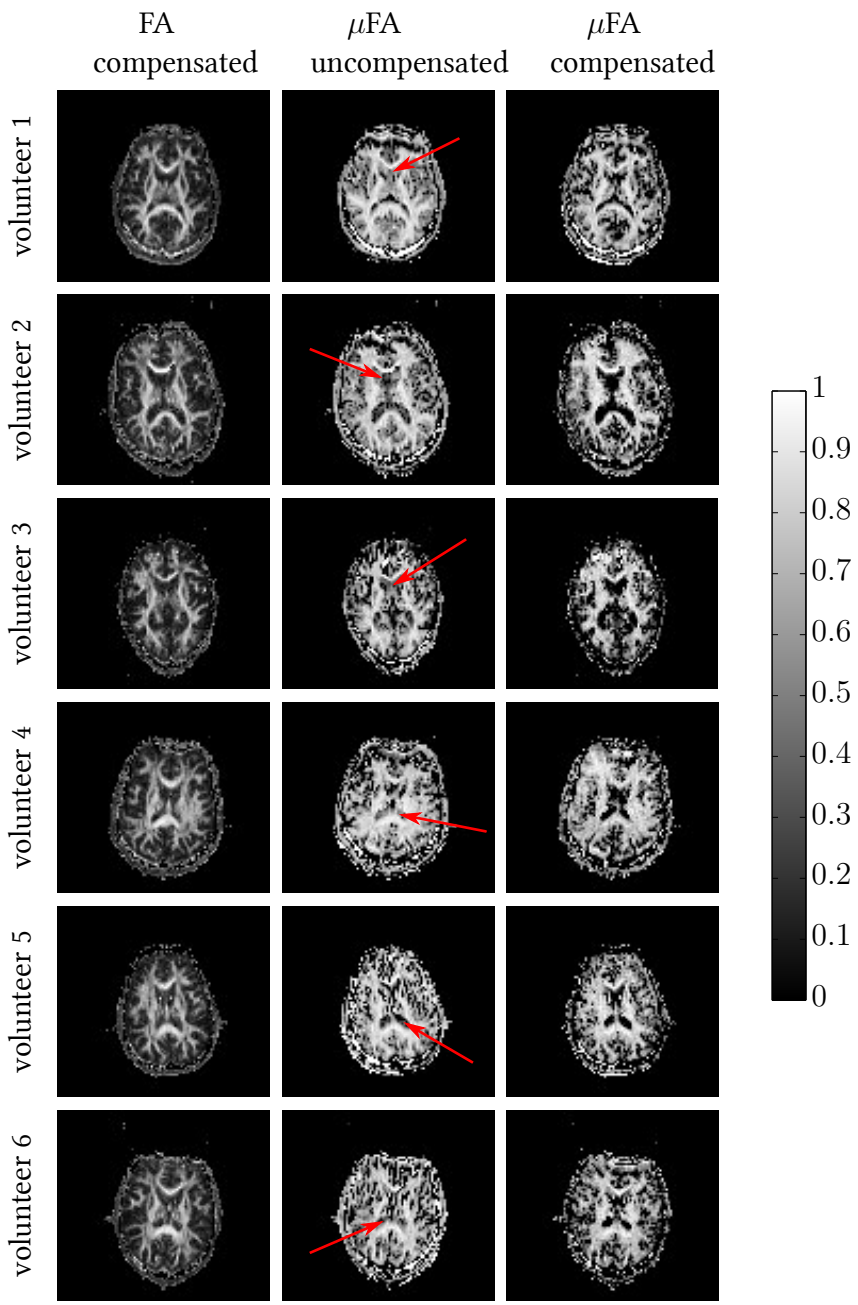

Figure 6.9: FA and μFA maps of the brains of six healthy volunteers. For each volunteer, an exemplary slice is shown. The FA map was calculated from the compensated measurement. The μFA shows larger areas of high values. The red arrows point to regions in the ventricle where the μFA is increased in the uncompensated measurements. These values are largely reduced in the compensated measurements. This is, to a lesser extent, the case in gray matter, while white matter remains unchanged. This figure was previously published in [MWKL17], copyright 2015 by Wiley Periodicals, Inc.

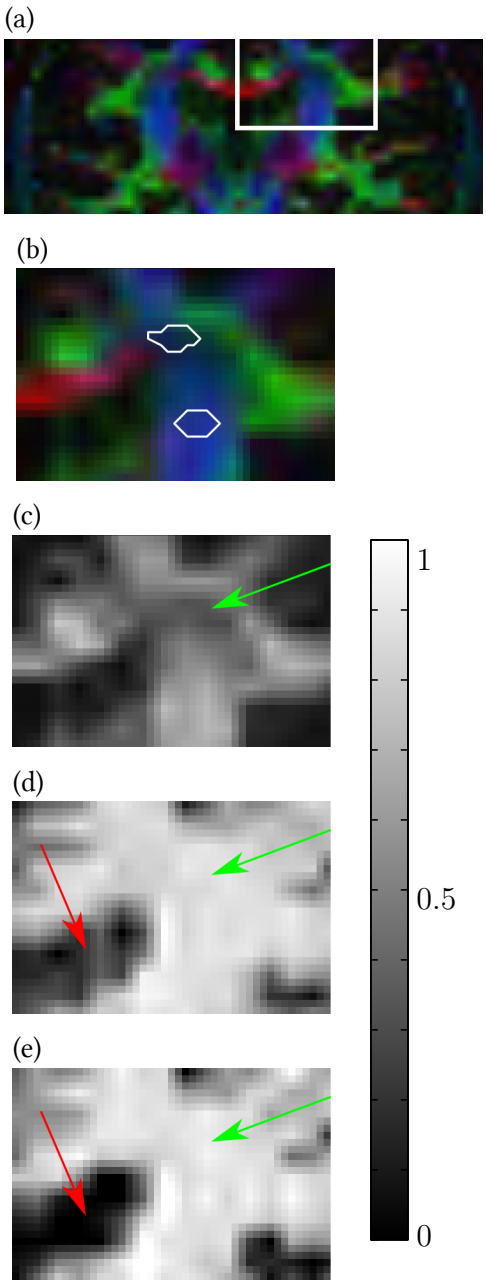

Figure 6.10: FA and μFA in fiber and fiber crossing. (a): Color FA map of the brain in a coronal slice. The white rectangular shows which area is enlarged in (b)-(e). (b): Detail of color FA map for ROI placement inside a fiber crossing with low FA (upper ROI) and inside a fiber (lower ROI). The FA (c) shows a drop in the crossing (green arrow), which does not exist in the μFA((d) and (e)). The uncompensated μFA measurements (d) show an increased value in the ventricle (red arrow), which cannot be seen in compensated measurements (e). All images shown here were tricubically interpolated to a threefold resolution. This figure was previously published in [MWKL17], copyright 2015 by Wiley Periodicals, Inc.

Table 6.1: Mean μFA $\pm$ standard deviation in different brain regions. This table was previously published in [MWKL17], copyright 2015 by Wiley Periodicals, Inc.

	white matter		gray matter		ventricles	
volunteer	u/u	c/c	u/u	c/c	u/u	c/c
1	0.79 ± 0.13	0.75 ± 0.16	0.54 ± 0.17	0.51 ± 0.19	0.47 ± 0.15	0.18 ± 0.23
2	0.78 ± 0.14	0.79 ± 0.14	0.57 ± 0.17	0.49 ± 0.19	0.36 ± 0.15	0.14 ± 0.21
3	0.79 ± 0.13	0.77 ± 0.14	0.52 ± 0.18	0.45 ± 0.21	0.53 ± 0.23	0.33 ± 0.34
4	0.74 ± 0.16	0.75 ± 0.16	0.57 ± 0.20	0.53 ± 0.18	0.61 ± 0.20	0.18 ± 0.23
5	0.76 ± 0.16	0.76 ± 0.15	0.63 ± 0.19	0.51 ± 0.20	0.59 ± 0.23	0.29 ± 0.28
6	0.72 ± 0.17	0.65 ± 0.21	0.60 ± 0.20	0.53 ± 0.21	0.68 ± 0.18	0.58 ± 0.31

Table 6.2: Pearson's r for $\mathrm{tr}(\underline{\underline{Q}})$ and μFA

volunteer	1	2	3	4	5	6
gray matter	0.67	0.60	0.60	0.83	0.51	0.48
white matter	0.66	0.55	0.54	0.75	0.53	0.58

segmentation for volunteer 4 was not done on additional images, but on the DDE measurement itself. Since FA boundaries were used, a vertical white stripe without any data points can be seen in figure 6.11d. The gray matter μFA-values are distributed over the whole range of allowed values, while in most cases only few values lie above 0.8. White matter voxels tend to higher μFA-values and only few lie below 0.4. In the FA-value white and gray matter are separated well in all volunteers, except number 6 where a strong overlap is present.

Figure 6.12 depicts the $Q = \mathrm{tr}(\underline{\underline{Q}})$ plotted against the μFA. It can be seen that Q increases with increasing μFA and is clearly non-zero. The Pearson's r correlation coefficient for gray and white matter for all six volunteers is given in table 6.2. The non-zero Q indicates that the two diffusion encodings were not independent and therefore that the long t_m limit was not achieved.

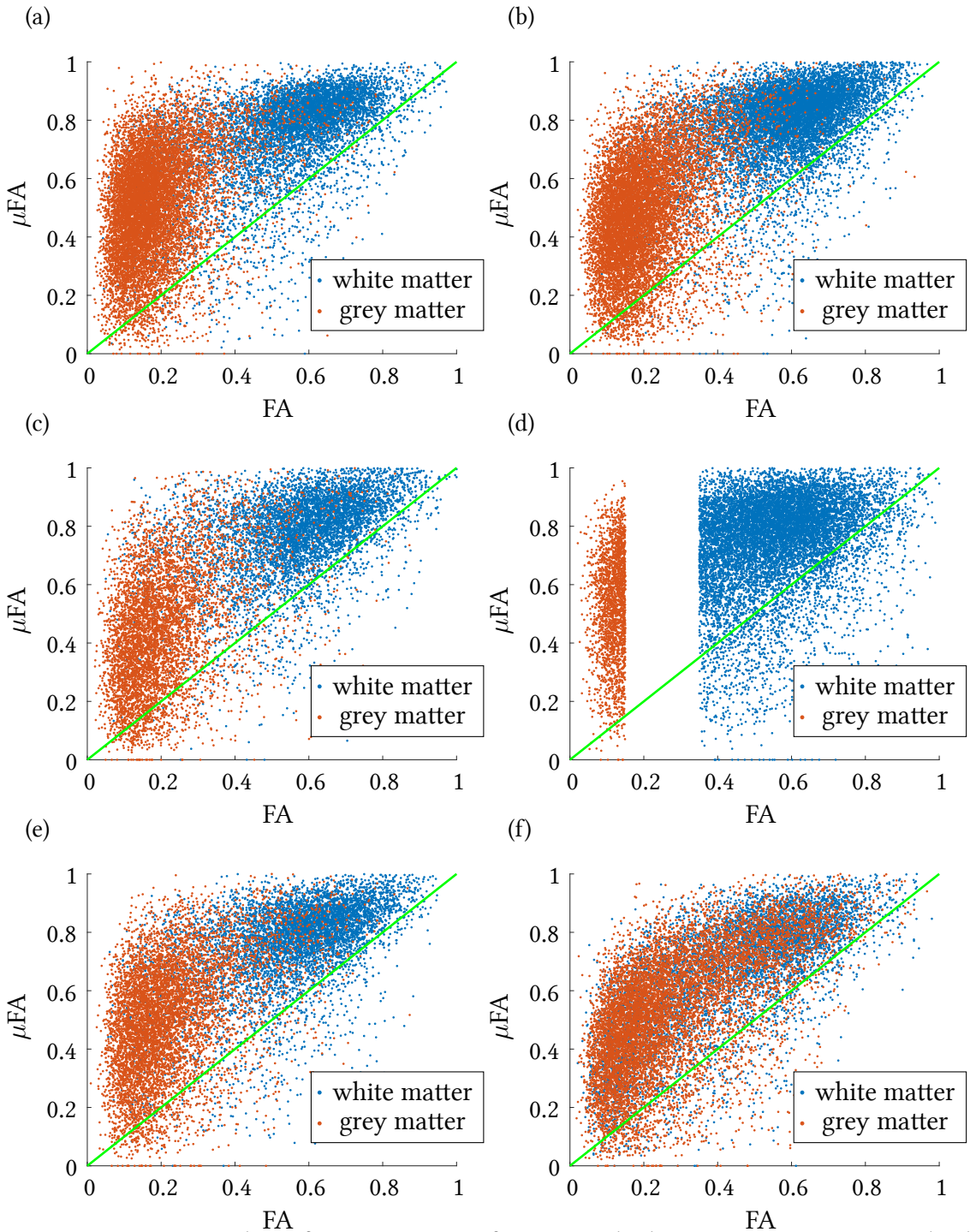

Figure 6.11: Scatter plots of μFA against FA for gray and white matter. For most pixels, the values lie above the identity line (green). For volunteer 4 (d), no independent diffusion measurement was available so that the masking was done on the DDE images, which leads to the white band.

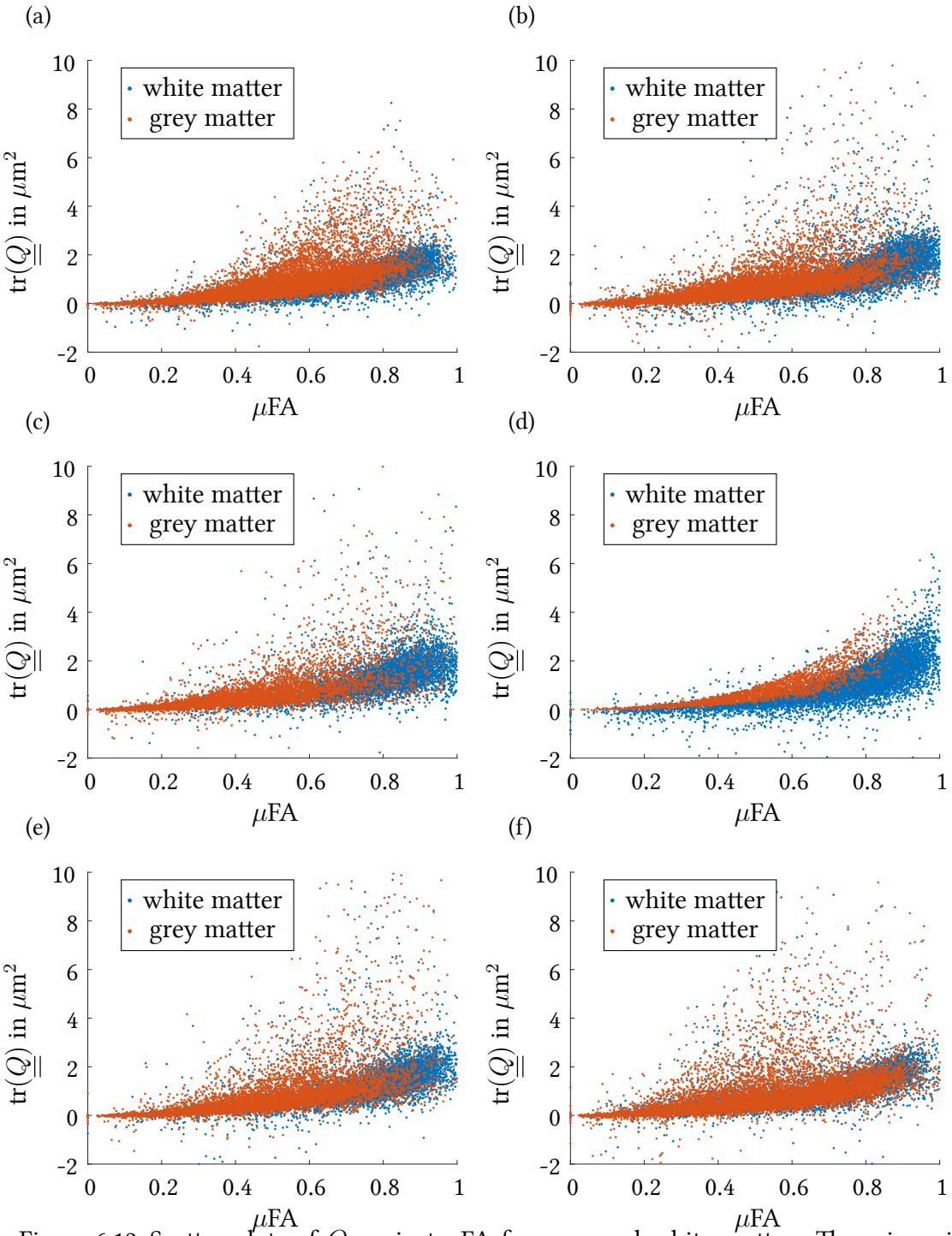

Figure 6.12: Scatter plots of Q against μFA for gray and white matter. There is a similar correlation between μFA and Q for all volunteers and for gray and white matter.

7 Results: Single Diffusion Encoding

The different kinds of artifacts, like flow, eddy currents, and concomitant fields, in diffusion MRI have, so far, mainly been treated individually. In this chapter, results are shown that demonstrate the possibility to compensate for these artifacts simultaneously by sequence design. First, numerical optimizations were done to maximize the b-value, while compensating for different artifacts with different sequence schemes (section 7.1). The sequence with the highest possible b-values was used for phantom experiments (section 7.2). In the final section, in vivo results are presented, which used the compensation combinations with the least artifacts in the phantom measurements.

7.1 Sequence Optimization

The maximal b-values, yielded by the optimization, are listed in tables 7.1-7.3 for each of the 20 sequences examined. Each table shows the results for a specific TE.

For many of the compensation combinations, different sequences show the same b-value. This is caused by the optimization setup, which allowed a gradient pulse duration of zero. For example, if concomitant field compensation is used alone, all sequences with a single refocusing RF pulse produce the same b-value. In such cases, the one with the lowest number of gradient pulses (or one with even less) is the best choice and all others can be traced back to it. As example, the case of no compensation is considered. All sequences with one refocusing pulse, except $+|+$, show the same b-value. The optimal sequence in that case and for this timing is actually $+-|+$. Thus, in the sequence $+-|+-$ the last gradient pulse has a duration of 0 or in $+-+|-+$ the third and fifth gradient pulses become zero.

The use of flow compensation alone reduces the maximal b-value to approximately 20-25 % of the value achievable with the Stejskal-Tanner sequence $+|+$, the exact fraction depends slightly on TE. For longer TE, the fraction gets higher. This pattern is the same for all compensation combinations. For some of the compensation schemes with the intermediate and long TE, the use of two refocusing RF pulses allows for higher b-values than the use of only one.

The use of eddy current compensation reduces the possible b-value less than flow compensation. The best results are achieved by the sequence $+|-+|-$, which is the TRSE sequence. However, it is not possible to compensate for flow with this sequence. The sequences with one pulse yield lower b-values for eddy current compensation than those with two. For only one RF pulse, the differences between flow compensation alone and eddy current compensation alone are only minor

Table 7.1: b-values in ms/µm² for TE = 55 ms and g = 40 mT/m

	none	flow	conco	eddy	flow conco	flow eddy	conco eddy	flow conco eddy
+|+	0.515	-	0.515	-	-	-	-	-
+|+|+	0.161	0.048	0.161	-	0.039	-	-	-
+−|+−	0.538	0.105	0.515	0.116	0.094	0.053	0.103	0.051
+−|−+	0.538	0.071	0.515	0.111	0.062	-	0.098	-
+|−+|−	0.290	-	0.161	0.274	-	-	0.145	-
+|+−|−	0.161	0.085	0.161	0.096	-	0.060	0.056	-
+−|+−+	0.538	0.105	0.515	0.116	0.094	0.053	0.103	0.051
+−+|−+	0.538	0.105	0.515	0.116	0.094	0.062	0.103	0.059
+−|−+−	0.538	0.105	0.515	0.116	0.094	0.053	0.103	0.051
+−+|+−	0.538	0.105	0.515	0.116	0.094	0.059	0.103	0.056
+|−+|−+	0.290	0.093	0.161	0.274	0.048	0.007	0.145	0.007
+−|+−|+	0.290	0.093	0.161	0.274	0.048	0.011	0.145	0.011
+−|−+|−	0.290	0.093	0.161	0.274	0.048	-	0.145	-
+|−+|+−	0.290	0.093	0.161	0.274	0.048	-	0.145	-
+|+−|−+	0.290	0.093	0.161	0.124	0.048	0.060	0.056	0.013
+−|−+|+	0.290	0.093	0.161	0.099	0.048	0.060	0.056	0.013
+−|+−|−	0.290	0.093	0.161	0.100	0.048	0.060	0.056	0.018
+|+−|+−	0.290	0.093	0.161	0.125	0.048	0.060	0.056	0.015
+|−+−|−	0.290	0.085	0.161	0.274	-	0.060	0.145	-
+|+−+|−	0.290	0.085	0.161	0.274	-	0.060	0.145	-

Table 7.2: b-values in ms/µm² for TE = 85 ms and g = 40 mT/m

	none	flow	conco	eddy	flow conco	flow eddy	conco eddy	flow conco eddy
$+\|+$	3.092	-	3.092	-	-	-	-	-
$+\|+\|+$	2.029	0.580	1.817	-	0.325	-	-	-
$+-\|+-$	3.136	0.658	3.092	0.732	0.637	0.371	0.706	0.327
$+-\|-+$	3.136	0.390	3.092	0.642	0.373	-	0.618	-
$+\|-+\|-$	2.351	-	2.029	2.207	-	-	1.886	-
$+\|+-\|-$	2.029	0.426	2.029	1.005	-	0.342	0.736	-
$+-\|+-+$	3.136	0.658	3.092	0.732	0.637	0.371	0.706	0.327
$+-+\|-+$	3.136	0.658	3.092	0.732	0.637	0.416	0.706	0.410
$+-\|-+-$	3.136	0.658	3.092	0.732	0.637	0.371	0.706	0.327
$+-+\|+-$	3.136	0.658	3.092	0.732	0.637	0.382	0.706	0.377
$+\|-+\|-+$	2.351	0.674	2.029	2.207	0.580	0.167	1.886	-
$+-\|+-\|+$	2.351	0.674	2.029	2.207	0.580	0.368	1.886	0.339
$+-\|-+\|-$	2.351	0.674	2.029	2.207	0.580	-	1.886	-
$+\|-+\|+-$	2.351	0.674	2.029	2.207	0.580	-	1.886	-
$+\|+-\|-+$	2.351	0.674	2.029	1.005	0.580	0.342	0.736	0.163
$+-\|-+\|+$	2.351	0.674	2.029	1.005	0.580	0.342	0.736	0.165
$+-\|+-\|-$	2.351	0.674	2.029	1.005	0.580	0.463	0.736	0.354
$+\|+-\|+-$	2.351	0.674	2.029	1.005	0.580	0.342	0.736	0.227
$+\|-+-\|-$	2.351	0.426	2.029	2.207	-	0.342	1.886	-
$+\|+-+\|-$	2.351	0.426	2.029	2.207	-	0.342	1.886	-

Table 7.3: b-values in ms/µm^2 for TE $= 115$ ms and $g = 40$ mT/m

	none	flow	conco	eddy	flow conco	flow eddy	conco eddy	flow conco eddy
$+\|+$	9.275	-	9.275	-	-	-	-	-
$+\|+\|+$	7.246	2.013	7.246	-	1.950	-	-	-
$+-\|+-$	9.341	2.048	9.275	2.358	2.016	1.098	2.318	0.852
$+-\|-+$	9.341	1.147	9.275	1.811	1.123	0.077	1.776	-
$+\|-+\|-$	7.762	-	7.246	7.369	-	-	6.855	-
$+\|+-\|-$	7.246	1.196	7.246	4.066	-	1.078	2.820	-
$+-\|+-+$	9.341	2.048	9.275	2.358	2.016	1.098	2.318	0.852
$+-+\|-+$	9.341	2.048	9.275	2.358	2.016	1.260	2.318	1.251
$+-\|-+-$	9.341	2.048	9.275	2.358	2.016	1.098	2.318	-
$+-+\|+-$	9.341	2.048	9.275	2.358	2.016	1.105	2.318	1.098
$+\|-+\|-+$	7.762	2.156	7.246	7.369	2.013	0.678	6.855	0.564
$+-\|+-\|+$	7.762	2.156	7.246	7.369	2.013	1.771	6.855	1.534
$+-\|-+\|-$	7.762	2.156	7.246	7.369	2.013	0.012	6.855	-
$+\|-+\|+-$	7.762	2.156	7.246	7.369	2.013	-	6.855	-
$+\|+-\|-+$	7.762	2.156	7.246	4.066	2.013	1.078	2.820	0.594
$+-\|-+\|+$	7.762	2.156	7.246	4.066	2.013	1.078	2.820	0.616
$+-\|+-\|-$	7.762	2.156	7.246	4.066	2.013	1.633	2.820	1.169
$+\|+-\|+-$	7.762	2.156	7.246	4.066	2.013	0.977	2.820	0.846
$+\|-+-\|-$	7.762	1.196	7.246	7.369	-	1.078	6.855	-
$+\|+-+\|-$	7.762	1.196	7.246	7.369	-	1.078	6.855	-

For the concomitant field compensation, the highest b-values can be achieved with the Stejskal-Tanner sequence, which can also be achieved by any sequence with one RF pulse. The sequences with two refocusing pulses generally show lower maximal b-values.

If flow and eddy current compensation are used at the same time, the possible b-value is lower than for each compensation individually and only gives about 10–20 % of the Stejskal-Tanner b-value. The use of flow and concomitant field compensation yields higher b-values for only one RF pulse than for two. The difference decreases for longer TE. This is the other way round for concomitant field and eddy current compensation, where two RF pulses are more efficient than one and the effect increases with longer TE.

In the case of short and intermediate TE, the best results for the full compensation are achieved by sequences with only one refocusing pulse. For long TE the highest b-values are achieved with two RF pulses. Since shorter TE are favorable in most cases, as they yield higher signal-to-noise ratio (SNR), the sequence $+-+|-+$ has been chosen for the measurements.

7.2 Phantom Measurements

7.2.1 Flow Compensation

The images used for validating the flow compensation, were acquired with a FOV of $252 \times 420\,\mathrm{mm}^2$, a nominal in-plane resolution of $4.2 \times 4.2\,\mathrm{mm}^2$, a slice thickness of $4.5\,\mathrm{mm}$, TE $=$ $90\,\mathrm{ms}$, TR $=$ $4000\,\mathrm{ms}$, a partial Fourier factor of 6/8 and a readout bandwidth of $1785\,\mathrm{Hz/pixel}$. Ten b-values between 0 and $0.8\,\mathrm{ms/\mu m^2}$ were acquired without flow and for the mean flow velocities $v_{\mathrm{flow},1} = (0.85 \pm 0.08)\,\mathrm{cm/s}$ and $v_{\mathrm{flow},2} = (1.71 \pm 0.11)\,\mathrm{cm/s}$. The diffusion encoding direction was chosen to be mainly in flow direction.

For the analysis, the signal was averaged over a ROI in one slice. The results of all compensation combinations for $v_{\mathrm{flow},1}$ and $v_{\mathrm{flow},2}$ are shown in figure 7.1. For the sequences that are not compensated at all or only for concomitant fields, the signal shows a steep initial drop until it decreases to the noise level. The sequences that are flow compensated show a similar signal decay to the measurements without flow. In the measurements with the higher flow velocity, there is a slight difference and the signal with flow decays a little bit faster. For both eddy-current-compensated sequences without flow compensation the signal curve lies between the other two groups, meaning it decreases faster than the flow-compensated sequences, but slower than the other non-flow-compensated ones.

7.2.2 Eddy Current Compensation

To validate the eddy current compensation, the grid phantom was used and images with 64 different diffusion directions were acquired with a b-value of $1.0\,\mathrm{ms/\mu m^2}$. For the measurements, TE $=$ $90\,\mathrm{ms}$, TR $=$ $4000\,\mathrm{ms}$ were chosen. The FOV was $432 \times 450\,\mathrm{mm}^2$ with a nominal resolution of $4.5 \times 4.5\,\mathrm{mm}^2$ and a slice thickness of $5\,\mathrm{mm}$ for all ten slices. The readout bandwidth was $2940\,\mathrm{Hz/pixel}$ and a partial Fourier factor of 6/8 was used.

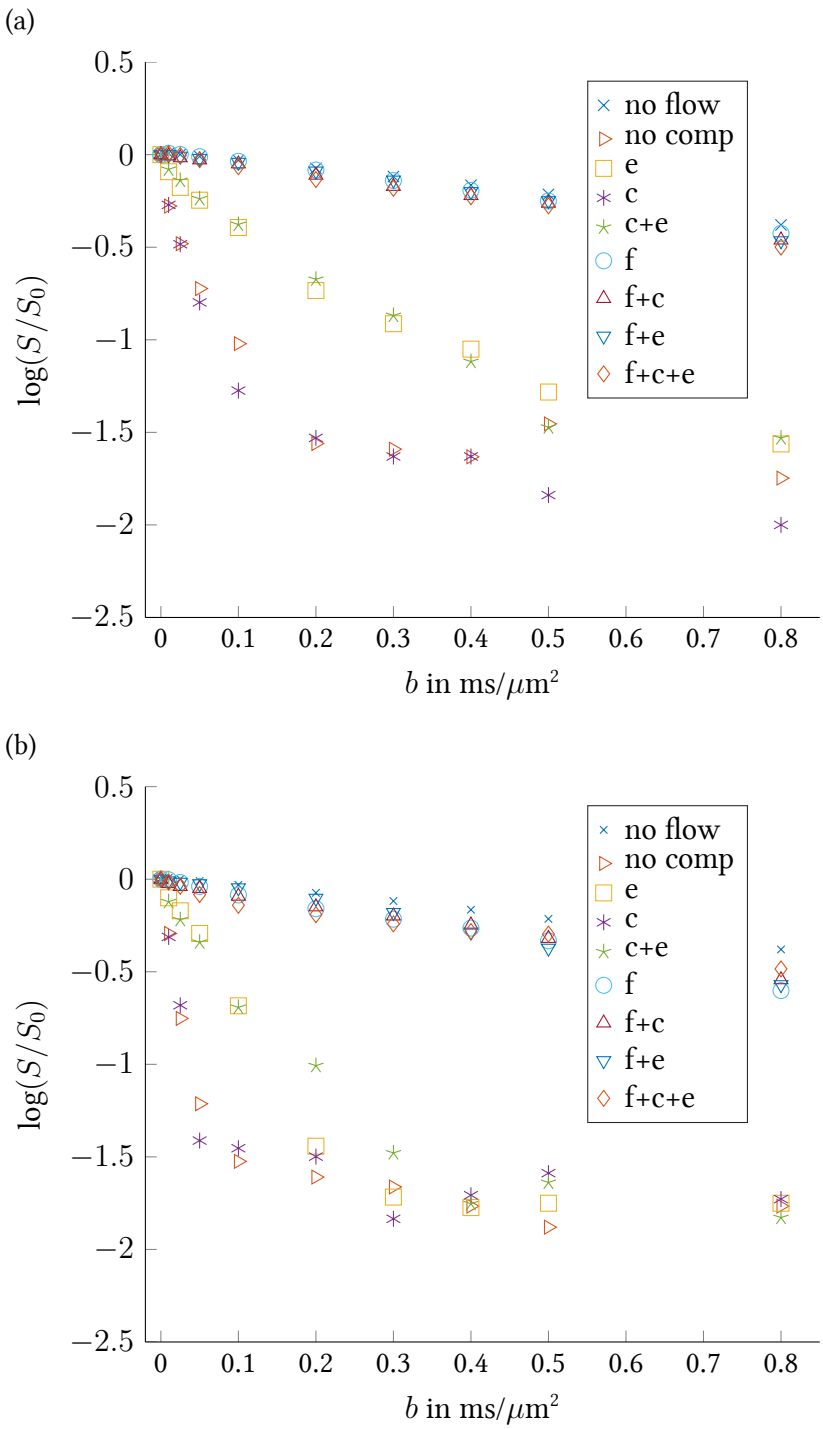

Figure 7.1: Diffusion measurements under flow. The measurements were performed for all compensation combinations of flow (f), concomitant fields (c) and eddy currents (e) with two flow velocities, a slower one (a) and one approximately twice as fast (b). Additionally, a measurement without flow was made. All flow-compensated measurements show a similar decrease in signal, which deviates only slightly from the measurement without flow.

The CV of the signal over the 64 directions was calculated on a pixel-by-pixel basis. The resulting maps are shown for one slice and all eight compensation combinations in figure 7.2. A difference between the maps is mainly visible on the outer areas of the grid and at the upper edge of the phantom.

The grid points are smeared out over several pixels in phase encoding direction, which was downwards in these measurements. In principal, the same holds true for the upper edge of the phantom, where, however, the smearing appears over larger areas and the CV shows larger values.

To quantify the eddy current compensation efficiency further, a ROI analysis was performed for three different ROIs: the square and the octagon shown in figure 7.2, as well as the whole image. The CV was averaged over the ROI and all slices simultaneously. The results are shown in figure 7.3. The overall highest CV of all ROIs can be seen for the concomitant-field-compensated and the uncompensated sequences. In the two small ROIs, all other sequences show similar CVs. This is different for the average over the whole imaging volume, where the eddy-current-compensated sequences, with and without flow compensation, show the lowest CVs. Flow and concomitant field compensation is slightly worse and an additional eddy current compensation does not improve this.

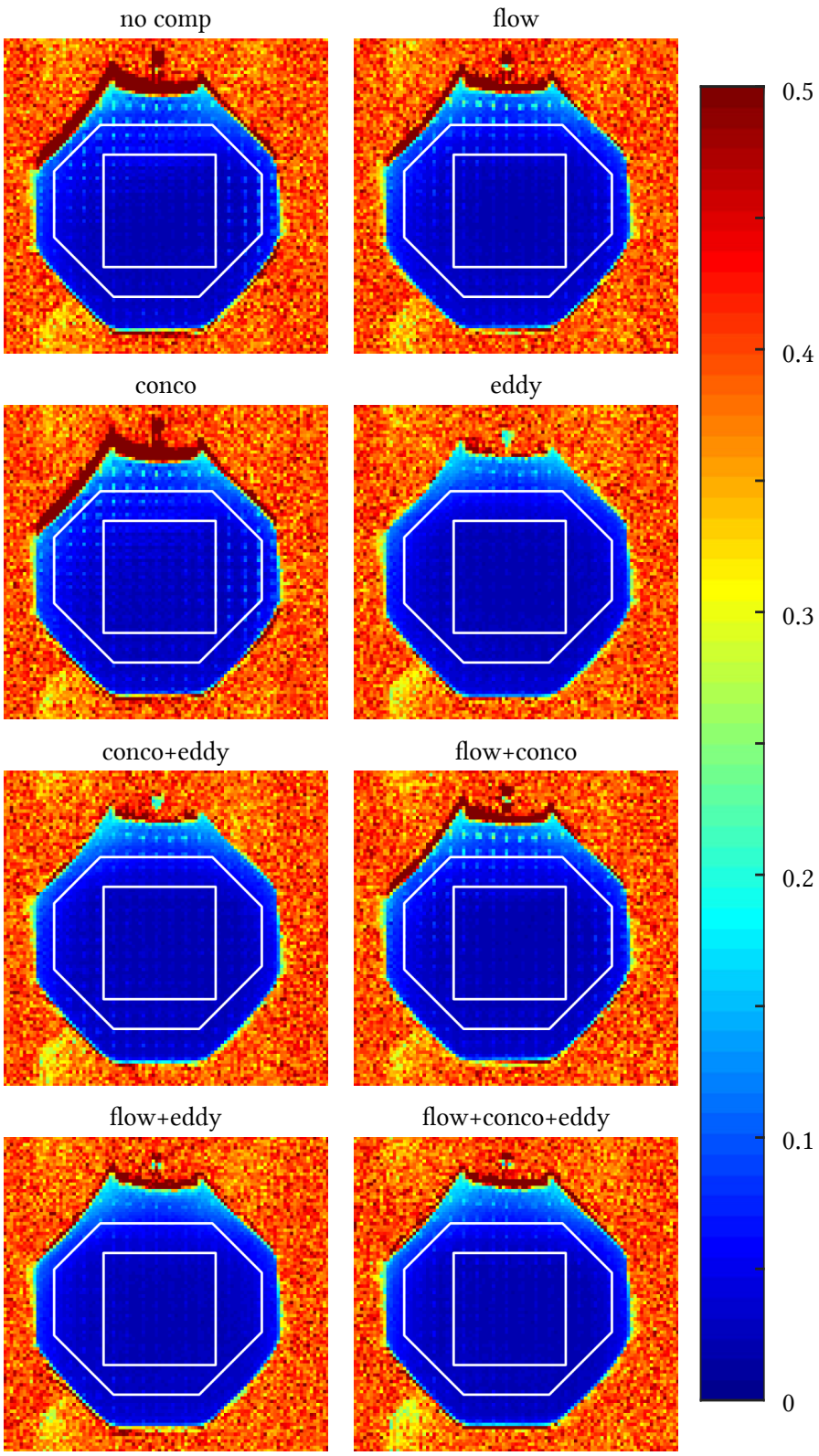

Figure 7.2: CV maps for one slice of the grid phantom for SDE measurements. The ROIs were used for comparing the mean CV for all compensation combinations. The use of eddy current compensation (eddy) reduces the CV, no matter which combination of flow and concomitant field (conco) compensation was used.

(a)

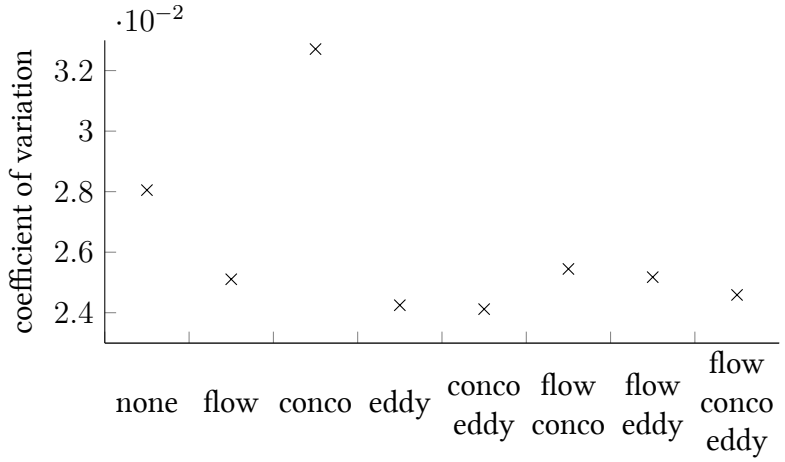

(b)

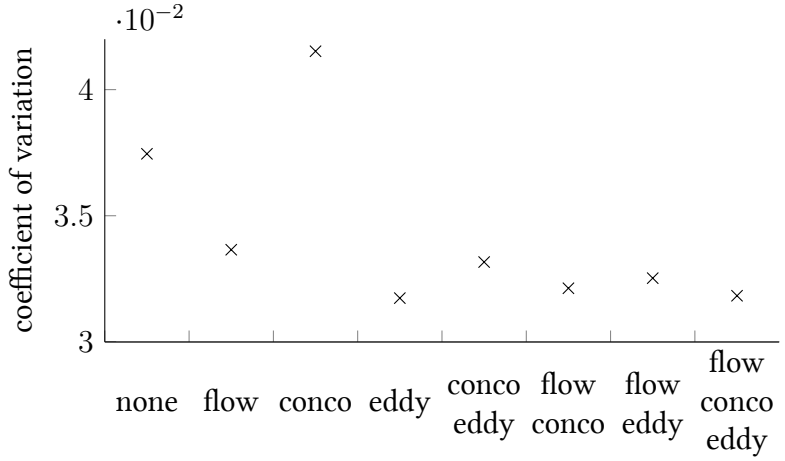

(c)

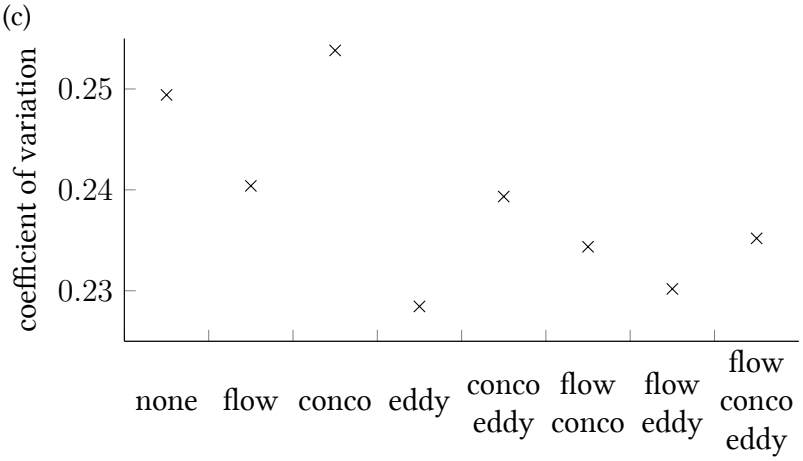

Figure 7.3: Coefficient of variation for all compensation combinations over different ROIs. The mean value over the rectangular (a) and octagonal (b) ROIs in figure 7.2 show similar trends with only marginal differences among most compensation combinations. This is different when the whole image is considered (c).

7.3 In Vivo Experiments

The effects of different compensation combinations were also examined in different regions of the human body. Diffusion weighted images of the brain, the abdomen and the prostate of healthy volunteers were acquired. Additionally, IVIM measurements of patients with prostate carcinoma were performed.

7.3.1 Brain

Two measurement series were performed in the brain. To show the improved stability of repeated measurements, an experiment with three b-values (0, 0.5 and 1.0 ms/µm^2), three orthogonal diffusion directions (x-, y- and z-direction) and ten repetitions was performed. The compensation combinations that were looked at were concomitant fields, flow, flow+concomitant fields, and flow+concomitant fields+eddy currents. The images were acquired with TE = 80 ms, TR = 5500 ms, a nominal in-plane resolution of $2.8 \times 2.8\,\text{mm}^2$ for 23 slices with a slice thickness of 5 mm and a FOV of $218 \times 280\,\text{mm}^2$. A partial Fourier factor of 6/8 and a bandwidth of 2780 Hz/pixel were used. The diffusion coefficient was calculated for the different directions individually as well as for the trace weighted images. To distinguish between diffusion coefficients determined from only one direction and those from the trace weighted images, the name ADC is used for the diffusion coefficient of a single direction and MD for the diffusion coefficient of the trace weighted images. The calculations were done for each repetition independently so that a CV could be calculated.

The CV for the MD is presented for all four compensation combinations in figure 7.4 for one exemplary slice. For better orientation, an image with $b = 0$ and a MD map for one repetition are also shown. It is visible that the CV is highest in the only concomitant-field-compensated case (figure 7.4c). It was reduced by using flow compensation (figure 7.4d). A further improvement was achieved by combining both compensation (figure 7.4e). Another slight improvement of the MD stability was seen when an additional eddy current compensation was used (figure 7.4f).

The differences between the compensation schemes look different in the slice in figure 7.5, which is 30 mm higher than the one in figure 7.4. The dependence of the ADC on the encoding direction can be seen in the first line. The other images show the CV of the ADC for the different directions and compensation combinations. In contrast to the slice in figure 7.4, a clear difference is seen between the full compensation and the flow+concomitant field compensation. The observed differences between the other compensation combinations remain unchanged from the slice in figure 7.4, although the overall CV seems slightly higher. There were no systematical differences between the CV maps for the different diffusion directions.

In the two presented slices, the median CV over the brain was determined by manually segmenting the whole brain based on a $b = 0$ image. The values are listed in tables 7.4 and 7.5. They show the same trends already described for the images. The median was chosen, as there were single pixels with very large CV-values, which would dominate the mean value. The CV of the ADC is higher than the corresponding CV of the MD for both slices and all compensation compensations

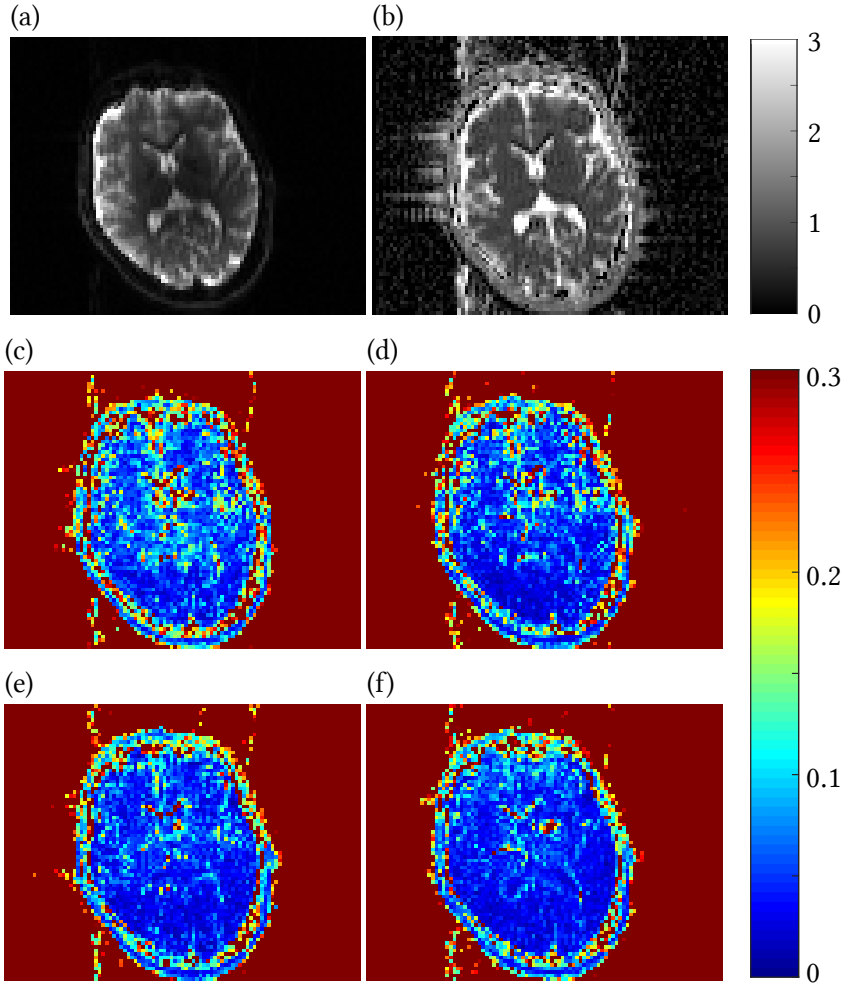

Figure 7.4: $B = 0$ image, MD and CV of MD in the brain for SDE measurements. The $b = 0$ image (a) in arbitrary units and the MD map (b) in $\mu m^2/ms$ are shown to provide anatomical information. (c)-(f) show the CV of the MD over 10 repetitions for different compensation schemes ((c): concomitant field, (d): flow, (e): flow+concomitant field, (f): flow+ concomitant field+eddy currents).

Table 7.4: Median CV corresponding to the slice shown in figure 7.4

compensation	MD	up–down	left–right	through plane
conco	0.063	0.075	0.077	0.081
flow	0.048	0.060	0.059	0.060
flow+conco	0.043	0.053	0.055	0.052
flow+conco+eddy	0.039	0.050	0.052	0.048

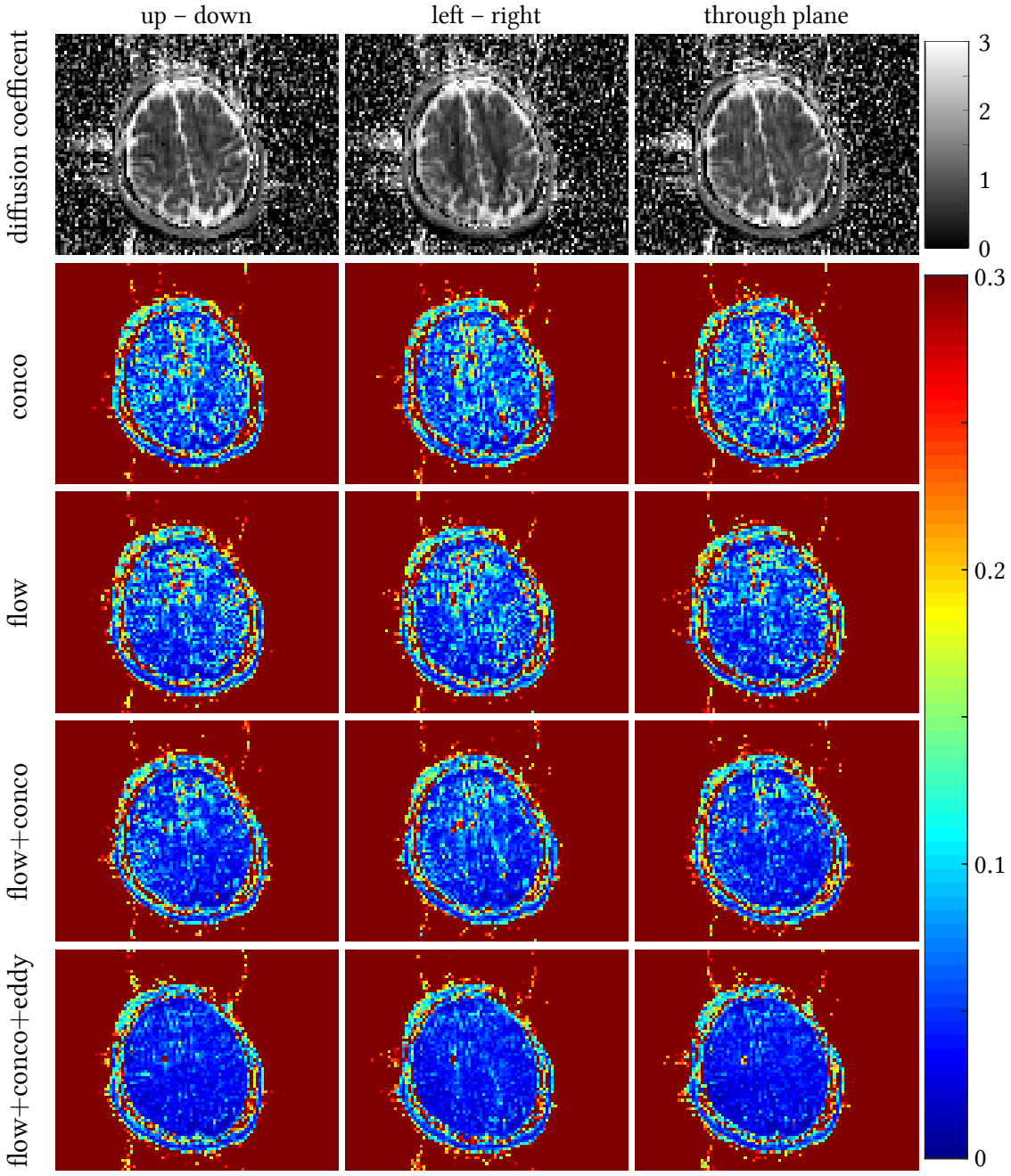

Figure 7.5: CV of the diffusion coefficient for different directions in the brain. The diffusion coefficient (first row, in $\mu m^2/ms$) shows a directional dependence, which is not translated directly to the CV maps.

Table 7.5: Median CV corresponding to the slice shown in figure 7.5

compensation	MD	up–down	left–right	through plane
conco	0.055	0.065	0.066	0.063
flow	0.046	0.056	0.057	0.055
flow+conco	0.038	0.047	0.049	0.044
flow+conco+eddy	0.029	0.035	0.037	0.033

In a second experiment, six different diffusion directions were acquired to determine the diffusion tensor $\underline{\underline{D}}$ and from this the FA. The b-values used were 0, 0.5 and 1.0 ms/µm^2 for no compensation, flow compensation, flow+concomitant field compensation and full compensation.

The images were acquired with TE = 75 ms (for the full compensation this had to be extended to TE = 80 ms), TR = 4000 ms and a single repetition. The other parameters were identical to the first brain measurement series. The slice in figure 7.6 is the same as in figure 7.4.

The arrows point towards areas where differences between the compensation combinations can be seen. A visual inspection shows mostly minor differences between the different compensation schemes. The largest ones can be seen between no compensation and the other three measurements. Without any compensation, a non-zero FA can be detected in areas where there is no anisotropy such as the ventricles. Additionally the FA-values at the brain edges are reduced visibly if a better compensation scheme is used. The largest improvement can, again, be seen between no compensation and the other three measurements.

7.3.2 Abdomen

To show that it is possible to also do flow-compensated IVIM with the proposed sequence, one volunteer's abdomen was scanned in free breathing. The motion artifacts were averaged out by taking the mean value over 5 repetitions. The b-values 0, 0.025, 0.05, 0.1, 0.15, 0.2, 0.25, 0.5 and 0.8 ms/μm^2 were acquired for three diffusion directions to calculate the trace weighted images. The compensation schemes concomitant fields and flow+concomitant fields were used. The other imaging parameters were TE = 65 ms, TR = 4000 ms, FOV = 252 × 350 mm^2, nominal resolution = 3.5 × 3.5 mm^2, slice thickness = 5 mm, partial Fourier factor = 6/8, and bandwidth per pixel = 2380 Hz/pixel.

In figure 7.7, a slice with $b = 0$ is shown on which ROIs drawn. Those ROIs were used to determine the IVIM parameters in different organs. The normalized signal values with the fitted IVIM model can be seen in figure 7.8. The values for D, f and $D^\star$ for the kidney, liver, and spleen are presented in tables 7.6a, 7.6b, and 7.6c.

In all three organs, the use of flow compensation reduces the perfusion fraction. The relative reduction is largest in the kidney, while it is similar in liver and spleen. The lowest perfusion fraction was observed in the spleen. The diffusion coefficient remains mostly constant for both compensation schemes. In the liver, there is a slight increase in D for

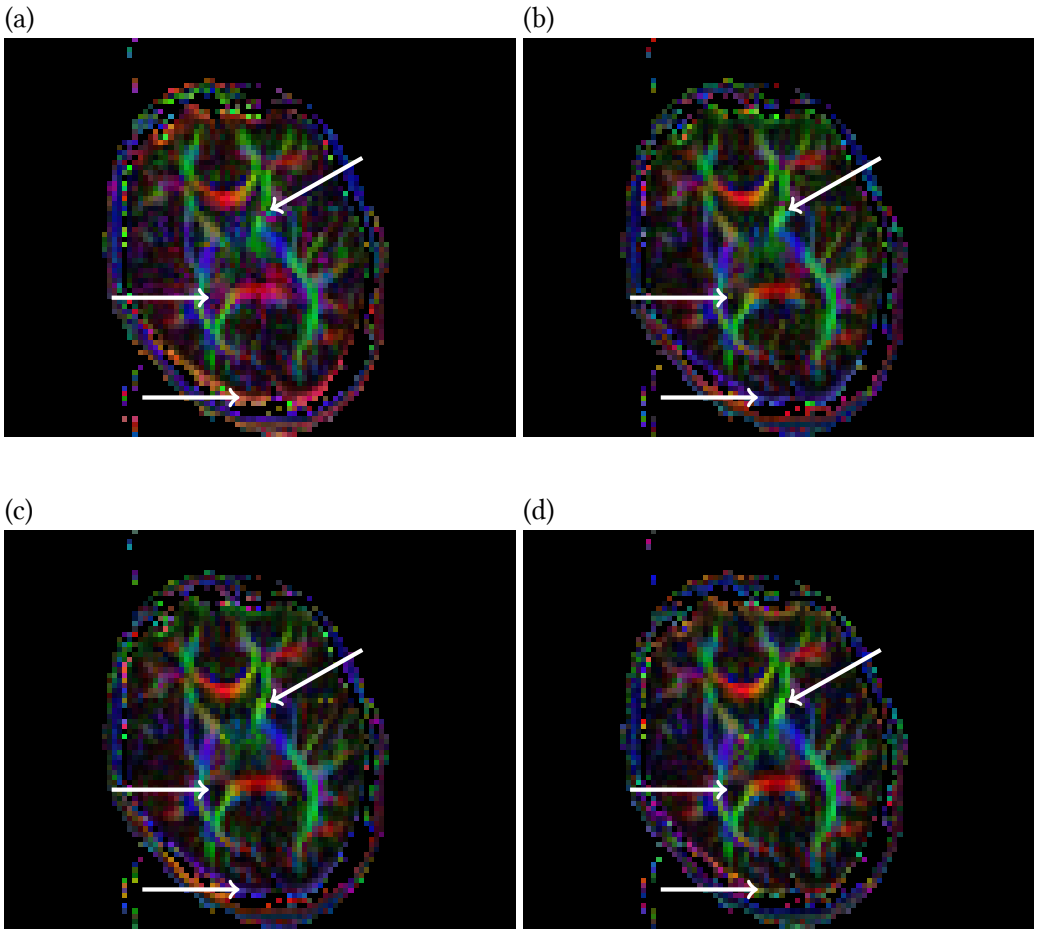

Figure 7.6: FA maps acquired with different compensation combinations. The arrows are pointing to regions with differences among the different maps. The largest differences can be seen between concomitant field compensation (a) and the others. Among flow compensation (b), flow+concomitant field compensation (c) and the full compensation (d), there are only small differences, which are mainly located at the brain edges.

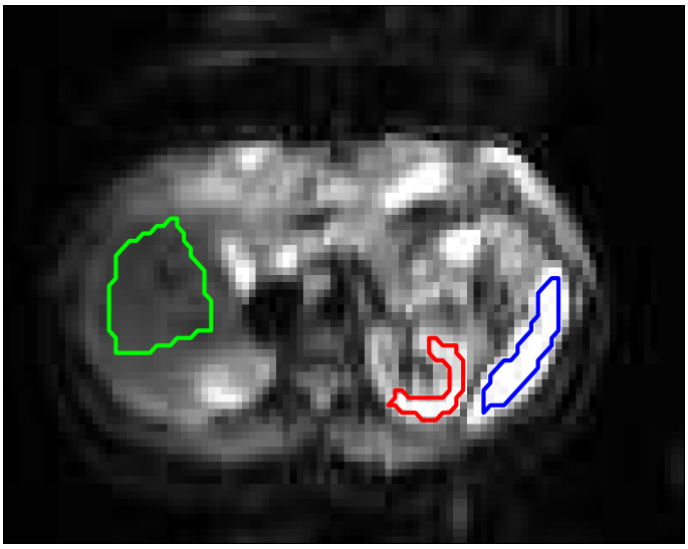

Figure 7.7: Slice chosen for ROI evaluation of IVIM model in the abdomen. The ROIs placed for fitting of the IVIM model in the kidney (red), the liver (green), and the spleen (blue) are shown. The ROIs were drawn on the averaged $b = 0$ image of the sequence with flow+concomitant field compensation.

Table 7.6: IVIM fit results ($\pm$ 95% confidence interval) in the abdomen

(a) Kidney

compensation	$D/(\mu\text{m}^2/\text{ms})$	f	$D^\star/(\mu\text{m}^2/\text{ms})$
conco	1.90 (0.54)	0.28 (0.18)	12 (9)
flow+conco	1.88 (0.18)	0.13 (0.07)	15 (10)

(b) Liver

compensation	$D/(\mu\text{m}^2/\text{ms})$	f	$D^\star/(\mu\text{m}^2/\text{ms})$
conco	1.12 (0.25)	0.31 (0.05)	46 (26)
flow+conco	1.28 (0.10)	0.22 (0.02)	29 (8)

(c) Spleen

compensation	$D/(\mu\text{m}^2/\text{ms})$	f	$D^\star/(\mu\text{m}^2/\text{ms})$
conco	0.78 (0.13)	0.12 (0.05)	19 (16)
flow+conco	0.76 (0.06)	0.08 (0.02)	27 (20)

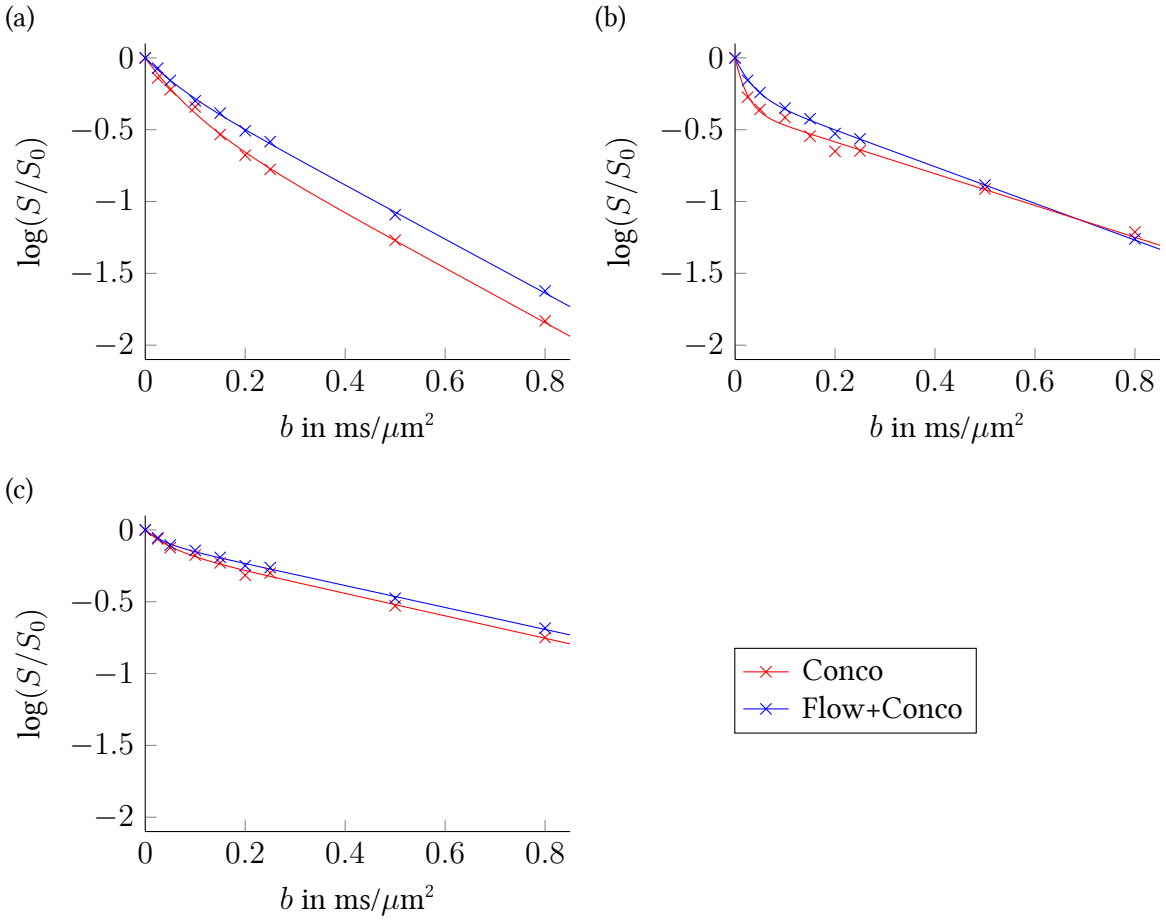

Figure 7.8: IVIM model fits for kidney, liver and spleen. For all organs ((a): kidney, (b): liver, (c): spleen), a bi-exponential fit can be seen. In the kidney and liver, there is a difference in the low b-value regime between flow compensation and no flow compensation. For higher b-values, this difference is lost in the liver. In the spleen, the difference appears at intermediate b-values.

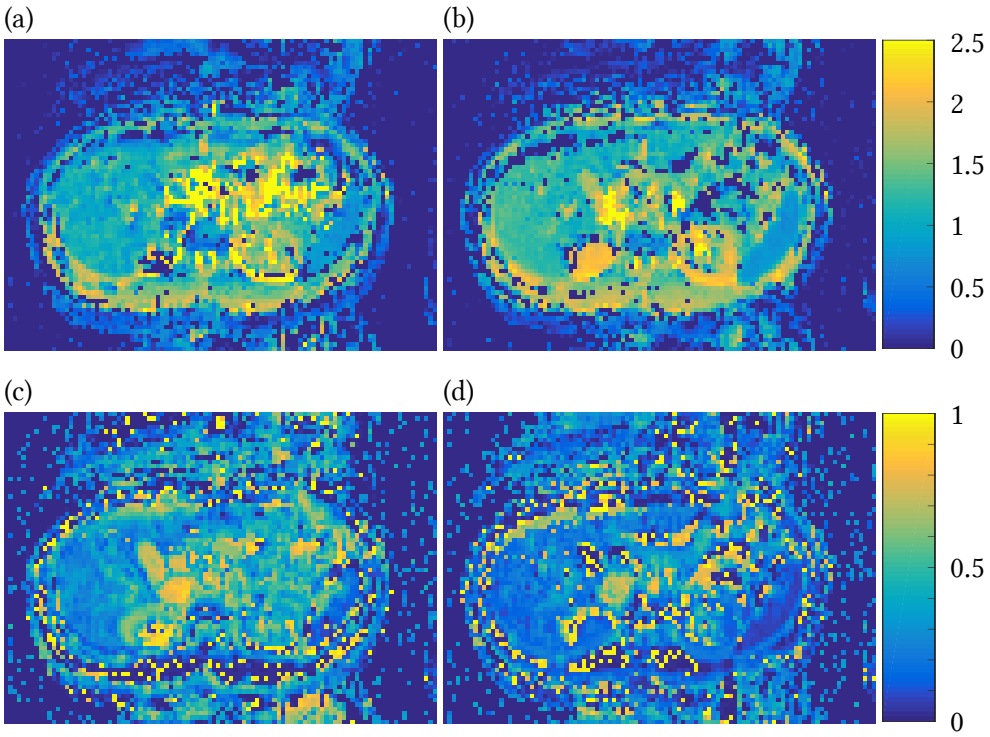

Figure 7.9: IVIM parameter maps of the abdomen. In the upper row, the diffusion coefficient D is shown in $\mu m^2/ms$ for concomitant field compensation ((a) and (c)) and flow+concomitant field compensation ((b) and (d)). The second row shows the perfusion fraction f.

the flow-compensated measurement. This can be seen in the slower signal attenuation for intermediate and large b-values.

It should be noted that in figure 7.8 the normalized signal is plotted, which allows a better comparison between different organs but omits the absolute value. This is smallest for the liver (see figure 7.7) and similar in the kidney and spleen. The values for $D^\star$ show the largest uncertainties in all fits. $D^\star$ is roughly one order of magnitude larger than D.

It is also possible to calculate f and D maps. An exemplary slice is shown in figure 7.9. The parameter maps show the same trends, that were already observed in the ROI analysis. The value of f is lower in the flow-compensated measurement. D remains constant in the spleen and is slightly higher in the liver when flow compensation is used. In the left kidney (on the right side of the image), the mean D-value changes only little, but the distribution seems more even in the flow-compensated measurement.

7.3.3 Prostate

In the prostate, two experiments where performed with one volunteer. The first measurement series included five repetitions to examine the stability of the different gradient schemes. The images were acquired with four b-values (0, 0.25, 0.5 and 1.0 $ms/\mu m^2$) in

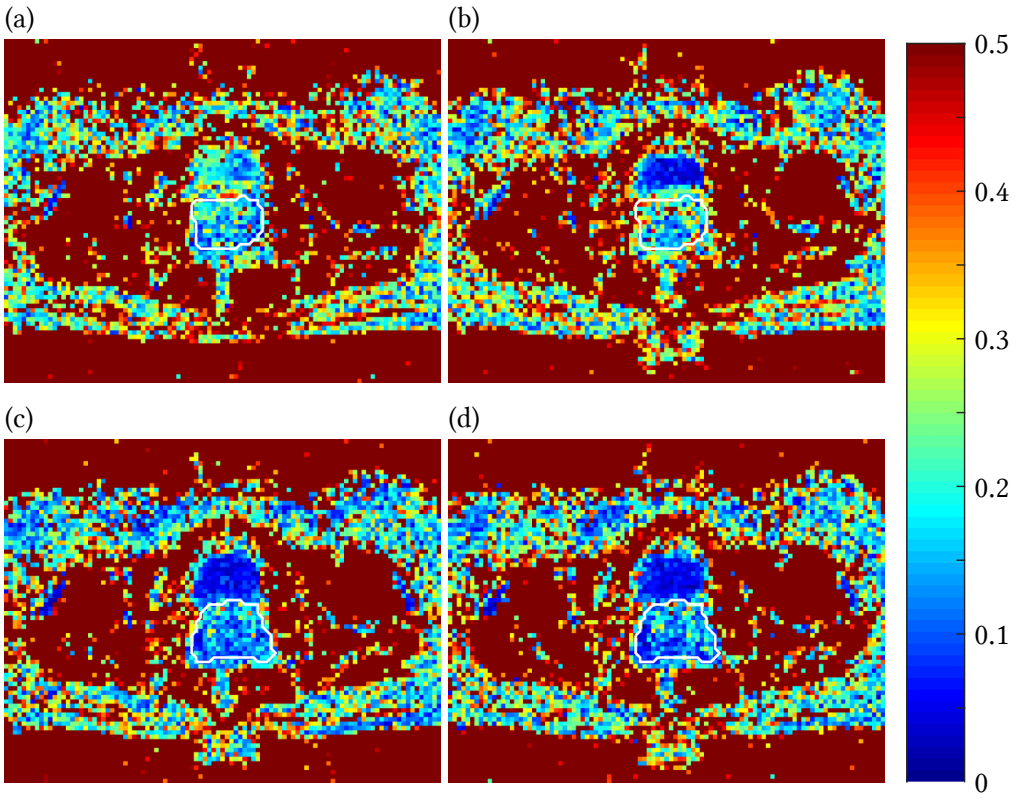

Figure 7.10: CV of MD in the prostate prostate of a healthy volunteer. Different compensation combinations were used ((a): concomitant field, (b): flow, (c): flow+concomitant field, (d): flow+concomitant field+eddy current compensation). The prostate was roughly marked on a corresponding image with $b = 0$ and the outline is shown as a white line. The CV improves the most when flow and concomitant field compensation are combined.

three directions, with TE $= 85$ ms and TR $= 3300$ ms. The FOV was 280×218 mm^2, with a nominal resolution of 2.8×2.8 mm^2 and a slice thickness of 5 mm. Other parameters used were a pixel bandwidth of 2780 Hz/pixel, a Grappa factor of 2 and a partial Fourier factor of $6/8$.

From the three directions, the trace-weighted image was calculated for each b-value and repetition. Afterwards, the MD was determined and the CV of the MD over all repetitions was calculated pixelwise. These maps can be seen in figure 7.10. They show no major difference between only concomitant field (figure 7.10a) and only flow (figure 7.10b) compensation. The same holds true for the maps for flow+concomitant field (figure 7.10c) and flow+concomitant field+eddy current compensation. An improvement can be seen when going from the first to the second pair. This is confirmed by looking at the mean value $\pm$ standard deviation over the ROIs shown in figure 7.10. In this analysis, the mean CV for

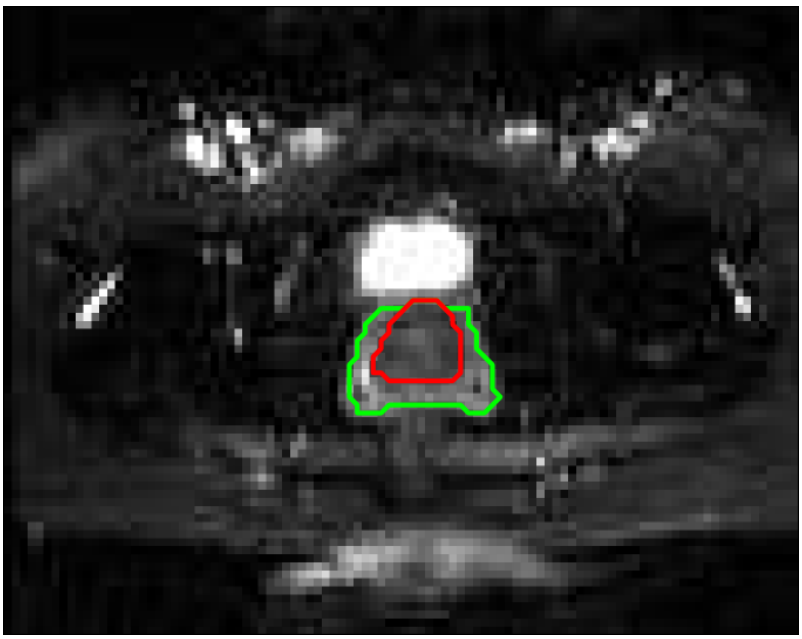

Figure 7.11: Slice chosen for ROI evaluation of the IVIM model in the prostate of a healthy volunteer. The red ROI encompasses the central gland of the prostate, while the green one was drawn around the peripheral zone. The green ROI does not include the red one.

concomitant field compensation alone is with 0.21 ± 0.45 smaller than for only flow compensation 0.26 ± 0.38, although the standard deviations are both rather large. The values for the measurements with flow+concomitant field (0.14 ± 0.08) and with flow+concomitant field+eddy current (0.15 ± 0.12) compensation are very close together.

The second measurement series was used to determine IVIM parameters. Therefore the b-values 0, 0.01, 0.02, 0.03, 0.04, 0.05, 0.1, 0.5 and 1.0 $\mathrm{ms}/\mu\mathrm{m}^2$ were used with the four different compensation combinations: no compensation, concomitant field, flow+concomitant field, and flow+concomitant field+eddy currents so that two measurements were without and two were with flow compensation. The other imaging parameters were the same as in the other prostate measurement series.

For ROI analysis, two ROIs were chosen (see figure 7.11), one covering the peripheral zone and the other covering the central gland. The resulting normalized signal vs. b curves are shown in figure 7.12. The different measurements can be distinguished more easily in the graphs showing a zoom on low b-values. The fitting results (with 95% confidence interval) are shown in table 7.7a for the central gland and in table 7.7b for the peripheral zone.

In the central gland, the perfusion effect is rather small and the use of flow compensation shows only minor effects. In the peripheral zone, this effect is considerably larger. Without flow compensation, a steep signal drop can be observed in the peripheral zone for low b-values. This is no longer present when flow compensation is used. The measurements without any compensation and the one with only concomitant field compensation yield

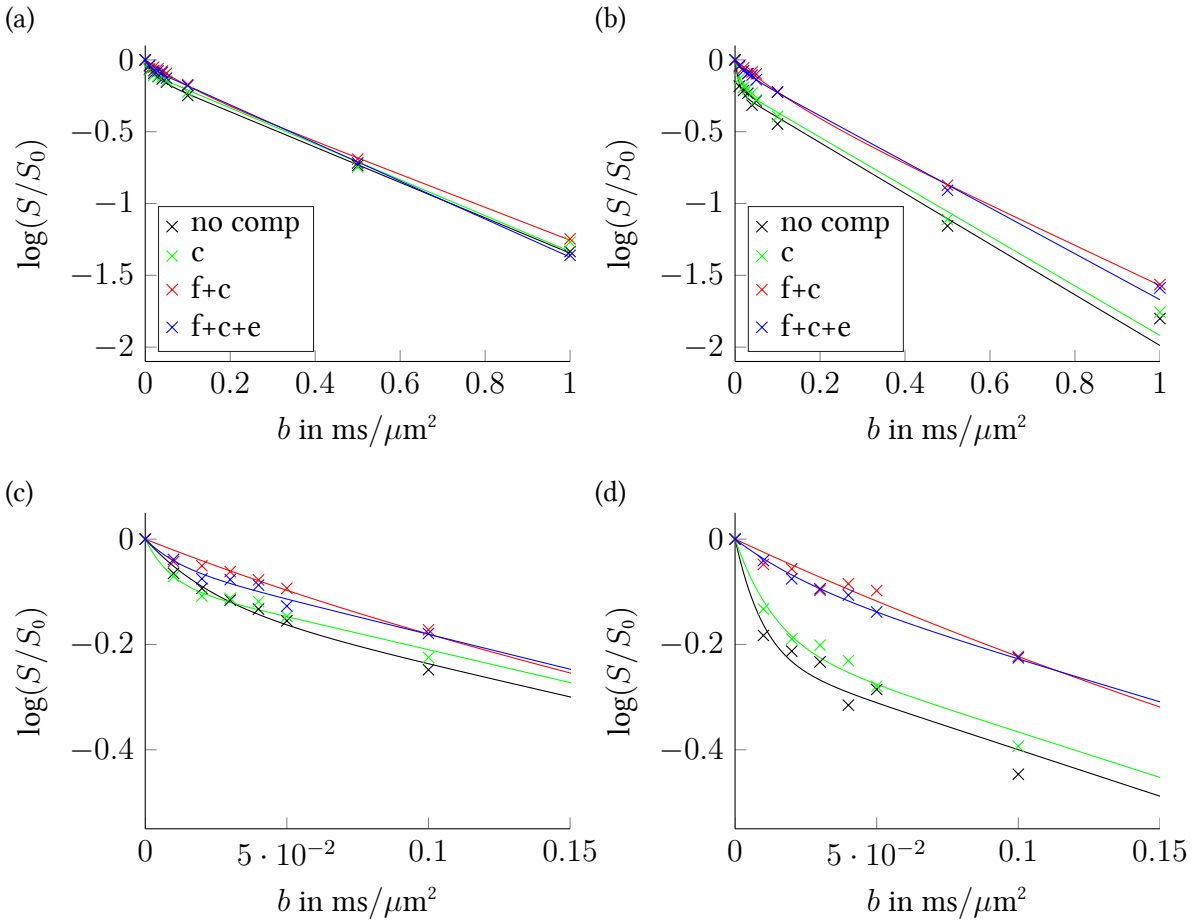

Figure 7.12: IVIM model fits for the prostate of a healthy volunteer. In the central gland ((a) and (c)), the IVIM effect is small and only a slight effect of flow compensation (noted with f) could be observed. In the peripheral zone ((b) and (d)), the effect is noticeably higher. The second row allows a closer look at the low b-value range. There are only small changes if concomitant field (noted with c) or eddy current (noted with e) compensation is used. (c) and (d) are close ups on small b-values of (a) and (b) respectively.

Table 7.7: IVIM fit results (± 95% confidence interval) in the prostate of a healthy volunteer.

(a) Central Gland

compensation	$D/(\mu\text{m}^2/\text{ms})$	f	$D^\star/(\mu\text{m}^2/\text{ms})$
no comp	1.23 (0.08)	0.11 (0.03)	45 (21)
conco	1.25 (0.10)	0.08 (0.02)	120 (144)
flow+conco	1.15 (0.20)	0.11 (0.12)	10 (13)
flow+conco+eddy	1.33 (0.07)	0.05 (0.02)	87 (107)

(b) Peripheral Zone

compensation	$D/(\mu\text{m}^2/\text{ms})$	f	$D^\star/(\mu\text{m}^2/\text{ms})$
no comp	1.77 (0.33)	0.20 (0.05)	114 (107)
conco	1.73 (0.24)	0.18 (0.04)	80 (61)
flow+conco	1.39 (0.49)	0.16 (0.29)	8 (12)
flow+conco+eddy	1.60 (0.12)	0.07 (0.04)	39 (46)

similar results for D and f in each ROI. In the central gland, they change only a little when using the full compensation. In the peripheral zone, both values are reduced, whereas the reduction is relatively larger for the perfusion fraction. In the case of flow+concomitant field compensation, the bi-exponential model does not seem to be suitable to describe the data very well, as the uncertainty is larger than the value itself for f and $D^\star$ in both ROIs.

In addition to the ROI analysis, voxelwise maps were calculated. The diffusion coefficient D is shown in figure 7.13 and the perfusion fraction f in figure 7.13. For these images, the parameters inside the union of the ROIs in figure 7.11 were superimposed in color on a gray-scale magnitude image with $b = 0$.

The D maps show similar features to the ROI analysis such as a higher value in the peripheral zone. This is at least the case in the left and right part of the peripheral zone, which was marked in figure 7.11. In the posterior area, there is only a thin area with a larger D for no compensation and only concomitant field compensation, which is not seen in the other two measurements. In those measurements, D has the same value as in the central gland. Additionally, D seems to be smaller in the peripheral zone for the flow+concomitant field and fully compensated sequences compared to the no and the concomitant field compensation sequences.

In the f maps (figure 7.14),the distinction between peripheral zone and central gland is not possible, although the areas with higher perfusion are mostly located in the peripheral zone for both measurements without flow compensation. The other two measurements do not show these areas.

In addition to the healthy volunteer, three prostate cancer patients were imaged with the same protocol, except for slightly longer ramp times and the b-values (0.05, 0.15, 0.5 and 1.0 $\mu\text{m}^2/\text{ms}$). For the evaluation, ROIs were placed in suspicious lesions on the standard MRI images (T_2-weighted and diffusion images), that were afterwards biopsied and proven

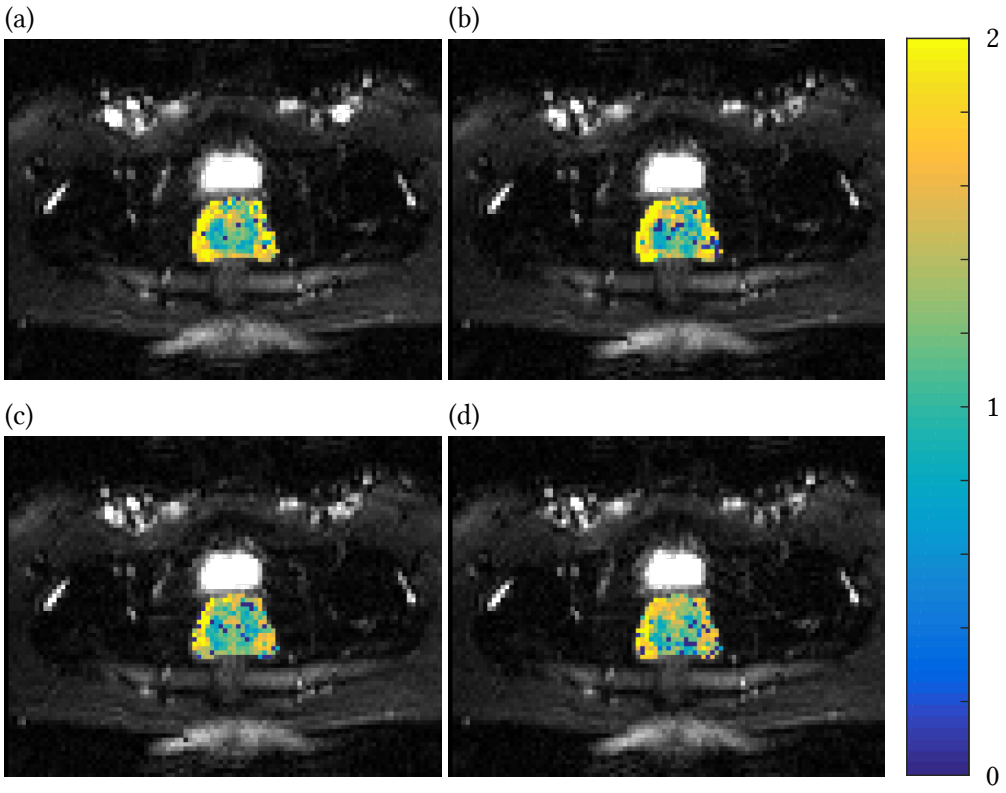

Figure 7.13: Diffusion coefficient (D) maps of the prostate of a healthy volunteer using IVIM. In the central gland all maps look similar. In the peripheral zone D is higher in the measurements without any (a) and with concomitant field compensation alone (b) than for one with flow+concomitant field (c) and the flow+concomitant field+ eddy curren -compensation. D is given in $\mu m^2/ms$

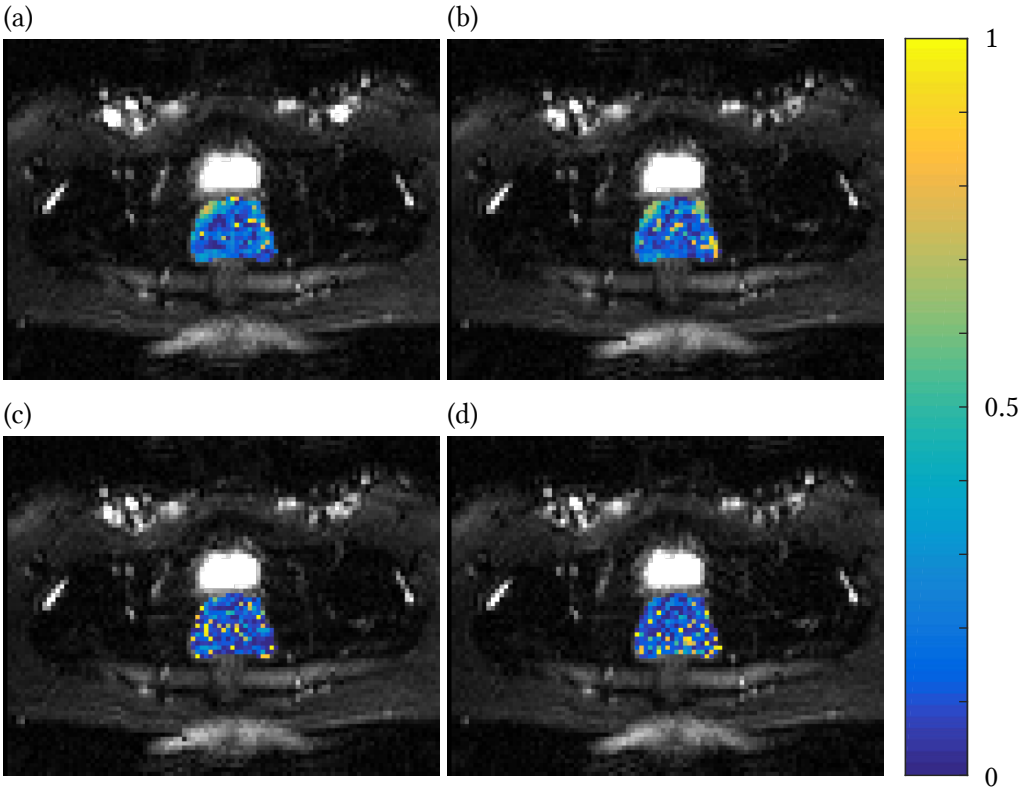

Figure 7.14: Perfusion fraction f maps of the prostate of a healthy volunteer using IVIM. The measurements without any (a) and with only concomitant field (b) compensation show relatively high f-values in the anterior part of the peripheral zone, which are not present in the flow+concomitant field (c) and the flow+concomitant field+eddy current (d) compensated measurements. The latter two show more pixels with extremely high f, scattered noise-like over the prostate.

Table 7.8: IVIM fit results (± 95% confidence interval) in the prostate of a patient (Gl.3+3).

(a) Tumor

compensation	$D/(\mu m^2/ms)$	f	$D^\star/(\mu m^2/ms)$
conco	0.78 (0.58)	0.24 (0.32)	10 (20)
flow	0.94 (0.46)	0.17 (0.28)	9 (18)
flow+conco	1.11 (0.26)	0.07 (0.11)	33 (154)

(b) Reference region

compensation	$D/(\mu m^2/ms)$	f	$D^\star/(\mu m^2/ms)$
conco	1.17 (0.47)	0.31 (0.32)	5 (4)
flow	0.48 (0.69)	0.74 (0.69)	3 (1)
flow+conco	0.42 (6.13)	0.74 (2.18)	3 (6)

Table 7.9: IVIM fit results (± 95% confidence interval) in the prostate of a patient (Gl.3+4).

(a) Tumor

compensation	$D/(\mu m^2/ms)$	f	$D^\star/(\mu m^2/ms)$
conco	0.86 (0.26)	0.21 (0.18)	5 (4)
flow	1.28 (0.30)	0.05 (0.26)	5 (20)
flow+conco	0.002 (4.40)	0.77 (1.51)	2 (3)

(b) Reference region

compensation	$D/(\mu m^2/ms)$	f	$D^\star/(\mu m^2/ms)$
conco	1.68 (0.06)	0.11 (0.03)	18 (8)
flow	1.60 (0.07)	0.30 (0.07)	3.6 (0.3)
flow+conco	1.46 (1.68)	0.37 (1.29)	4 (7)

to be cancerous. For comparison, ROIs in tissue without proven cancer were used. The ROIs were placed in the same slice.

Slices with MR visible lesions are shown in figures 7.15, 7.16 and 7.17. The results of the IVIM fits are listed in tables 7.8, 7.9 and 7.10.

The lesions with a Gleason score $3+3$ and $3+5$ were located in the central gland, while the Gleason $3+4$ lesion was located in the peripheral zone. The $3+3$ and $3+4$ lesions showed a similar behavior in the IVIM curves when compared with the non cancerous tissue. There is in both cases a clear difference between the curves for healthy and cancerous tissue. The curves differ for higher b-values, while they are very similar for the small b-values. Differences among the compensation combinations could be observed in neither of the ROIs examined for those two patients. This is in contrast to the healthy volunteer, where an effect of flow compensation was observed in the peripheral zone. The $3+5$ lesion shows a smaller difference between the two ROIs.

Even though the curves are clearly separated, this cannot be said about the fitting results. The values show large uncertainties, which are in many cases larger than the values itself.

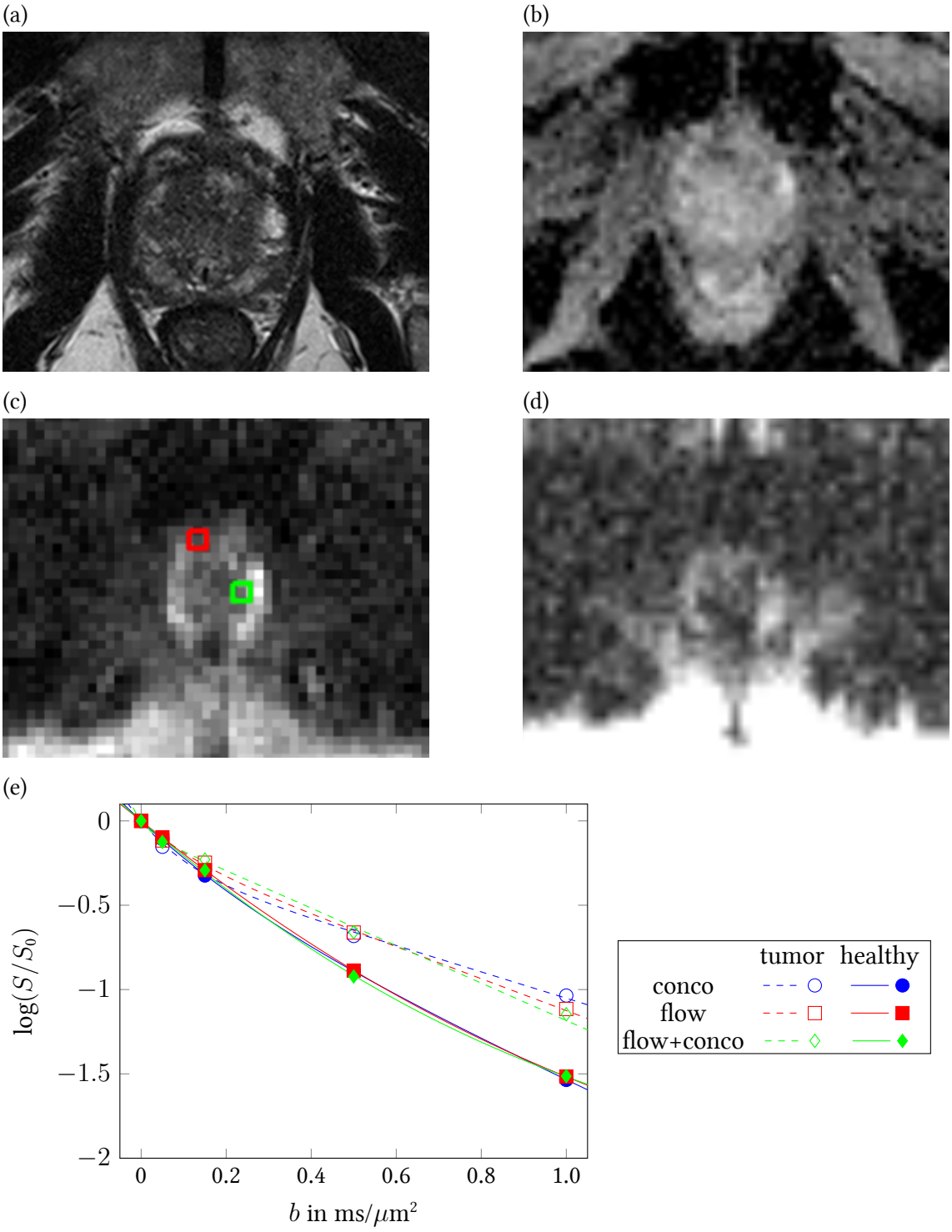

Figure 7.15: Prostate cancer patient with Gleason score 3+3. (a) T_2-weighted image from clinical protocol. (b) ADC map calculated from clinical diffusion sequence. (c) Image with $b = 0$, used for ROI placement. The red ROI was placed in the tumor, the green one in tissue without proven cancer. (d) Image with $b = 1.0\,\mathrm{ms}/\mu\mathrm{m}^2$. (e) IVIM curves for both ROIs. Reference and tumorous tissue can be clearly separated, but there is no visual difference between flow and no flow compensation.

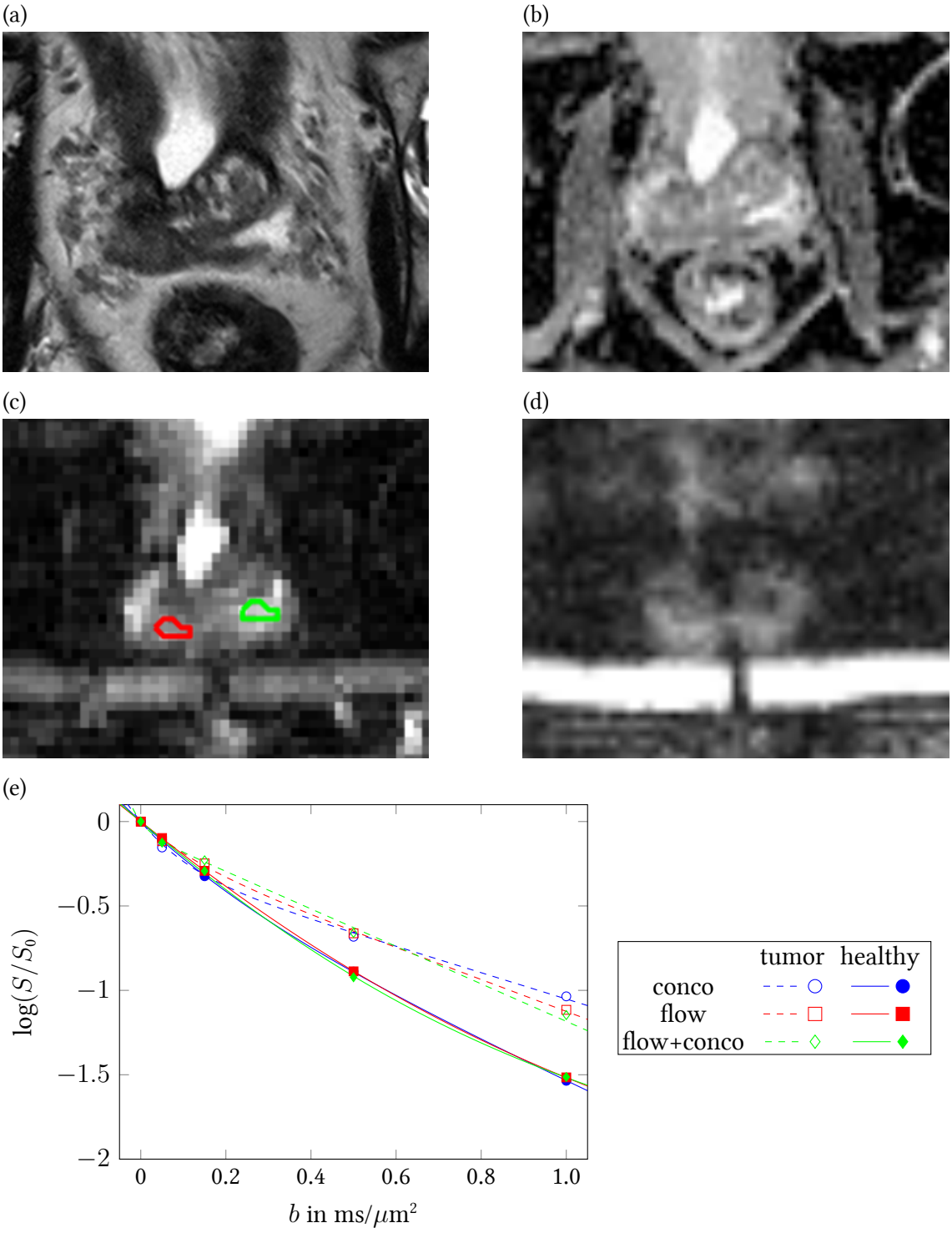

Figure 7.16: Prostate cancer patient with Gleason score 3+4. (a) T_2-weighted image from clinical protocol. (b) ADC map calculated from clinical diffusion sequence. (c) Image with $b = 0$, used for ROI placement. The red ROI was placed in the tumor, the green one in tissue without proven cancer. (d) Image with $b = 1.0\,\mathrm{ms/\mu m^2}$. (e) IVIM curves for both ROIs. Reference and tumorous tissue can be clearly separated, but there is no visual difference between flow and no flow compensation.

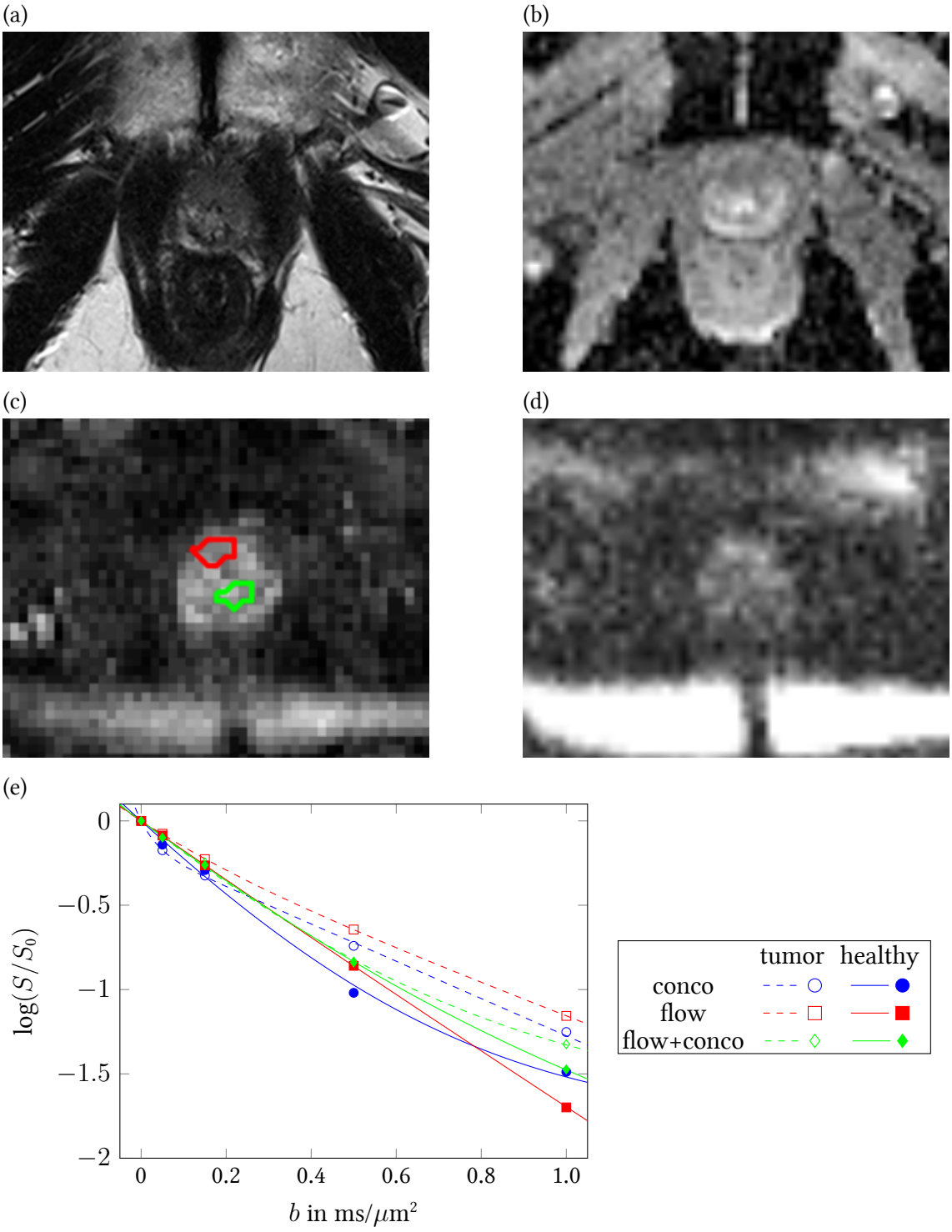

Figure 7.17: Prostate cancer patient with Gleason score 3+5. (a) T_2-weighted image from clinical protocol. (b) ADC map calculated from clinical diffusion sequence. (c) Image with $b = 0$, used for ROI placement. The red ROI was placed in the tumor, the green one in tissue without proven cancer. (d) Image with $b = 1.0\,\mathrm{ms}/\mu\mathrm{m}^2$. (e) IVIM curves for both ROIs. Reference and tumorous tissue are slightly separated. There is no systematic difference between flow and no flow compensation in the tumor.

Table 7.10: IVIM fit results (± 95% confidence interval) in the prostate of a patient (Gl.3+5).

(a) Tumor

compensation	$D/(\mu m^2/ms)$	f	$D^\star/(\mu m^2/ms)$
conco	1.11 (0.17)	0.16 (0.07)	26 (29)
flow	0.97 (0.16)	0.17 (0.13)	5 (3)
flow+conco	0.05 (15.54)	0.80 (4.33)	2 (11)

(b) Reference Region

compensation	$D/(\mu m^2/ms)$	f	$D^\star/(\mu m^2/ms)$
conco	0.00[a]	0.84 (0.12)	3 (1)
flow	1.63 (0.53)	0.08 (0.77)	3 (11)
flow+conco	0.47 (5.20)	0.76 (2.00)	2 (4)

[a] no confidence interval can be given, as the value was limited by the fitting constraints

8 Discussion

This work aimed at improving the determination of microscopic tissue parameters such as μFA or tissue perfusion, by reducing artifacts in different diffusion weighted MRI techniques. Therefore, two sequences were developed. The first one was a DDE sequence, which was modified to compensate for eddy current artifacts. The improvements were demonstrated in phantom experiments and verified in vivo. The in vivo measurements of the μFA mainly benefited from reduced falsely elevated values in areas with little to no anisotropy. The second one was a SDE sequence. In previous works, SDE sequences were compensated for flow or eddy current artifacts individually. Here, it was shown that it is also possible to achieve these compensations simultaneously while additionally compensating for concomitant fields. This was shown in simulations and phantom experiments. The use of these compensations allowed a more accurate determination of the FA in the brain and more stable IVIM measurements in the abdomen and prostate.

8.1 Eddy-Current-Compensated Double Diffusion Encoding

8.1.1 General Remarks

The eddy current compensation for the DDE sequence was achieved by using the TRSE [Hei00, RHWW03] gradient scheme for each diffusion encoding individually. This reduced the need for post processing methods for eddy current compensation that require the acquisition of additional images [BKKT04, LBF15] and/or an image registration [HM96, MMK$^+$10]. The acquisition of additional images requires more measurement time, which is not desired. Registration approaches suffer from the problem that they cannot reduce image blurring from time dependent eddy currents and have to deal with the changing image contrasts for different diffusion encoding strengths [Hor99]. Another problem with the affine registration approaches is that they perform worse at correcting the eddy current artifacts than the sequence design approaches [NDC$^+$11]. For the best possible results, it might be necessary to combine an eddy current compensated sequence design with an appropriate post processing algorithm.

All eddy current compensation was performed under the assumption of a single decay time. This time constant was chosen to minimize the eddy current artifacts, although it was not possible to compensate for eddy currents completely. This can be seen by the difference between the fully compensated measurements and the baseline measurements with only one diffusion direction. One way to improve this might be to use an approach that compensates partly for two decay times [Fin10]. A drawback of this approach is the longer TE needed. For in vivo measurements, the use of the proposed sequence already yielded an

approximately 20 ms longer TE. If this is prolonged even further, the measurements might get unfeasible for reasonable b-values. With short t_m, it might be more reasonable to use the approach for two decay times.

It should be noted that the definition of t_m used in this work differs from the definition used in most publications. Here, it was defined as the time from the end of the first diffusion encoding to the beginning of the second encoding, while it is normally the time from the beginning of the rephasing gradient of the first encoding to the start of the dephasing gradient of the second encoding [SJA+16]. Consequently, in the u/u sequence the t_m given here is shorter by one total gradient time than in the standard definition. The reason for the different definition lies in the sequence schemes of the other three compensation combinations. The lowest achievable t_m is limited because of the varying gradient pulse durations and the RF pulses in between. Additionally, the diffusion times that were used for comparison of different encoding schemes (in DDE and SDE) were the total durations of the individual encodings, labeled T_D. These definitions lead to the effect that the sum of both T_D and t_m gives the total time needed for both diffusion encoding. The disadvantage of the t_m definition is that the theoretical zero mixing time limit, with overlapping gradient pulses of the two encodings, is different than the $t_m = 0$ used here.

Another definition, which varies in the literature, is when $\boldsymbol{q_1}$ and $\boldsymbol{q_2}$ are considered to be parallel and when they are seen as antiparallel. In many previous publications, it is not clearly stated which definition the authors used [JB11, SBS+12], but they mostly followed [Mit95]. The authors who do mention it also followed this conventions [KF08, Fin11]. All the aforementioned studies used the u/u sequence and considered $\boldsymbol{q_1}$ and $\boldsymbol{q_2}$ as parallel if the two innermost gradients are parallel. In this case, parallel encodings are achieved if the rephasing gradient of the first encoding and the dephasing gradient of the second encoding are parallel. A recent consensus of nomenclature in DDE experiments [SJA+16] stated that it is more helpful to define parallel encodings for the effective gradient scheme, which is without RF pulses and adjusted gradient directions. In this case, two encodings are considered parallel if the dephasing gradients of each encoding are parallel. This is the opposite definition of the commonly used one and the one used in this work. These two different definitions explain the opposite sign in $Q = \mathrm{tr}(\underline{\underline{Q}})$ measured here and predicted in [JB11]. There, the theoretical considerations and simulations predicted a negative definite $\underline{\underline{Q}}$, while here clearly positive values were measured. The definition for $\underline{\underline{Q}}$ in the signal equation 5.15 looks the same as in [JB11], but the additional minus that pops up by the redefinition of parallel q-vectors is absorbed in the definition of $\underline{\underline{Q}}$.

8.1.2 Simulations and Phantom Experiments

The diffusion phantom experiments show a slight decrease in Q with longer t_m for the fiber area. This was more prominent in the Monte Carlo simulations. The decrease is in accordance with expectation [KF09, Jes12] and measurements [SOBC09, SC11a]. In these publications, the signal difference between parallel, antiparallel and orthogonal measurements is used for estimations of pore size and anisotropy, without calculating $\underline{\underline{Q}}$ explicitly, with the exception of [Jes12]. It was shown that $\underline{\underline{Q}}$ and $\underline{\underline{D}}$ bear all information on com-

partment size that can be determined from fits with terms up to the order of q^2 (that is b) [JB11]. In the agarose gel, where the diffusion is mainly free [WS70], the correlation tensor was basically zero, as expected [JB11]. The one value in agar gel close to the value inside the fiber area can most likely be attributed to noise. The low diffusion encoding ($q = 0.05\,\mu m^{-1}$) leads only to a small signal difference and thus to a high sensitivity to noise.

The Monte Carlo simulations show a strong dependence of Q on t_m for short mixing times. Additionally the T_D behavior shows differences between the two geometries. This might be explained by the different times needed to reach the long time limit for both geometries. This fact is best visible in the dependence on t_m. For the plates, the long mixing time limit($Q = 0$) is reached for $t_m \gtrsim 15\,ms$. For the circle, the long time limit is not yet reached for 30 ms. In general, the simulations for Q done here show the same trends as in [JB11] and [KF09].

An important result of the simulations for μFA is that a microscopic anisotropy can be measured for the circle, although none is present, if the long mixing time limit is not met. In this regime, there is still a cos θ dependence of the signal which is due to the restrictions [Mit95, KF08] and leads also to differences between parallel and perpendicular encodings. In the limit of low q-values and long diffusion times, the use of parallel and antiparallel diffusion encodings should eliminate the difference and thus the apparent μFA [Mit95, KF08]. This was theoretically shown in descriptions of DDE parameters where the assumption of long diffusion times has been loosened [ÖB08], but low q-values were still assumed. In another work, higher q-values were considered in the zero and long mixing time limit [Öza09] leading to the same result. In simulations where none of the conditions were met, deviations were found for the angular dependence of the signal [KF09], which would reduce, but not eliminate, the false μFA. In the simulations performed here also none of the assumptions were met, which might explain the false μFA, although parallel and antiparallel q-vectors were used.

For the parallel plates no t_m dependence of the μFA was found. Therefore, the diffusion time dependence can be explained by the following considerations. For short diffusion times only the particles close to the boundaries are effected by these while most diffuse freely. The longer the diffusion time gets the more particles are affected by the boundaries and therefore experience the anisotropy [MSSLD92, MSS93]. Since the total anisotropy is derived from an average over all particles, it grows with longer diffusion times until the particles probe the whole volume and the μFA reaches the maximal value. The simulations showed that this process is slightly faster for the μFA than for the FA.

In the diffusion phantom, a small dependence of μFA on t_m was measured. This difference to the simulations might be explained by the differences in the setup, as, for example, the simulations assumed infinitely short gradient pulses. In the measurements, the gradient pulse durations were effectively just a little less than $T_D/2$. The main point of the simulations was to show that the existence of isotropic boundaries can lead to an apparent μFA if the long mixing time limit is not met and that the correlation tensor is a good measure to see if the long mixing time limit is reached.

The overestimation of the μFA for small q-values in the phantom measurements is in accordance with [JLSD13] where simulations showed that the determination of ϵ and there-

fore also μFA depends on many parameters such as the pore size and q-value. It can happen that ϵ is overestimated for small q-values. For a very large ϵ, the μFA goes to 3/2, as can easily seen from the normalization (equation 5.13).

8.1.3 In Vivo Measurements

The DDE brain measurements show clearly elevated μFA values in gray matter, which are reduced if the compensated sequence is used. This is visible in the calculated maps as well as in the averages over the whole brain. For the white matter, however, no systematical changes were observed. The μFA-values reported here for white matter lie below the ones in [SLvW+15], although it must be considered that the latter used the q-vector magic-angle spinning (qMAS) technique. In qMAS, constantly changing diffusion gradients are employed to determine the microscopic anisotropy [ELT13, LSE+14]. This method assumes no exchange between different pores, a time-independent diffusion tensor and a Gaussian phase distribution in each pore. If all assumptions are met, the isotropic DDE scheme and qMAS should give the same μFA-values [JLSD14a], but they report values for specific white matter regions between 0.93 ± 0.01 and 1.02 ± 0.02, which is considerably higher than the 0.72-0.79 measured in this work. One explanation for the difference might be the approximately three times longer diffusion time used in [SLvW+15]. This would allow the particles to probe the anisotropy better as was also seen as a result in the simulations. Another difference is that in this study the values were averaged over the whole brain with a rather simple white matter mask. This also included voxels that were affected by partial volume effects and therefore reduced the average. The analysis of single ROIs yielded higher anisotropies, which were still smaller than in [SLvW+15].

Other studies measuring the anisotropy in the human brain with DDE [LBF15, LF15] used a different directional scheme yielding a different anisotropy parameter labeled microscopic anisotropy (MA) [LKF10]. The MA ranges from 0 to 1, but is not identical to the μFA [LBF15]. Most white matter ROIs show MA values between 0.8 and 0.9, with the lowest value 0.629 ± 0.046 and the highest 0.947 ± 0.017 [LBF15], so the reported values have a similar range as the μFA measured here. In their gray matter ROIs the MA is between 0.464 ± 0.064 and 0.624 ± 0.079 which is in the same range as the μFA measured in section 6.3, which was on average 0.53 ± 0.19.

The μFA values have to be interpreted carefully as was shown in the simulations. Measurements which do not reach the long time limit can lead to a falsely elevated μFA. With the timing used here, the long time limit was not reached, which can be seen by the non-zero correlation tensor. The falsely heightened μFA is maybe more pronounced in the in vivo measurements than in the simulations or in [LBF15, LF15] because no antiparallel measurements were included here, which reduce the effects of a shorter t_m [ÖB08, KF09, Öza09]. Additionally, it should be mentioned that in [LBF15, LF15] no cortical gray matter was looked at. This was done recently in [LF16] where they observed a MA of 0.2 ± 0.1, while in this work the whole brain gray matter was looked at.

In the MA studies, similar time parameters were used, but the applied q-values were slightly lower with $q \approx 0.16\,\mu\text{m}^{-1}$, compared to the 0.193 and $0.233\,\mu\text{m}^{-1}$ used here. The q-values were even higher in ex vivo studies, $q = 0.28\,\mu\text{m}^{-1}$ for fixed vervet monkey

brain [JLSD13] and $q = 0.314\,\mu\text{m}^{-1}$ for fixed rat brain [SBS+12]. The values given here are adjusted from the papers to fit the applied definitions. All q-values reported here are reported for a single encoding. One assumption for the μFA measurements is that terms of order q^6 (that is b^3) and higher in the signal expansion are negligible. The role of these terms is difficult to assess because they are not known a priori. For typical diffusion and kurtosis values in the human brain, it was estimated that b-values up to $2.0\,\text{ms}/\mu\text{m}^2$ should lead to an accuracy within 20 % (for fits up to the order of b^2) [JH10]. A similar approach could be applied here showing that the b-values used here ($2 \cdot 0.5\,\text{ms}/\mu\text{m}^2$) should be reasonably low.

In this work, the DDE measurements were only optimized for eddy current artifacts. It might prove useful to consider other sources of artifacts as well, such as concomitant fields or susceptibility differences. In the optimization for the SDE sequence, it was shown here, that the TRSE sequence can additionally be compensated for concomitant fields. This would have improved the measurements with the grid phantom but most likely not have changed the in vivo results considerably as the magnitude brain images showed no such artifacts. On the other hand, it would have increased TE and therefore worsened the SNR.

Another source of falsely heightened μFA-values, besides eddy currents, can be susceptibility differences in the tissue [SC11b]. These lead to internal gradients [Hur98, ZP07] which can induce an apparent anisotropy. One approach to minimize these artifacts in SDE measurements is the use of a bipolar gradient scheme and/or the use of additional refocusing RF pulses [CHSM89, ZP07]. Some of the proposed solutions were also included in DDE measurements [KF08, SC11b] and can possibly be implemented for an eddy-current-compensated sequence.

The proposed eddy current compensation could also be used for other DDE applications than μFA measurements. It might prove not feasible for pore size estimations, as they are ideally done in the zero mixing time limit [Mit95, ÖB08, SOBC09] leading to overlapping gradients. This not achievable with the current approach because of the two dephasing and two rephasing gradients for each diffusion encoding. The different durations of the dephasing and rephasing gradient pulses and the resulting different position of the RF pulses hinder a large gradient overlap. It is thus necessary to apply the diffusion encodings consecutively, without overlapping gradients. This would prolong the effective mixing time and decrease the signal modulation [KF08]. For exchange measurements with filter exchange imaging (FEXI) [LNL+11, NLvW+13], it might prove more fruitful to use the eddy current compensated diffusion encoding. This method often uses a stimulated echo sequence as even longer t_m are required. The eddy current compensated DDE sequence could easily be modified to use a stimulated echo. As the gradient timings for each encoding were calculated individually, the needed 90° RF pulses could be included between the two encodings.

8.2 Artifact-Reduced Single Diffusion Encoding

8.2.1 Optimization

The main goal of the sequence optimization for the SDE sequence was to find a flow-compensated one that also allowed for concomitant field and eddy current compensation, but, for completeness, all combinations of compensations were looked at.

One limitation in the optimization is the assumption of rectangular gradient pulses with constant amplitude. In other diffusion encoding sequences, these assumptions were not met. In [WSL15], trapezoidal gradient pulses with different amplitudes were applied to get a flow-compensated diffusion encoding with additional concomitant field compensation. In other works, oscillating gradients were used to probe the behavior for short diffusion times [DPG03, PDG06], whereupon they can be chosen to be flow compensated or not [GXC+10, Wet13]. Although, these sequences have their applications, it was shown that for a given b-value the shortest TE can be achieved with trapezoidal gradient pulses with mostly maximal amplitude [AWE17]. This was achieved by minimizing TE for a given b-value. The gradient amplitude for each time point was optimized without any restriction on the gradient form, aside from hardware constraints, namely the maximal gradient amplitude and slew rate. Despite the difference in the optimization setup, finding minimal TE for given b-value against finding maximal b-value for given TE and partially different constraints, it is a good indication that trapezoidal gradients achieve the optimal result.

The use of rectangular gradients in the optimization simplifies the equations, without changing the results, as the ramps only cause minor corrections as can be seen in the theory sections (3.4, 3.5, 4.2 and 4.4).

In many studies where flow compensation is implemented, the used sequence is $+-|+-$ [DRTW02, GBK07, AKW+16]. In the simulations performed here, this is the sequence with the highest b-value for flow-compensated diffusion MRI with additional concomitant field compensation. In [AWE17], the best result shown for flow compensation is basically $+-+|-$. A reason for this difference can be seen in the longer time they allocated for the readout with over 20 ms compared to the 10 ms used here. In the actual measurements, this difference should not be present as the used sequence $+-+|-+$ also allows for both other schemes to be realized. If only flow is compensated for, the sequence with the highest b-value can contain two RF pulses, which was the case here for the intermediate and long TE. The difference is only minor and might be canceled out by the higher sensitivity to imperfections of the refocusing RF pulse.

For the measurements in [AWE17], an additional concomitant field correction is needed. With the approach presented here, this is not necessary and the b-value is only reduced marginally. The reduction could be slightly higher if longer readout times were used, but the effect should not be too severe. In all measurements done in this work, the minimal TE was extended by a maximum of 5 ms when switching from flow to flow+concomitant field compensation.

Another result of the optimization was that of all diffusion encoding schemes considered, the most b-value efficient eddy-current-compensated one was the TRSE ($+|-+|-$) sequence [RHWW03]. This is again due to the rather short readout time used in these

simulations. In contrast, it was shown that a sequence with only one RF pulse during the diffusion encoding, like $+ - |+$ can yield shorter TE for higher resolutions and therefore longer readout durations [Fin09]. Again, the latter sequence is a special case of the actually implemented sequence.

The sequence with the highest possible b-value depends on the actual timing. Since normally the readout time is longer than the excitation time, it seems reasonable for sequences with one refocusing pulse to use more gradient pulses before the RF pulse compared to after the RF pulse, which is also reflected in the optimization. Besides the higher sensitivity to RF pulse imperfections, the inclusion of a second RF pulse also leads to lower b-values, especially for short TE. The main reason being that the time for the RF pulse cannot be freely used for maximizing the b-value.

The optimization presented here nulls eddy currents for one decay time, but, as mentioned above, it can be beneficial to partly compensate two decay times [Fin10]. This could be implemented in the optimization quite easily. The same holds true for the compensation of higher gradient moments, which proved to be beneficial in cardiovascular diffusion measurements [FSNL15, WDH15, SvDG+16]. Both adjustments require an additional constraint, which could quite easily be included in the optimization.

8.2.2 Phantom Experiments

The phantom experiments served two purposes, one was to prove the flow compensation and the other was to examine the capabilities of eddy current compensation.

To demonstrate the flow compensation, a simple phantom was used which consisted of a tube with water flowing through it. More advanced phantoms exist, which also try to mimic the microstructure in perfused tissue [MMJ91, CC01, CKJ+12], but they were not needed here as only principal flow compensation should be shown. This was achieved for all compensation combinations that included flow. There was a minor deviation between the flow compensated measurements and the measurements without flow. The reason for this could be the pulsatile part of the flow produced by the peristaltic pump. The sequence was only designed to compensate for constant flow, therefore the pulsatile part can lead to an additional signal decay. The eddy-current-compensated versions of the proposed sequence without explicit flow compensation exhibited a faster signal decay than the flow-compensated ones, but a slower decay than the other non-flow-compensated sequences. The reason for this partial flow compensation lies in the sequence design. For the eddy current compensation the highest b-value is achieved for the scheme $+ - | + -$, which is the same as the one often used for flow compensation [DRTW02, GBK07, AKW+16]. The actual gradient durations are different, which leads only to a partial flow compensation. The same effect leads to a partial eddy current compensation in the flow-compensated sequence as can be seen by the CV measured in the grid phantom.

The two small ROIs (see figure 7.2) can be regarded as representative if only smaller structures are of interest, for example, in prostate imaging, while the whole image might be more representative for measurements with a larger FOV like the abdomen. This analogy does not include image distortions due to susceptibility artifacts, which can be important in prostate diffusion imaging [MVN+13, DCY+14]. These were most prominent at the

upper edge of the phantom. Different image distortions at boundaries can lead to high CV-values as it includes actual signal as well as noise. In diffusion tensor imaging (DTI), this can lead to high anisotropy values [JC10]. In the grid phantom measurements, an eddy current compensation always decreased the high CV values at the edge when added to any combination of compensations.

The differences between the different combination schemes are more pronounced in the whole image analysis. For flow+concomitant field and flow+concomitant field+eddy current compensation the results are nearly the same. This might be explained by the experiment design. The measurements were performed with constant TE (and thus T_D) and b-value. This led to different gradient amplitudes. As eddy currents scale with the gradient amplitude [VVB90, JWS90, JBP98], the advantage of a better eddy current compensation can be evened out by the higher gradient amplitude needed. This effect, however, cannot explain the higher CV in concomitant field+eddy current compensation compared to only eddy current compensation. In the optimization these two sequences showed only minor b-value differences and therefore the gradient amplitude should not have varied much.

The differences between most compensation combinations vanish when considering the smaller ROIs. The only two schemes standing out are the ones without any and with only concomitant field compensation. These mostly use two long gradient pulses with the same polarity, which leads to considerable artifacts already close to the isocenter of the MRI machine where the CV is smallest. The totally uncompensated sequence additionally uses a short gradient pulse with opposite polarity which reduces the eddy currents a little bit.

8.2.3 In Vivo Measurements

To verify the advantages of the proposed compensations for actual in vivo studies, three different body parts were imaged: head, abdomen and prostate.

The stability of the brain measurements was tested by determining the diffusion coefficient for each of the three acquired diffusion directions as well as for the trace weighted image. This was done for each repetition individually. To distinguish the two diffusion coefficients, the ones for the individual directions are called ADC and the one for the trace weighted image is named MD. That means ADC still includes the directional dependence, while MD represents $\mathrm{tr}(\underline{\underline{D}})$.

Diffusion in the white matter in the brain is highly anisotropic [MCK+90, CBP90, JSWH99], while the MD changes only little over larger areas. This might lead to the conclusion that the improvement in signal stability might have larger effects for the individual ADC maps compared to the MD. This was not confirmed by the measurements as the CV changes are approximately the same for all maps. One reason could be the fact that the images used for the calculation of both diffusion metrics are still highly dependent on the diffusion encoding direction. Eddy current artifacts, which are a main cause for misalignment, show therefore similar effects for the parameter map stability.

Another source of artifacts in DWI is the pulsatile motion of the brain [BBG+99, SA01]. The source of the pulsations is the heart beat and the resulting blood flow and pressure variations [WEM11]. The amplitude of the brain parenchyma movement is normally below 1 mm [PWWC92, EP92] and therefore below the image resolution used here and thus

should not lead to misalignments. The velocities of brain parenchyma can go up to 2 mm/s, which is in the same order of flow velocities in small blood vessels [KPS05, SKK16]. The brain pulsation can therefore lead to severe artifacts, due to additional signal dephasing and dropouts [GWF+92]. These motion artifacts can be reduced by the use of a cardiac trigger [HAM10, KDR+13] which in turn leads to longer measurement times. It was previously shown that the use of flow-compensated diffusion encodings can be beneficial for diffusion measurements in the brain [PN91, BTW+95]. These results were confirmed in this work, although, it was not examined if the main source of improvement was the motion compensation or the reduced eddy currents. The reduction in the CV-values in the phantom and in the brain follows parallel trends. In the phantom the improvements cannot be attributed to reduced flow artifacts as convectional flows cannot explain the reduced CV at the edge and should produce larger patterns on the magnitude images inside the phantom which would have been visible in the CV maps

The improved image quality is translated to the diffusion tensor estimations where a it can be seen in the artificially increased FA-values at the edge of the brain. When switching from only concomitant field compensation to the full compensation these are reduced considerably. The advantages are also visible further away from the edges as all pixels are possibly affected by eddy current and pulsation artifacts [JC10]. This higher stability in the images could also improve model based estimations of brain microstructure, for example with CHARMED [AFRB04, AB05], AxCaliber [ABKYB08], NODDI [ZSWKA12] or many other model based approaches.

In contrast to the head, there was no improvement in image stability due to the use of flow compensation in the prostate indicating that pulsation or bowel motion was not an issue during these measurements. Nevertheless, they might have been present between measurements as the prostate outline in the examined slice changed slightly once between concurrent measurements during the stability tests. A major improvement in image stability is seen when concomitant field compensation is added to the flow compensation. An additional eddy current compensation does not add to the image stability. In light of the grid phantom measurements, this suggests that the improvement is caused by the reduction of eddy current artifacts. These potential artifacts can lead to erroneous estimates in prostate DWI [RT14].

For the abdomen measurements, the stability was not tested. Since the measurements were performed in free breathing, the breathing motion would have dominated the signal variations and the proposed compensation was not designed to correct for this. To compensate for breathing motion, different approaches could be implemented such as a respiratory trigger [NDH+10, TSS+09] or acquiring the images in breath-hold [CBMS03]. Both techniques have their drawbacks as they, for example, require longer acquisition times. The averaging over several repetitions leads in turn to image blurring. Two studies showed that measurements under free breathing and with respiratory gating produce similar results [DGN+13, JOd+14].

Most IVIM measurements were performed without flow compensation, thus, these values should be compared to the only concomitant-field-compensated sequence. Here the values lie in the area of previously reported ones. In the kidney the perfusion fraction is slightly higher than the reported range, which roughly is from 0.15 to 0.26 [LSSL11,

JOd+14, NCM+15, BDFT16] (here: 0.28 ± 0.18), in contrast to the value for D which is in between the reported values, that are distributed between 1.4 and 2.4 $\mu m^2/ms$ [LSSL11, JOd+14, NCM+15, BDFT16] (here: $1.9 \pm 0.54\,\mu m^2/ms$). For the liver, the reported f-values vary a lot between 0.13 and 0.34 [LSSL11, DJK+14, JOd+14, BDFT16, WSL15] (here: 0.31 ± 0.05), while for D the values are between 0.8 and 1.2 $\mu m^2/ms$ [LSSL11, DJK+14, JOd+14, BDFT16, WSL15] (here: $1.12 \pm 0.25\,\mu m^2/ms$). The values reported here lie in these intervals. The same holds true for the spleen as the f-values in the literature are between 0.05 and 0.15 (here: 0.12 ± 0.05) and results for D range from 0.6 to 0.9 $\mu m^2/ms$ [LSSL11, JOd+14, BDFT16] (here: $0.78 \pm 0.13\,\mu m^2/ms$).

In the prostate measurements, similar trends are true as the measured values for the central gland and peripheral zone are comparable to previously reported ones. In the central gland these were for f between 0.06 and 0.18 (here: 0.08 ± 0.02) and for D between 1.3 and 1.5 $\mu m^2/ms$ [RHCEdS09, MMP+17] (here: $1.25 \pm 0.10\,\mu m^2/ms$). In the peripheral zone the values for f were roughly between 0.03 and 0.23 (here: 0.18 ± 0.04) and for D between 1.3 and 1.8 $\mu m^2/ms$ [RHCEdS09, DLWS11, PTB+13, KRS+14, MMP+17, PPF+17] (here: 1.73 ± 0.24).

The previously reported results for IVIM parameters show a large variation. This is due to several reasons, as the results depend on the choice of b-values [PTB+13], the fitting algorithm [KRS+14, MMP+17] and, of course, the individual who was measured. There are several ways to optimize the choice of b-values for individual organs and they lead to different protocols [LSSL11, ZSR+12, DJK+14] for each organ. Since the main target of the measurements of healthy volunteers was to show the feasibility of IVIM measurements with the proposed sequence, the b-values were adjusted from clinical protocols that are used at this institution for standard diffusion imaging.

The results for $D^\star$ were not considered further as they show a very low reproducibility [DJK+14, MMP+17].

For the flow-compensated and the non-flow-compensated IVIM measurements, the diffusion coefficient D is roughly the same. This could be expected, since the biexponential model was introduced to differentiate between actual diffusion and effects that only seem like diffusion, namely perfusion [LBL+86, LBL+88]. The model assumes that the blood flow in the capillaries changes the direction often enough so that it can be treated as a fast diffusive motion. The long diffusion times needed for this model are normally not achieved [WSL15], therefore the use of a flow compensation makes a difference. This explains the lower f-values in the flow-compensated measurements as the fast initial decrease is partly compensated.

It should also be noted that the flow-compensated fits showed smaller confidence intervals, indicating more stable measurements. The only exception was in the case of flow+ concomitant field compensation in the prostate. One reason could be the low value for f which means that there is mainly a monoexponential decay, leading to a higher sensitivity to noise for the fit. Additionally, the images show a larger signal variation, meaning that there maybe were small motion artifacts.

In the measurements of prostate cancer, the diffusion curves showed a difference between cancerous tissue and the reference regions. This is already used in clinical practice for cancer detection with the monoexponential model [WBC+16]. There were also studies that

examined IVIM parameters for improved detection and staging [STS+12, KRS+14, PPF+17]. They found significant differences between healthy and cancerous tissue, but they were not able to differentiate between prostate cancer and BPH [PPF+17]. BPH was not examined in this study but neither in the healthy volunteer nor in the patients a difference in the central gland could be found by the use of flow compensation. This indicates that BPH could not be identified any better by flow-compensated IVIM. For a definite conclusion, a more detailed study is needed.

For such a study, it would be beneficial to use more b-values because the fitting results here showed large uncertainties. Nevertheless the use of a compensated sequence could improve future studies, as the phantom measurements and the healthy volunteer showed a clear improvement in image stability. The large uncertainties and nonsensical IVIM parameters could also be indicating that IVIM is no suitable model to describe the microstructure in prostate cancer.

8.3 Summary

The aim of this work was to improve the determination of different tissue parameters by non-invasive diffusion imaging. Therefore, novel MRI sequences were developed. DWI is a promising tool to probe the tissue microstructure as the range of the random motion is in the same order as relevant cell sizes, which is smaller than the image resolution. It thus allows one to infer information that is otherwise not accessible or requires the use of contrast agents. The diffusion measurements in turn can suffer from artifacts that are caused by the high gradient amplitudes needed for the diffusion encoding. In this work, two sequences were developed that allowed the compensation of the most severe artifacts. For the determination of the microscopic anisotropy, given by μFA, an eddy-current-compensated DDE sequence was implemented. For the determination of the perfusion fraction f with the intravoxel incoherent motion (IVIM) model, a single diffusion encoded sequence was used. This sequence can be compensated for flow, concomitant fields and eddy currents individually and in any combination. For both techniques, clear improvements in the stability could be shown in phantom experiments as well as in vivo.

Bibliography

[AB05] Y. Assaf and P. J. Basser. Composite hindered and restricted model of diffusion (CHARMED) MR imaging of the human brain. Neuroimage, 27(1):48–58, 2005.

[ABKYB08] Y. Assaf, T. Blumenfeld-Katzir, Y. Yovel, and P. J. Basser. AxCaliber: a method for measuring axon diameter distribution from diffusion MRI. Magnetic Resonance in Medicine, 59(6):1347–1354, 2008.

[Abr11] A. Abragam. The principles of nuclear magnetism. International series of monographs on physics. Oxford Univ. Pr., Oxford [u.a.], repr. edition, 2011.

[AFRB04] Y. Assaf, R. Z. Freidlin, G. K. Rohde, and P. J. Basser. New modeling and experimental framework to characterize hindered and restricted water diffusion in brain white matter. Magnetic Resonance in Medicine, 52(5):965–978, 2004.

[AKW+16] A. Ahlgren, L. Knutsson, R. Wirestam, M. Nilsson, F. Stahlberg, D. Topgaard, and S. Lasic. Quantification of microcirculatory parameters by joint analysis of flow-compensated and non-flow-compensated intravoxel incoherent motion (IVIM) data. NMR in Biomedicine, 29(5):640–649, 2016.

[AWE17] E. Aliotta, H. H. Wu, and D. B. Ennis. Convex optimized diffusion encoding (CODE) gradient waveforms for minimum echo time and bulk motion-compensated diffusion-weighted MRI. Magnetic Resonance in Medicine, 77(2):717–729, 2017.

[BBG+99] S. Brockstedt, M. Borg, B. Geijer, R. Wirestam, C. Thomsen, S. Holtas, and F. Stahlberg. Triggering in quantitative diffusion imaging with single-shot EPI. Acta Radiologica, 40(3):263–269, 1999.

[BDFT16] S. Barbieri, O. F. Donati, J. M. Froehlich, and H. C. Thoeny. Comparison of Intravoxel Incoherent Motion Parameters across MR Imagers and Field Strengths: Evaluation in Upper Abdominal Organs. Radiology, 279(3):784–794, 2016.

[BGM91] C. Boesch, R. Gruetter, and E. Martin. Temporal and spatial analysis of fields generated by eddy currents in superconducting magnets: optimization of corrections and quantitative characterization of magnet/gradient systems. Magnetic Resonance in Medicine, 20(2):268–284, 1991.

[BGN00] R. H. Byrd, J. C. Gilbert, and J. Nocedal. A trust region method based on interior point techniques for nonlinear programming. Mathematical Programming, 89(1):149–185, 2000.

[BHN99] R. H. Byrd, M. E. Hribar, and J. Nocedal. An interior point algorithm for large-scale nonlinear programming. Siam Journal on Optimization, 9(4):877–900, 1999.

[BKKT04] N. Bodammer, J. Kaufmann, M. Kanowski, and C. Tempelmann. Eddy current correction in diffusion-weighted imaging using pairs of images acquired with opposite diffusion gradient polarity. Magnetic Resonance in Medicine, 51(1):188–193, 2004.

[BKZ04] M. A. Bernstein, K. F. King, and X. J. Zhou. Handbook of MRI pulse sequences. Elsevier, 2004.

[Blo46] F. Bloch. Nuclear Induction. Physical Review, 70(7-8):460–474, 1946.

[BM91] R. Bowtell and P. Mansfield. Gradient coil design using active magnetic screening. Magnetic Resonance in Medicine, 17(1):15–21, 1991.

[BML94a] P. J. Basser, J. Mattiello, and D. LeBihan. Estimation of the effective self-diffusion tensor from the NMR spin echo. Journal of Magnetic Resonance Series B, 103(3):247–254, 1994.

[BML94b] P. J. Basser, J. Mattiello, and D. LeBihan. MR diffusion tensor spectroscopy and imaging. Biophysical Journal, 66(1):259–267, 1994.

[BTW+95] S. Brockstedt, C. Thomsen, R. Wirestam, J. De Poorter, C. De Wagter, L. G. Salford, S. Holtas, and F. Stahlberg. Use of an enhanced gradient system for diffusion MR imaging with motion-artifact reduction. Acta Radiologica, 36(6):662–670, 1995.

[BW84] Paul A. Bottomley and A. William. Method of eliminating effects of spurious free induction decay NMR signal caused by imperfect 180 degrees RF pulses. Patent US4484138 A, November 1984.

[CBMS03] L. C. Chow, R. Bammer, M. E. Moseley, and F. G. Sommer. Single breath-hold diffusion-weighted imaging of the abdomen. Journal of Magnetic Resonance Imaging, 18(3):377–382, 2003.

[CBP90] T. L. Chenevert, J. A. Brunberg, and J. G. Pipe. Anisotropic diffusion in human white matter: demonstration with MR techniques in vivo. Radiology, 177(2):401–405, 1990.

[CC01] P. T. Callaghan and S. L. Codd. Flow coherence in a bead pack observed using frequency domain modulated gradient nuclear magnetic resonance. Physics of Fluids, 13(2):421–427, 2001.

[CCM+91] P. T. Callaghan, A. Coy, D. MacGowan, K. J. Packer, and F. O. Zelaya. Diffraction-like effects in NMR diffusion studies of fluids in porous solids. Nature, 351(6326):467–469, 1991.

[CG90] D. G. Cory and A. N. Garroway. Measurement of Translational Displacement Probabilities by Nmr - an Indicator of Compartmentation. Magnetic Resonance in Medicine, 14(3):435–444, 1990.

[CHSM89] R. M. Cotts, M. J. R. Hoch, T. Sun, and J. T. Markert. Pulsed Field Gradient Stimulated Echo Methods for Improved Nmr Diffusion Measurements in Heterogeneous Systems. Journal of Magnetic Resonance, 83(2):252–266, 1989.

[CKJ+12] G. Y. Cho, S. Kim, J. H. Jensen, P. Storey, D. K. Sodickson, and E. E. Sigmund. A versatile flow phantom for intravoxel incoherent motion MRI. Magnetic Resonance in Medicine, 67(6):1710–1720, 2012.

[DCY+14] Jr. Donato, F., D. N. Costa, Q. Yuan, N. M. Rofsky, R. E. Lenkinski, and I. Pedrosa. Geometric distortion in diffusion-weighted MR imaging of the prostate-contributing factors and strategies for improvement. Academic Radiology, 21(6):817–823, 2014.

[DGN+13] H. A. Dyvorne, N. Galea, T. Nevers, M. I. Fiel, D. Carpenter, E. Wong, M. Orton, A. de Oliveira, T. Feiweier, M. L. Vachon, J. S. Babb, and B. Taouli. Diffusion-weighted Imaging of the Liver with Multiple b Values: Effect of Diffusion Gradient Polarity and Breathing Acquisition on Image Quality and Intravoxel Incoherent Motion Parameters-A Pilot Study. Radiology, 266(3):920–929, 2013.

[DJK+14] H. Dyvorne, G. Jajamovich, S. Kakite, B. Kuehn, and B. Taouli. Intravoxel incoherent motion diffusion imaging of the liver: Optimal b-value subsampling and impact on parameter precision and reproducibility. European Journal of Radiology, 83(12):2109–2113, 2014.

[DLWS11] J. Dopfert, A. Lemke, A. Weidner, and L. R. Schad. Investigation of prostate cancer using diffusion-weighted intravoxel incoherent motion imaging. Magnetic Resonance Imaging, 29(8):1053–1058, 2011.

[DPG03] M. D. Does, E. C. Parsons, and J. C. Gore. Oscillating gradient measurements of water diffusion in normal and globally ischemic rat brain. Magnetic Resonance in Medicine, 49(2):206–215, 2003.

[DRTW02] J. G. Dou, T. G. Reese, W. Y. I. Tseng, and V. J. Wedeen. Cardiac diffusion MRI without motion effects. Magnetic Resonance in Medicine, 48(1):105–114, 2002.

[DW14] D. Drenckhahn and J. Waschke. Benninghoff Taschenbuch Anatomie. Urban & Fischer in Elsevier, 2014.

[EAJAE05] J. I. Epstein, W. C. Allsbrook Jr, M. B. Amin, and L. L. Egevad. The 2005 international society of urological pathology (isup) consensus conference on gleason grading of prostatic carcinoma. The American journal of surgical pathology, 29(9):1228–1242, 2005.

[Ein05] A. Einstein. Über die von der molekularkinetischen Theorie der Wärme geforderte Bewegung von in ruhenden Flüssigkeiten suspendierten Teilchen. Annalen der Physik, 322(8):549–560, 1905.

[ELT13] S. Eriksson, S. Lasic, and D. Topgaard. Isotropic diffusion weighting in PGSE NMR by magic-angle spinning of the q-vector. J Magn Reson, 226:13–18, 2013.

[EP92] D. R. Enzmann and N. J. Pelc. Brain motion: measurement with phase-contrast MR imaging. Radiology, 185(3):653–660, 1992.

[Fic55] A. Fick. Ueber Diffusion. Annalen der Physik, 170(1):59–86, 1855.

[Fin09] J. Finsterbusch. Eddy-current compensated diffusion weighting with a single refocusing RF pulse. Magnetic Resonance in Medicine, 61(3):748–754, 2009.

[Fin10] J. Finsterbusch. Double-spin-echo diffusion weighting with a modified eddy current adjustment. Magnetic Resonance Imaging, 28(3):434–440, 2010.

[Fin11] J. Finsterbusch. The parallel-antiparallel signal difference in double-wave-vector diffusion-weighted MR at short mixing times: a phase evolution perspective. J Magn Reson, 208(1):114–121, 2011.

[FSNL15] M. Froeling, G. J. Strijkers, A. J. Nederveen, and P. R. Luijten. Whole heart DTI using asymmetric bipolar diffusion gradients. Journal of Cardiovascular Magnetic Resonance, 17(1):P15, 2015.

[GBK07] U. Gamper, P. Boesiger, and S. Kozerke. Diffusion imaging of the in vivo heart using spin echoes–considerations on bulk motion sensitivity. Magnetic Resonance in Medicine, 57(2):331–337, 2007.

[GJH+02] M. A. Griswold, P. M. Jakob, R. M. Heidemann, M. Nittka, V. Jellus, J. Wang, B. Kiefer, and A. Haase. Generalized autocalibrating partially parallel acquisitions (GRAPPA). Magnetic Resonance in Medicine, 47(6):1202–1210, 2002.

[Glo98] F. Glover. A template for scatter search and path relinking. In Jin-Kao Hao, Evelyne Lutton, Edmund Ronald, Marc Schoenauer, and Dominique Snyers, editors, Artificial Evolution: Third European Conference AE '97 Nîmes, France, October 22–24, 1997 Selected Papers, pages 1–51. Springer, Berlin, Heidelberg, 1998.

[GP09] M. Graf and D. Potts. Sampling Sets and Quadrature Formulae on the Rotation Group. Numerical Functional Analysis and Optimization, 30(7-8):665–688, 2009.

[Gre07] D. S. Grebenkov. NMR survey of reflected Brownian motion. Reviews of Modern Physics, 79:1077–1137, Aug 2007.

[GWF+92] D. Greitz, R. Wirestam, A. Franck, B. Nordell, C. Thomsen, and F. Stahlberg. Pulsatile brain movement and associated hydrodynamics studied by magnetic resonance phase imaging. The Monro-Kellie doctrine revisited. Neuroradiology, 34(5):370–380, 1992.

[GXC+10] J. C. Gore, J. Z. Xu, D. C. Colvin, T. E. Yankeelov, E. C. Parsons, and M. D. Does. Characterization of tissue structure at varying length scales using temporal diffusion spectroscopy. NMR in Biomedicine, 23(7):745–756, 2010.

[Hah50] E. L. Hahn. Spin Echoes. Physical Review, 80(4):580–594, 1950.

[HAM10] J. Habib, D. P. Auer, and P. S. Morgan. A quantitative analysis of the benefits of cardiac gating in practical diffusion tensor imaging of the brain. Magnetic Resonance in Medicine, 63(4):1098–1103, 2010.

[HBTV99] E. M. Haacke, R. W. Brown, M. R. Thompson, and R. Venkatesan. Magnetic resonance imaging : physical principles and sequence design. Wiley-Liss, New York [u.a.], 1999.

[Hei00] O. Heid. Eddy current-nulled diffusion weighting. Proceedings of the International Society of Magnetic Resonance in Medicine, Denver, CO, 799, 2000.

[HM96] J. C. Haselgrove and J. R. Moore. Correction for distortion of echo-planar images used to calculate the apparent diffusion coefficient. Magnetic Resonance in Medicine, 36(6):960–964, 1996.

[Hor99] M. A. Horsfield. Mapping eddy current induced fields for the correction of diffusion-weighted echo planar images. Magn Reson Imaging, 17(9):1335–1345, 1999.

[Hur98] M. D. Hurlimann. Effective Gradients in Porous Media Due to Susceptibility Differences. Journal of Magnetic Resonance, 131(2):232–240, 1998.

[JB11] S. N. Jespersen and N. Buhl. The displacement correlation tensor: Microstructure, ensemble anisotropy and curving fibers. Journal of Magnetic Resonance, 208(1):34–43, 2011.

[JBDN87] D. J. Jensen, W. W. Brey, J. L. Delayre, and P. A. Narayana. Reduction of pulsed gradient settling time in the superconducting magnet of a magnetic resonance instrument. Medical Physics, 14(5):859–862, 1987.

[JBP98] P. Jezzard, A. S. Barnett, and C. Pierpaoli. Characterization of and correction for eddy current artifacts in echo planar diffusion imaging. Magnetic Resonance Medicine, 39(5):801–812, 1998.

[JC10] D. K. Jones and M. Cercignani. Twenty-five pitfalls in the analysis of diffusion mri data. NMR in Biomedicine, 23(7):803–820, 2010.

[Jes12] S. N. Jespersen. Equivalence of double and single wave vector diffusion contrast at low diffusion weighting. Nmr in Biomedicine, 25(6):813–818, 2012.

[JH10] J. H. Jensen and J. A. Helpern. MRI quantification of non-Gaussian water diffusion by kurtosis analysis. NMR in Biomedicine, 23(7):698–710, 2010.

[JLSD13] S. N. Jespersen, H. Lundell, C. K. Sonderby, and T. B. Dyrby. Orientationally invariant metrics of apparent compartment eccentricity from double pulsed field gradient diffusion experiments. NMR in Biomedicine, 26(12):1647–1662, 2013.

[JLSD14a] S. N. Jespersen, H. Lundell, C. K. Sønderby, and T. B. Dyrby. Commentary on "Microanisotropy imaging: quantification of microscopic diffusion anisotropy and orientation of order parameter by diffusion MRI with magic-angle spinning of the q-vector". Frontiers in Physics, 2:28, 2014.

[JLSD14b] S. N. Jespersen, H. Lundell, C. K. Sonderby, and T. B. Dyrby. Erratum: Orientationally invariant metrics of apparent compartment eccentricity from double pulsed field gradient diffusion experiments. NMR in Biomedicine, 27(6):738–738, 2014.

[JOd+14] N. P. Jerome, M. R. Orton, J. A. d'Arcy, D. J. Collins, D. M. Koh, and M. O. Leach. Comparison of Free-Breathing With Navigator-Controlled Acquisition Regimes in Abdominal Diffusion-Weighted Magnetic Resonance Images: Effect on ADC and IVIM Statistics. Journal of Magnetic Resonance Imaging, 39(1):235–240, 2014.

[Jon11] D. K. Jones, editor. Diffusion MRI. Oxford Univ. Press, New York ; Oxford, 2011.

[JSWH99] D. K. Jones, A. Simmons, S. C. Williams, and M. A. Horsfield. Non-invasive assessment of axonal fiber connectivity in the human brain via diffusion tensor MRI. Magnetic Resonance in Medicine, 42(1):37–41, 1999.

[JWS90] P. Jehenson, M. Westphal, and N. Schuff. Analytical method for the compensation of eddy-current effects induced by pulsed magnetic field gradients in NMR systems. Journal of Magnetic Resonance (1969), 90(2):264–278, 1990.

[KDR+13] L. R. Kozak, S. David, G. Rudas, Z. Vidnyanszky, A. Leemans, and Z. Nagy. Investigating the need of triggering the acquisition for infant diffusion MRI:

a quantitative study including bootstrap statistics. Neuroimage, 69:198–205, 2013.

[KF08] M. A. Koch and J. Finsterbusch. Compartment size estimation with double wave vector diffusion-weighted imaging. Magnetic Resonance in Medicine, 60(1):90–101, 2008.

[KF09] M. A. Koch and J. Finsterbusch. Numerical Simulation of Double-Wave Vector Experiments Investigating Diffusion in Randomly Oriented Ellipsoidal Pores. Magnetic Resonance in Medicine, 62(1):247–254, 2009.

[Kin06] P. B. Kingsley. Introduction to diffusion tensor imaging mathematics: Part III. Tensor calculation, noise, simulations, and optimization. Concepts in Magnetic Resonance Part A, 28A(2):155–179, 2006.

[KLG+11] M. Klauss, A. Lemke, K. Grunberg, D. Simon, T. J. Re, M. N. Wente, F. B. Laun, H. U. Kauczor, S. Delorme, L. Grenacher, and B. Stieltjes. Intravoxel incoherent motion MRI for the differentiation between mass forming chronic pancreatitis and pancreatic carcinoma. Investigative Radiology, 46(1):57–63, 2011.

[KPS05] R. Klinke, H.-C. Pape, and S. Silbernagl. Physiologie. Thieme Electronic Book Library. Thieme, Stuttgart, 5. komplett überarbeitete Auflage edition, 2005.

[KRS+14] T. H. Kuru, M. C. Roethke, B. Stieltjes, K. Maier-Hein, H. P. Schlemmer, B. A. Hadaschik, and M. Fenchel. Intravoxel Incoherent Motion (IVIM) Diffusion Imaging in Prostate Cancer - What Does It Add? Journal of Computer Assisted Tomography, 38(4):558–564, 2014.

[LBF15] M. Lawrenz, S. Brassen, and J. Finsterbusch. Microscopic diffusion anisotropy in the human brain: reproducibility, normal values, and comparison with the fractional anisotropy. Neuroimage, 109:283–297, 2015.

[LBL+86] D. LeBihan, E. Breton, D. Lallemand, P. Grenier, E. Cabanis, and M. Laval-jeantet. MR Imaging of Intravoxel Incoherent Motions - Application to Diffusion and Perfusion in Neurologic Disorders. Radiology, 161(2):401–407, 1986.

[LBL+88] D. LeBihan, E. Breton, D. Lallemand, M. L. Aubin, J. Vignaud, and M. Laval-jeantet. Separation of Diffusion and Perfusion in Intravoxel Incoherent Motion MR Imaging. Radiology, 168(2):497–505, 1988.

[LF13] M. Lawrenz and J. Finsterbusch. Double-wave-vector diffusion-weighted imaging reveals microscopic diffusion anisotropy in the living human brain. Magnetic Resonance in Medicine, 69(4):1072–1082, 2013.

[LF15] M. Lawrenz and J. Finsterbusch. Mapping measures of microscopic diffusion anisotropy in human brain white matter in vivo with double-wave-vector diffusion-weighted imaging. Magnetic Resonance in Medicine, 73(2):773–783, 2015.

[LF16] M. Lawrenz and J. Finsterbusch. Detection of Microscopic Diffusion Anisotropy in Human Brain Cortical Gray Matter in Vivo with Double Diffusion Encoding. Proceedings of the International Society for Magnetic Resonance in Medicine, Singapore, 212, 2016.

[LHS09] F. B. Laun, S. Huff, and B. Stieltjes. On the effects of dephasing due to local gradients in diffusion tensor imaging experiments: relevance for diffusion tensor imaging fiber phantoms. Magnetic Resonance Imaging, 27(4):541–548, 2009.

[LKF10] Marco Lawrenz, Martin A. Koch, and Jürgen Finsterbusch. A tensor model and measures of microscopic anisotropy for double-wave-vector diffusion-weighting experiments with long mixing times. Journal of Magnetic Resonance, 202(1):43 – 56, 2010.

[LNL+11] S. Lasic, M. Nilsson, J. Latt, F. Stahlberg, and D. Topgaard. Apparent exchange rate mapping with diffusion MRI. Magnetic Resonance in Medicine, 66(2):356–365, 2011.

[LSE+14] S. Lasič, F. Szczepankiewicz, S. Eriksson, M. Nilsson, and D. Topgaard. Microanisotropy imaging: quantification of microscopic diffusion anisotropy and orientational order parameter by diffusion MRI with magic-angle spinning of the q-vector. Frontiers in Physics, 2:11, 2014.

[LSSL11] A. Lemke, B. Stieltjes, L. R. Schad, and F. B. Laun. Toward an optimal distribution of b values for intravoxel incoherent motion imaging. Magnetic Resonance Imaging, 29(6):766–776, 2011.

[LVC+08] A. Luciani, A. Vignaud, M. Cavet, J. T. Nhieu, A. Mallat, L. Ruel, A. Laurent, J. F. Deux, P. Brugieres, and A. Rahmouni. Liver cirrhosis: intravoxel incoherent motion MR imaging–pilot study. Radiology, 249(3):891–899, 2008.

[Man77] P. Mansfield. Multi-planar image formation using NMR spin echoes. Journal of Physics C: Solid State Physics, 10(3):L55, 1977.

[MC86a] P. Mansfield and B. Chapman. Active Magnetic Screening of Coils for Static and Time-Dependent Magnetic-Field Generation in NMR Imaging. Journal of Physics E-Scientific Instruments, 19(7):540–545, 1986.

[MC86b] P. Mansfield and B. Chapman. Active Magnetic Screening of Gradient Coils in NMR Imaging. Journal of Magnetic Resonance, 66(3):573–576, 1986.

[MC87] P. Mansfield and B. Chapman. Multishield Active Magnetic Screening of Coil Structures in NMR. Journal of Magnetic Resonance, 72(2):211–223, 1987.

[MCK+90] M. E. Moseley, Y. Cohen, J. Kucharczyk, J. Mintorovitch, H. S. Asgari, M. F. Wendland, J. Tsuruda, and D. Norman. Diffusion-weighted MR imaging of anisotropic water diffusion in cat central nervous system. Radiology, 176(2):439–445, 1990.

[MCM+90] M. E. Moseley, Y. Cohen, J. Mintorovitch, L. Chileuitt, H. Shimizu, J. Kucharczyk, M. F. Wendland, and P. R. Weinstein. Early detection of regional cerebral ischemia in cats: comparison of diffusion- and T2-weighted MRI and spectroscopy. Magnetic Resonance in Medicine, 14(2):330–46, 1990.

[MH95] P. P. Mitra and B. I. Halperin. Effects of finite gradient-pulse widths in pulsed-field-gradient diffusion measurements. Journal of Magnetic Resonance, Series A, 113(1):94 – 101, 1995.

[Mit95] P. P. Mitra. Multiple wave-vector extensions of the NMR pulsed-field-gradient spin-echo diffusion measurement. Physical Review B, 51(21):15074–15078, 1995.

[MKAN91] M. E. Moseley, J. Kucharczyk, H. S. Asgari, and D. Norman. Anisotropy in diffusion-weighted MRI. Magnetic Resonance in Medicine, 19(2):321–326, 1991.

[MMJ91] J. H. Maki, J. R. MacFall, and G. A. Johnson. The use of gradient flow compensation to separate diffusion and microcirculatory flow in MRI. Magnetic Resonance in Medicine, 17(1):95–107, 1991.

[MMK+10] S. Mohammadi, H. E. Moller, H. Kugel, D. K. Muller, and M. Deppe. Correcting eddy current and motion effects by affine whole-brain registrations: evaluation of three-dimensional distortions and comparison with slicewise correction. Magnetic Resonance in Medicine, 64(4):1047–1056, 2010.

[MMP+17] H. Merisaari, P. Movahedi, I. M. Perez, J. Toivonen, M. Pesola, P. Taimen, P. J. Bostrom, T. Pahikkala, A. Kiviniemi, H. J. Aronen, and I. Jambor. Fitting methods for intravoxel incoherent motion imaging of prostate cancer on region of interest level: Repeatability and gleason score prediction. Magnetic Resonance in Medicine, 77(3):1249–1264, 2017.

[Moa08] M. Moakher. Fourth-order cartesian tensors: old and new facts, notions and applications. The Quarterly Journal of Mechanics and Applied Mathematics, 61(2):181, 2008.

[Mor07] S. Mori. Introduction to diffusion tensor imaging. Elsevier, Amsterdam ; Boston [u.a.], 1. edition, 2007.

[MSS93] P. P. Mitra, P. N. Sen, and L. M. Schwartz. Short-time behavior of the diffusion coefficient as a geometrical probe of porous media. Physical Review B, 47(14):8565–8574, 1993.

[MSSLD92] P. P. Mitra, P. N. Sen, L. M. Schwartz, and P. Le Doussal. Diffusion propagator as a probe of the structure of porous media. Physical Review Letters, 68(24):3555–3558, 1992.

[MVN+13] Y. Mazaheri, H. A. Vargas, G. Nyman, O. Akin, and H. Hricak. Image artifacts on prostate diffusion-weighted magnetic resonance imaging: trade-offs at 1.5 Tesla and 3.0 Tesla. Academic Radiology, 20(8):1041–1047, 2013.

[MWKL17] L. Mueller, A. Wetscherek, T. A. Kuder, and F. B. Laun. Eddy current compensated double diffusion encoded (DDE) MRI. Magnetic Resonance in Medicine, 77(1):328–335, 2017.

[MZFP08] C. Meier, M. Zwanger, T. Feiweier, and D. Porter. Concomitant field terms for asymmetric gradient coils: Consequences for diffusion, flow, and echo-planar imaging. Magnetic Resonance in Medicine, 60(1):128–134, 2008.

[NCM+15] M. Notohamiprodjo, H. Chandarana, A. Mikheev, H. Rusinek, J. Grinstead, T. Feiweier, J. G. Raya, V. S. Lee, and E. E. Sigmund. Combined Intravoxel Incoherent Motion and Diffusion Tensor Imaging of Renal Diffusion and Flow Anisotropy. Magnetic Resonance in Medicine, 73(4):1526–1532, 2015.

[NDC+11] R. G. Nunes, I. Drobnjak, S. Clare, P. Jezzard, and M. Jenkinson. Performance of single spin-echo and doubly refocused diffusion-weighted sequences in the presence of eddy current fields with multiple components. Magnetic Resonance Imaging, 29(5):659–667, 2011.

[NDH+10] M. Notohamiprodjo, O. Dietrich, W. Horger, A. Horng, A. D. Helck, K. A. Herrmann, M. F. Reiser, and C. Glaser. Diffusion Tensor Imaging (DTI) of the Kidney at 3 Tesla-Feasibility, Protocol Evaluation and Comparison to 1.5 Tesla. Investigative Radiology, 45(5):245–254, 2010.

[NLvW+13] M. Nilsson, J. Latt, D. van Westen, S. Brockstedt, S. Lasic, F. Stahlberg, and D. Topgaard. Noninvasive mapping of water diffusional exchange in the human brain using filter-exchange imaging. Magnetic Resonance in Medicine, 69(6):1573–1581, 2013.

[NTW14] Z. Nagy, D. L. Thomas, and N. Weiskopf. Orthogonalizing crusher and diffusion-encoding gradients to suppress undesired echo pathways in the twice-refocused spin echo diffusion sequence. Magnetic Resonance in Medicine, 71(2):506–515, 2014.

[ÖB08] E. Özarslan and P. J. Basser. Microscopic anisotropy revealed by NMR double pulsed field gradient experiments with arbitrary timing parameters. Journal of Chemical Physics, 128(15):154511, 2008.

[Öza09] E. Özarslan. Compartment shape anisotropy (CSA) revealed by double pulsed field gradient MR. Journal of Magnetic Resonance, 199(1):56 – 67, 2009.

[PDG06] E. C. Parsons, M. D. Does, and J. C. Gore. Temporal diffusion spectroscopy: Theory and implementation in restricted systems using oscillating gradients. Magnetic Resonance in Medicine, 55(1):75–84, 2006.

[PN91] P. V. Prasad and O. Nalcioglu. A Modified Pulse Sequence for Invivo Diffusion Imaging with Reduced Motion Artifacts. Magnetic Resonance in Medicine, 18(1):116–131, 1991.

[PPF+17] F. Pesapane, F. Patella, E. M. Fumarola, S. Panella, A. M. Ierardi, G. G. Pompili, G. Franceschelli, S. A. Angileri, A. Magenta Biasina, and G. Carrafiello. Intravoxel Incoherent Motion (IVIM) Diffusion Weighted Imaging (DWI) in the Periferic Prostate Cancer Detection and Stratification. Medical Oncology, 34(3):35, 2017.

[PTB+13] Y. Pang, B. Turkbey, M. Bernardo, J. Kruecker, S. Kadoury, M. J. Merino, B. J. Wood, P. A. Pinto, and P. L. Choyke. Intravoxel incoherent motion MR imaging for prostate cancer: an evaluation of perfusion fraction and diffusion coefficient derived from different b-value combinations. Magnetic Resonance in Medicine, 69(2):553–562, 2013.

[PWWC92] B. P. Poncelet, V. J. Wedeen, R. M. Weisskoff, and M. S. Cohen. Brain parenchyma motion: measurement with cine echo-planar MR imaging. Radiology, 185(3):645–651, 1992.

[QBD+03] J. D. Quirk, G. L. Bretthorst, T. Q. Duong, A. Z. Snyder, C. S. Springer, J. J.H. Ackerman, and J. J. Neil. Equilibrium water exchange between the intra- and extracellular spaces of mammalian brain. Magnetic Resonance in Medicine, 50(3):493–499, 2003.

[RHCEdS09] S. F. Riches, K. Hawtin, E. M. Charles-Edwards, and N. M. de Souza. Diffusion-weighted imaging of the prostate and rectal wall: comparison of biexponential and monoexponential modelled diffusion and associated perfusion coefficients. NMR in Biomedicine, 22(3):318–325, 2009.

[RHWW03] T. G. Reese, O. Heid, R. M. Weisskoff, and V. J. Wedeen. Reduction of eddy-current-induced distortion in diffusion MRI using a twice-refocused spin echo. Magnetic Resonance in Medicine, 49(1):177–182, 2003.

[RT14] A. B. Rosenkrantz and S. S. Taneja. Radiologist, Be Aware: Ten Pitfalls That Confound the Interpretation of Multiparametric Prostate MRI. American Journal of Roentgenology, 202(1):109–120, 2014.

[SA01] S. Skare and J. L. Andersson. On the effects of gating in diffusion imaging of the brain using single shot EPI. Magnetic Resonance Imaging, 19(8):1125–1128, 2001.

[SB13] S. P. Sourbron and D. L. Buckley. Classic models for dynamic contrast-enhanced MRI. NMR in Biomedicine, 26(8):1004–1027, 2013.

[SBS+12] N. Shemesh, D. Barazany, O. Sadan, L. Bar, Y. Zur, Y. Barhum, N. Sochen, D. Offen, Y. Assaf, and Y. Cohen. Mapping apparent eccentricity and residual ensemble anisotropy in the gray matter using angular double-pulsed-field-gradient MRI. Magnetic Resonance in Medicine, 68(3):794–806, 2012.

[SC11a] N. Shemesh and Y. Cohen. Microscopic and Compartment Shape Anisotropies in Gray and White Matter Revealed by Angular Bipolar Double-PFG MR. Magnetic Resonance in Medicine, 65(5):1216–1227, 2011.

[SC11b] N. Shemesh and Y. Cohen. Overcoming apparent susceptibility-induced anisotropy (aSIA) by bipolar double-pulsed-field-gradient NMR. Journal of Magnetic Resonance, 212(2):362–369, 2011.

[SJA+16] N. Shemesh, S. N. Jespersen, D. C. Alexander, Y. Cohen, I. Drobnjak, T. B. Dyrby, J. Finsterbusch, M. A. Koch, T. Kuder, F. Laun, M. Lawrenz, H. Lundell, P. P. Mitra, M. Nilsson, E. Ozarslan, D. Topgaard, and C. F. Westin. Conventions and nomenclature for double diffusion encoding NMR and MRI. Magnetic Resonance in Medicine, 75(1):82–87, 2016.

[SKK16] S. Schaal, K. Kunsch, and S. Kunsch. Der Mensch in Zahlen : Eine Datensammlung in Tabellen mit über 20000 Einzelwerten. Springer Spektrum, Berlin, Heidelberg, 4. vollständig überarbeitete und ergänzte Auflage edition, 2016.

[SLvW+15] F. Szczepankiewicz, S. Lasic, D. van Westen, P. C. Sundgren, E. Englund, C. F. Westin, F. Stahlberg, J. Latt, D. Topgaard, and M. Nilsson. Quantification of microscopic diffusion anisotropy disentangles effects of orientation dispersion from microstructure: applications in healthy volunteers and in brain tumors. Neuroimage, 104:241–252, 2015.

[SOBC09] N. Shemesh, E. Ozarslan, P. J. Basser, and Y. Cohen. Measuring small compartmental dimensions with low-q angular double-PGSE NMR: The effect of experimental parameters on signal decay. Journal of Magnetic Resonance, 198(1):15–23, 2009.

[SSS09] M. Schünke, E. Schulte, and U. Schumacher. Prometheus - Lernatlas der Anatomie: Innere Organe ; 118 Tabellen. Number Bd. 2 in Prometheus. Thieme, 2009.

[ST65] E. O. Stejskal and J. E. Tanner. Spin Diffusion Measurements: Spin Echoes in the Presence of a Time-Dependent Field Gradient. Journal of Chemical Physics, 42(1):288, 1965.

[STS+12] H. Shinmoto, C. Tamura, S. Soga, E. Shiomi, N. Yoshihara, T. Kaji, and R. V. Mulkern. An intravoxel incoherent motion diffusion-weighted imaging study of prostate cancer. American Journal of Roentgenology, 199(4):496–500, 2012.

[SvDG+16] C. T. Stoeck, C. von Deuster, M. Genet, D. Atkinson, and S. Kozerke. Second-order motion-compensated spin echo diffusion tensor imaging of the human heart. Magnetic Resonance in Medicine, 75(4):1669–1676, 2016.

[Tor56] H. C. Torrey. Bloch Equations with Diffusion Terms. Physical Review, 104(3):563–565, 1956.

[TSS+09] B. Taouli, A. Sandberg, A. Stemmer, T. Parikh, S. Wong, J. Xu, and V. S. Lee. Diffusion-Weighted Imaging of the Liver: Comparison of Navigator Triggered and Breathhold Acquisitions. Journal of Magnetic Resonance Imaging, 30(3):561–568, 2009.

[Tuc04] D. S. Tuch. Q-Ball imaging. Magnetic Resonance in Medicine, 52(6):1358–1372, 2004.

[ULP+07] Z. Ugray, L. Lasdon, J. Plummer, F. Glover, J. Kelly, and R. Martí. Scatter Search and Local NLP Solvers: A Multistart Framework for Global Optimization. INFORMS Journal on Computing, 19(3):328–340, 2007.

[vK08] N. G. van Kampen. Stochastic processes in physics and chemistry. North-Holland personal library. Elsevier, Amsterdam ; Heidelberg [u.a.], 3. edition, 2008.

[VVB90] J. J. Van Vaals and A. H. Bergman. Optimization of eddy-current compensation. Journal of Magnetic Resonance, 90(1):52–70, 1990.

[vZY11] P. C. M. van Zijl and N. N. Yadav. Chemical exchange saturation transfer (CEST): What is in a name and what isn't? Magnetic Resonance in Medicine, 65(4):927–948, 2011.

[WBC+16] Jeffrey C. Weinreb, Jelle O. Barentsz, Peter L. Choyke, Francois Cornud, Masoom A. Haider, Katarzyna J. Macura, Daniel Margolis, Mitchell D. Schnall, Faina Shtern, Clare M. Tempany, Harriet C. Thoeny, and Sadna Verma. PI-RADS Prostate Imaging – Reporting and Data System: 2015, Version 2. European Urology, 69(1):16 – 40, 2016.

[WDH15] C. L. Welsh, E. V. DiBella, and E. W. Hsu. Higher-Order Motion-Compensation for In Vivo Cardiac Diffusion Tensor Imaging in Rats. IEEE Transactions on Medical Imaging, 34(9):1843–1853, 2015.

[WEM11] M. E. Wagshul, P. K. Eide, and J. R. Madsen. The pulsating brain: A review of experimental and clinical studies of intracranial pulsatility. Fluids and Barriers of the CNS, 8(1):5, 2011.

[Wet13] A. Wetscherek. Magnetic resonance diffusion weighted imaging: flow compensated intravoxel incoherent motion imaging as a tool to probe microvasculature. Thesis, Ruprecht-Karls-Universität Heidelberg, 2013.

[WMNO06] R. A. Waltz, J. L. Morales, J. Nocedal, and D. Orban. An interior algorithm for nonlinear optimization that combines line search and trust region steps. Mathematical Programming, 107(3):391–408, 2006.

[WS70] D. E. Woessner and B. S. Snowden. Pulsed NMR Study of Water in Agar Gels. Journal of Colloid and Interface Science, 34(2):290–299, 1970.

[WSL15] A. Wetscherek, B. Stieltjes, and F. B. Laun. Flow-compensated intravoxel incoherent motion diffusion imaging. Magnetic Resonance in Medicine, 74(2):410–419, 2015.

[ZP07] G. Zheng and W. S. Price. Suppression of background gradients in (B-0 gradient-based) NMR diffusion experiments. Concepts in Magnetic Resonance Part A, 30a(5):261–277, 2007.

[ZSR+12] J. L. Zhang, E. E. Sigmund, H. Rusinek, H. Chandarana, P. Storey, Q. Chen, and V. S. Lee. Optimization of b-value sampling for diffusion-weighted imaging of the kidney. Magnetic Resonance in Medicine, 67(1):89–97, 2012.

[ZSWKA12] H. Zhang, T. Schneider, C. A. Wheeler-Kingshott, and D. C. Alexander. NODDI: practical in vivo neurite orientation dispersion and density imaging of the human brain. Neuroimage, 61(4):1000–16, 2012.

Previous publications in scientific journals

The grid phantom and brain measurements with the eddy-current-compensated double diffusion encoding sequence were previously published in [MWKL17].

Danksagung

This part I would like to do in my mother tongue: An dieser Stelle möchte ich mich bei allen bedanken, die mich über die letzten Jahre hinweg unterstützt und begleitet haben.

Zuerst seien die Professoren Semmler und Ladd genannt, die mir die Möglickeit gaben diese Arbeit in der Abteilung Medizinische Physik in der Radiologie am DKFZ durchzuführen.

Außerdem gilt mein Dank Professor Bachert für das Vertreten der Doktorarbeit gegenüber der Fakultät und Professor Seco für die Erstellung des Zweitgutachtens.

Ein ganz großes Dankeschön geht an Fred Laun für die Aufnahme in seine Arbeitsgruppe und die intensive Betreuung der Arbeit. Ich danke dir außerdem für die Dinge, die du mir über die wissenschaftliche Arbeit und das Schreiben darüber beigebracht hast.

Ein weiterer Dank geht an die gesamte Arbeitsgruppe, die eine freundliche und entspannte Arbeitsatmosphäre geschaffen haben. Von einer erschöpfende Liste aller, die in meiner Zeit am DKFZ gekommen, gegangen oder die gesamte Zeit dabei gewesen sind, möchte ich allerdings absehen, da ich sicher einige vergessen würden.

Natürlich darf auch meine Familie, allen voran meine Eltern, nicht vergessen werden. Sie haben mich mein Leben lang geliebt, begleitet, unterstützt und vorangetrieben. Ich danke euch über alles dafür.

Ich auch an meine Freunde und Bekannten aus meiner Zeit in Heidelberg denken, die mit mir meine Freuden geteilt und mir über stressige Zeiten geholfen haben. Dabei sind besonders die SMD, mit meinen Hauskreisen und dem Dossenheimer (ehemals Handschuhsheimer) Gebetsfrühstück.

Ein ganz besonderer Dank an alle, die nochmal über die Arbeit gelesen haben und sie mit ihren Anmerkungen verbesserten. Alle verbleibenden Rechtschreib- und Zeichenfehler sind allein meine Schuld.

Last, but not least (doch nochmal englisch) möchte ich dem Herrn danken, der mich schon liebte bevor ich ihn kannte wurde und der mich weiterhin liebt, obwohl er mich kennt.

Erklärung:

Ich versichere, dass ich diese Arbeit selbstständig verfasst habe und keine anderen als die angegebenen Quellen und Hilfsmittel benutzt habe.

Heidelberg, den (Datum) . . . . . .